APPLICATIONS OF SQUID MAGNETOMETERS TO BIOMAGNETISM AND NONDESTRUCTIVE EVALUATION

J.P. WIKSWO
Vanderbilt University
Department of Physics and Astronomy
Box 1807 Station B
Nashville, TN 37235, U.S.A.

Abstract. Since their introduction to biomagnetism in 1970, SQUID magnetometers have been used worldwide to measure magnetic signals from the heart, brain, lungs, liver, nerves, skeletal muscle, stomach, intestines, eyes, and other organs. The majority of the effort in the field has been by university and national-laboratory researchers and by small, high-technology companies, and has been directed towards the development and promotion of this technology. While a SQUID clearly is an accepted and productive research instrument, the application of this technology in routine clinical diagnosis is only now beginning. The challenge is to identify applications for which SQUIDs are ideally suited and there is minimal competition from other technologies. The introduction of high-temperature superconductor (HTS) SQUIDs has led to a resurgence, for example, in measurements of the magnetocardiogram by physicists and new searches for applications. Similar trends are evident in the use of SQUIDs for the nondestructive evaluation (NDE) of aircraft and other structural systems and materials: most of the effort is directed towards instrumentation development and demonstrations in simple systems. Instruments suitable for specific commercial applications are just now being prototyped, and there is a new generation of HTS SQUIDs for NDE. This chapter presents an overview of SQUID magnetometers for biomagnetism and NDE, reviews a number of pertinent applications of SQUIDs, and discusses the criteria for successful application.

H. Weinstock (ed.), Applications of Superconductivity, 139–228.

1. Introduction

Superconducting QUantum Interference Device (SQUID) magnetometers have been used for measuring the magnetic fields produced by biological systems since 1970, when David Cohen, Edgar Edelsack and Jim Zimmerman demonstrated that a superconducting point-contact magnetometer could be used to record the human magnetocardiogram (MCG) inside of the MIT shielded room [1]. SQUIDs were introduced to nondestructive evaluation (NDE) by Harold Weinstock and Marty Nisenoff in 1985 [2]. Since then, there have been numerous reviews and conference proceedings and even several books that describe in detail many of the applications of SQUIDs to biomagnetism and nondestructive evaluation [3–15]. This chapter is derived largely from a 1994 lecture and the resulting paper [16]. My goal for this chapter is to update that review and direct it more towards the SQUID builder, and in doing so provide a self-contained summary of the types of applications of SQUIDs that have proven successful and would be fruitful for further investigation. Hence, the references I cite are primarily those drawn from my 1994 paper, and are used to analyze the capabilities and limitations of SQUIDs for these applications. I will not discuss marketing issues; for that the reader is referred to my 1994 paper.

2. The Signals of Interest

2.1. BIOMAGNETIC SIGNALS AND THEIR SOURCES

Biomagnetism is the measurement of the magnetic fields that are produced by biological systems. These fields are either the result of ionic currents flowing within the tissue, or by the ferromagnetic, paramagnetic, or diamagnetic properties of either the tissue or added tracers or contamination. In addition to the early MCG studies, the Zimmerman SQUID was used at MIT to study the magnetoencephalogram (MEG) from electrical activity of the brain [17]. Cohen and numerous other investigators subsequently recorded signals from a wide variety of sources within the brain, including the spontaneous alpha and delta rhythms, spikes associated with epilepsy, and evoked responses resulting from auditory, visual, tactile, and other stimulation [3,5]. Biomagnetic signals have also been detected from the eye as the magnetooculogram and the magnetoretinogram, the stomach as the magnetogastrogram (MGG), the small intestine as the magnetoenterogram (MENG), skeletal muscle as the magnetomyogram (MMG), peripheral nerve as the magnetoneurogram (MENG), and the fetal heart and brain as the fetal magnetocardiogram (FMCG) and magnetoencephalogram (FMEG). As shown in Fig. 1, the strength of these signals ranges from 10 femtotesla (fT) to more than 10,000 fT, at frequencies from several cycles

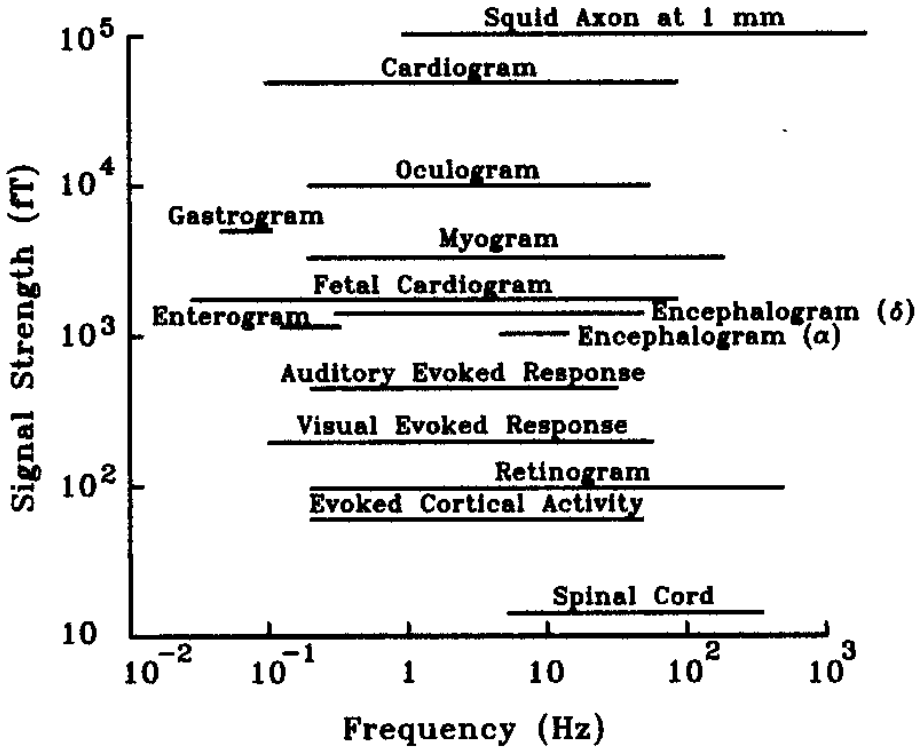

Figure 1. A logarithmic graph of the strength and frequency bandwidth of various biomagnetic signals. (Adapted from [9])

per minute to a kilohertz.

Clearly, the widest scientific and commercial interest has been directed towards the MEG and hence this is the area with the most active instrumentation development. As shown in Fig. 2, the cortex of the human brain is filled with nerve cells that have distributed dendritic networks. In the course of the electrical activity of the brain, currents in these dendrites act like small electric dipoles. If the dipole is located tangential to the approximately spherical surface of the brain, it will produce an external magnetic field; collections of 10^4 dendrites active in a 1 mm^2 area of cortex can produce magnetic fields that are measurable outside the surface of the scalp with a SQUID magnetometer [18]. Figure 3 shows an example of magnetoencephalogram waveforms recorded with a SQUID magnetometer in an unshielded environment during an epileptic seizure [19].

In contrast to the brain, in which magnetic signals are produced by innumerable asynchronous sources, the electrical activity of the normal heart is a highly synchronized yet distributed current source that propagates through the heart as a wave. From the surface of the chest, as shown in Fig. 4a, the heart looks like an electric battery, or current dipole, whose amplitude and orientation varies in time. The peak magnetic field from the

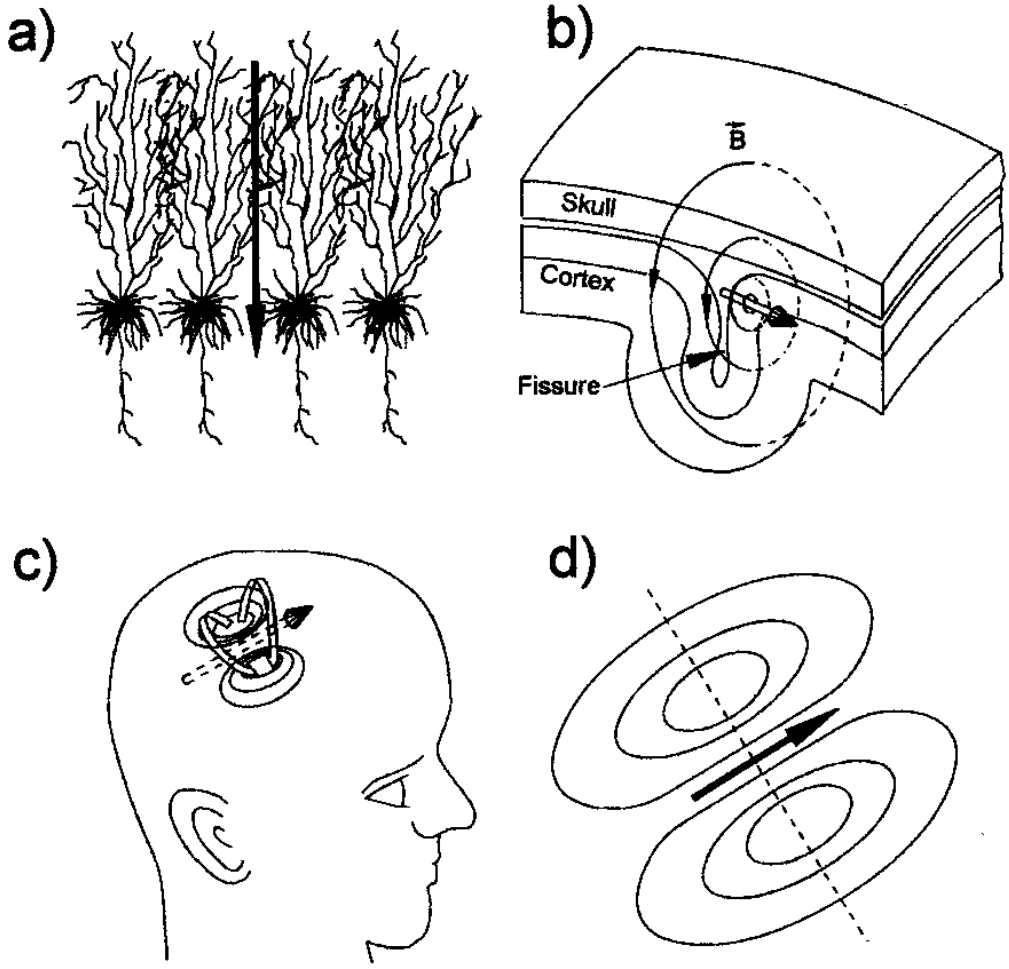

Figure 2. The magnetic field from the brain. a) A collection of simultaneously active cortical dendrites whose summed electrical activity produces electric and magnetic fields similar to that of a current dipole. b) Equivalent dipole sources adjacent to a sulcus (fissure) in the brain oriented so that the dipole is tangential to the surface of the skull produce externally detectable magnetic fields in (c), which produce the characteristic dipolar pattern of isofield contours in (d). (Adapted from [5])

heart exits the chest on the left side and enters the abdomen lower on the right; the strength and orientation of the source and hence its magnetic field vary throughout the cardiac cycle. Inside the heart, as shown in Fig. 4b, the source is an activation wave front that serves as a two-dimensional battery, *i.e.*, a current source on the outer surface and a current sink on the inner one. It can be shown that the battery in Fig. 4a is simply the electrical

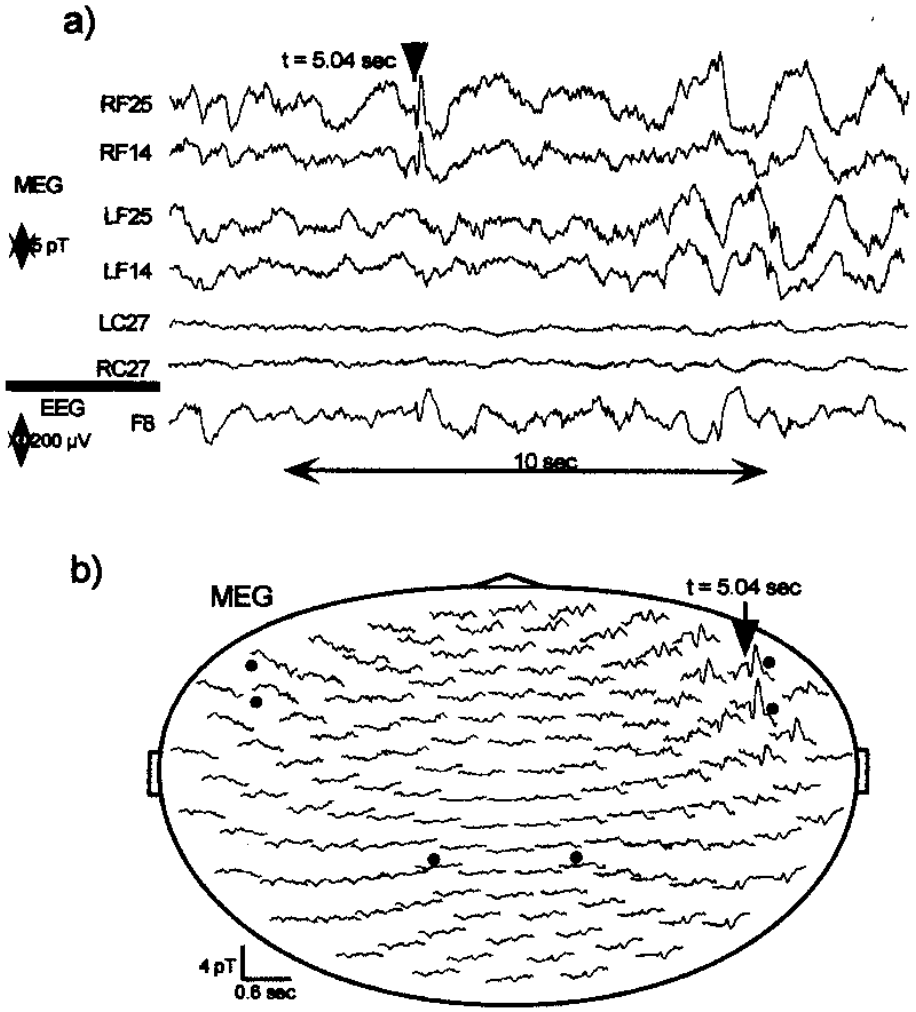

Figure 3. The magnetic field from the brain during an epileptic seizure. Top: Fifteen-second segments of an 800-second recording of MEG and EEG waveforms during temporal-lobe epilepsy with complex partial seizures, measured in an unshielded environment (MEG bandwidth dc to 40 Hz, EEG bandwidth 0.16 to 40 Hz). Bottom: MEG tracings from the entire 143-channel SQUID array. (From [19], with permission)

dipole moment of the wavefront in Fig. 4b [5]. The magnetocardiogram in Fig. 5 was recorded by the Jülich group with a first-order HTS rf SQUID gradiometer in a magnetically shielded room [20]. The limiting noise with an LTS SQUID, with a bandwidth of 250 Hz, is a fraction of a picotesla (pT) and does not come from the SQUID or the magnetic shield, but it is magnetic noise from the patient [21].

The signals from other bioelectric sources are produced in a manner similar to the MCG and the MEG. A susceptometer can be used to measure non-invasively the paramagnetic iron stored in the human liver [22]. SQUID systems that involve the sequential magnetization and magnetic field measurement are proving useful for detecting the magnetic fields from

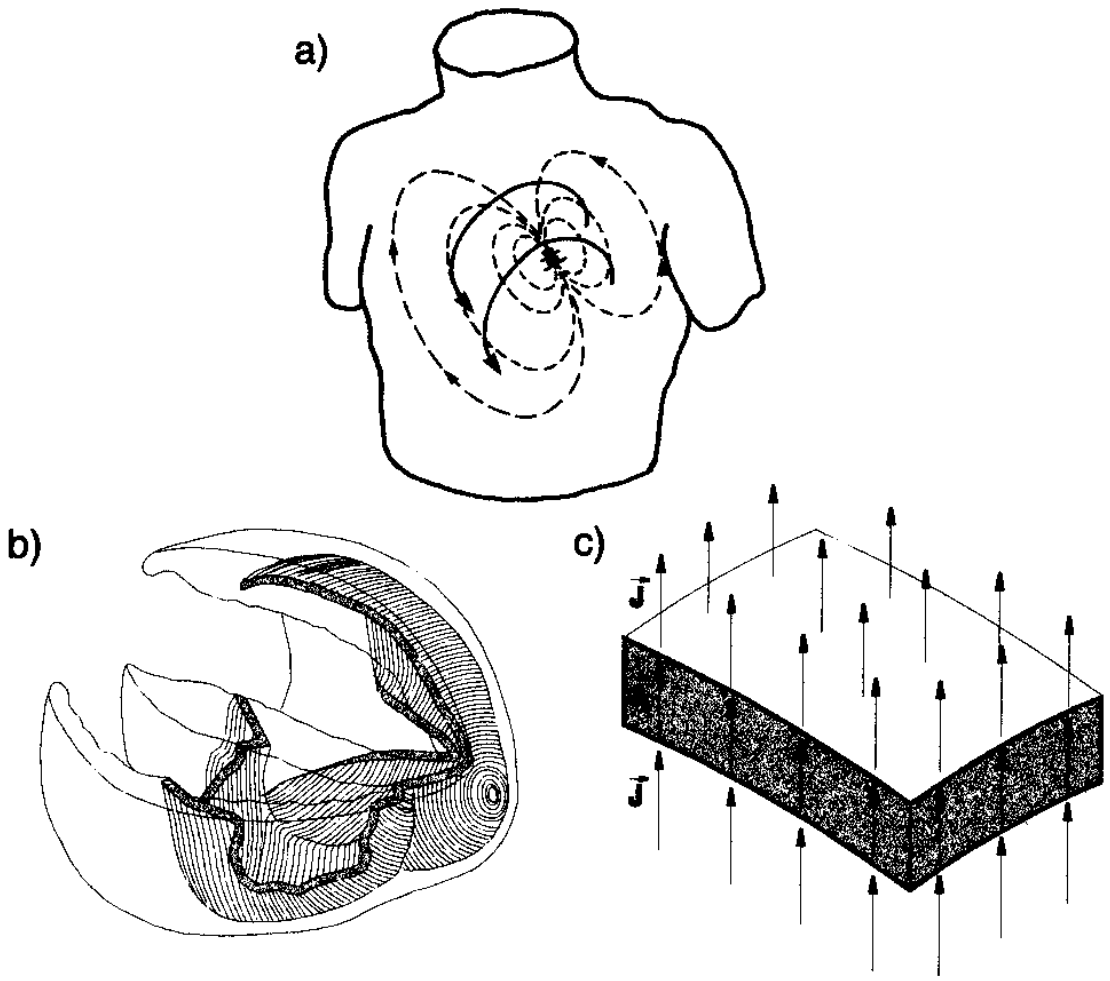

Figure 4. The magnetocardiogram. a) The magnetic field from the heart at the time of peak signal. b) The source of the magnetocardiogram is a wave front of activation that is approximately 1 mm thick and moves with velocity of up to 0.5 meters per second. c) A closeup of the wavefront showing the impressed current density $\vec{J}_i$ within the wavefront and the Ohmic current $\vec{J}$ in the tissue on either side of the wavefront. (Adapted from [5])

ferromagnetic particles in biological systems [23] or *in vitro* immunoassays [24–27].

2.2. NDE SIGNALS USING SQUIDS

The majority of biomagnetism applications simply record the intrinsic magnetic field produced by the biological system. In contrast, the majority of NDE applications detect the perturbations in an applied magnetic or electric field that result from some flaw in the sample under test. As a result, there is a larger number of fundamentally different ways to use SQUIDs in

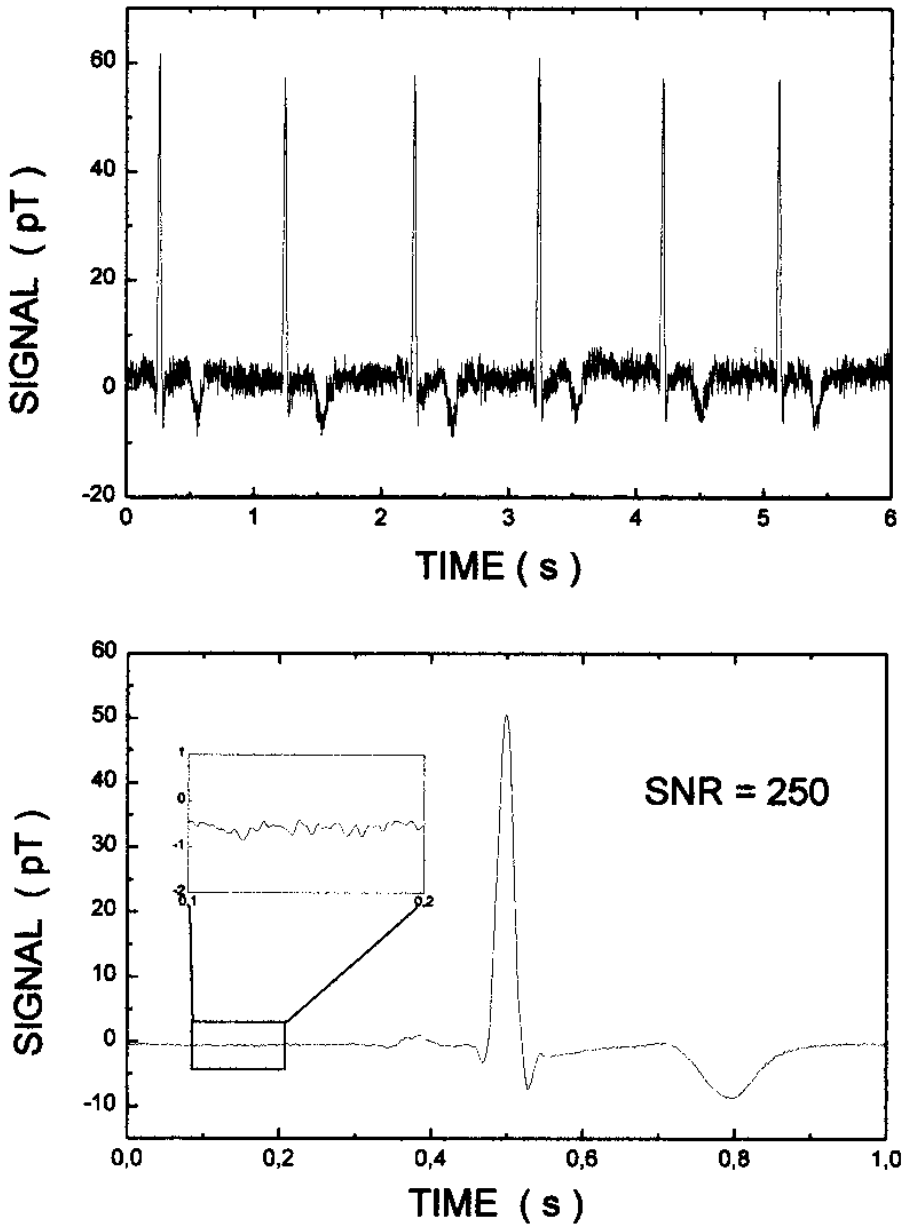

Figure 5. Magnetocardiograms recorded inside a magnetically shielded room with a 10-cm baseline electronic HTS gradiometer in a 0.016-250 Hz bandwidth [20]. a) Real-time signal of a healthy person, signal-to-noise ratio (SNR) is 35. b) Signal averaged over 300 beats, SNR = 400. (From [20], with permission)

NDE than in biomagnetism. Figure 6 shows that SQUIDs can be used in several different NDE modes [28]. The intrinsic currents in Fig. 6a could be electrical signals in a printed or integrated circuit or in a superconductor [13,29–32]. The remanent magnetization in Fig. 6b could be provided by magnetic inclusions in slices of rock [33], the magnetic-field-sensing magnetosomes in biological tissue [34,35], or magnetic tracers used in magnetic

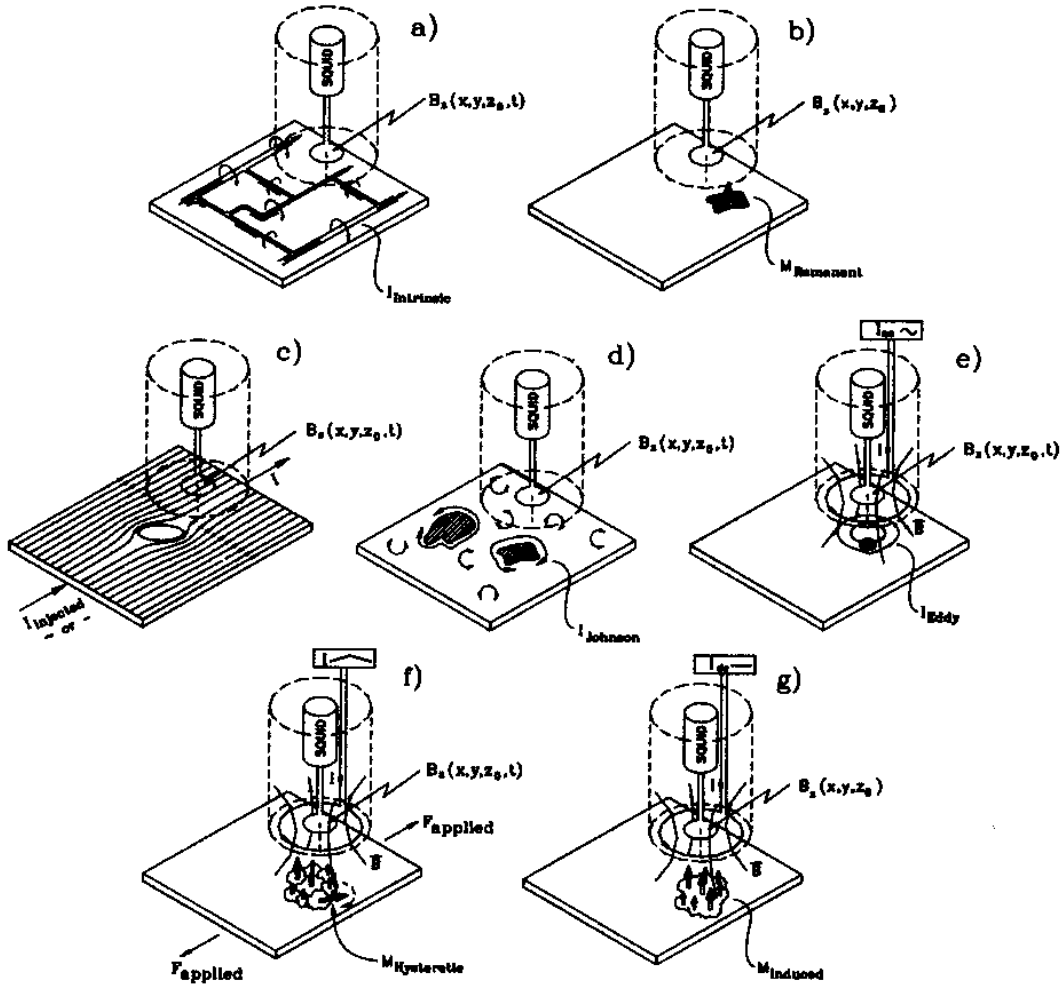

Figure 6. Modes of SQUID NDE. By scanning the sample beneath the SQUID, it is possible to image a) intrinsic or applied currents in a circuit or superconductor, b) remanent magnetization, c) flaw-induced perturbations in applied currents, d) Johnson noise or corrosion activity in conductors, e) eddy currents and their perturbations by flaws, f) hysteretic magnetization in ferromagnetic materials in the presence of an applied stress and/or an applied field, and g) diamagnetic and paramagnetic materials in an applied field. (From [28], with permission)

decoration of surface flaws [36] or magnetic-relaxation immunoassay [25,26]. The application of current to a sample can be used to detect flaws that have a differing conductivity from that of the surrounding metal [37–40], as in Fig. 6c. SQUIDs are sufficiently sensitive that they can be used to image the current distributions associated with Johnson noise or corrosion in metallic conductors [41,42] (Fig. 6d). If an ac magnetic field is applied to the sample by a coil or sheet-inducer, as in Fig. 6e, the SQUID can be used

to image the resulting eddy currents or their perturbation by flaws in the object [43–45]. The application of stress to a ferromagnetic material and/or simultaneously applied ac and dc magnetic fields will alter the magnetization (Fig. 6f), such that the SQUID can be used to map the distribution of stress-related changes in the ferromagnetic state of the material [46]. Finally, the dc magnetic field applied in Fig. 6g can be used to image the magnetization of diamagnetic and paramagnetic materials [28,33,47]. We will discuss several of these applications later in this chapter.

3. Instrumentation

The weak field strength, the substantial information content at low frequencies, and the broad measurement bandwidth all suggest that SQUIDs will remain the magnetometer of choice for biomagnetic measurements in the immediate future, with the exception of measurements on isolated, one-dimensional nerve and muscle tissue preparations that can be made with miniature toroidal pickup coils [48] and possibly the measurement of the adult MCG using optical [49–51], or giant-magnetoresistance magnetometers [52–57]. As we will see later, the strength of some of the biomagnetic signals shown in Fig. 1 already places them within the range of sensitivity provided by high-transition-temperature SQUIDs.

For many applications, the energy sensitivity is utilized to obtain the highest possible field sensitivity, but in other applications, the field sensitivity can be sacrificed to obtain high spatial resolution [10,13]. For all of the applications discussed in this chapter, the sample being studied, for example the human head or a piece of an airplane, is at room temperature while the SQUID is at either liquid helium or liquid nitrogen temperature. We will begin this section with a general overview of SQUIDs, then describe common techniques used for fabricating the SQUIDs for biomagnetism and NDE, and conclude with a description of a number of commercial SQUID instruments.

3.1. SQUID MAGNETOMETERS

A SQUID is a Superconducting Quantum Interference Device, and has as its active element one or more Josephson junctions (Reference [58] provides more details on SQUIDs). A Josephson junction is a weak link between two superconductors that can support a supercurrent below a critical value I_c. An rf SQUID uses a single Josephson junction that is connected to a superconducting loop; an rf current bias is inductively coupled to the SQUID to measure its impedance. A dc SQUID uses a superconducting loop with a pair of Josephson junctions, and a dc current is applied directly to the SQUID to measure the loop impedance, as shown in Fig. 7. In either

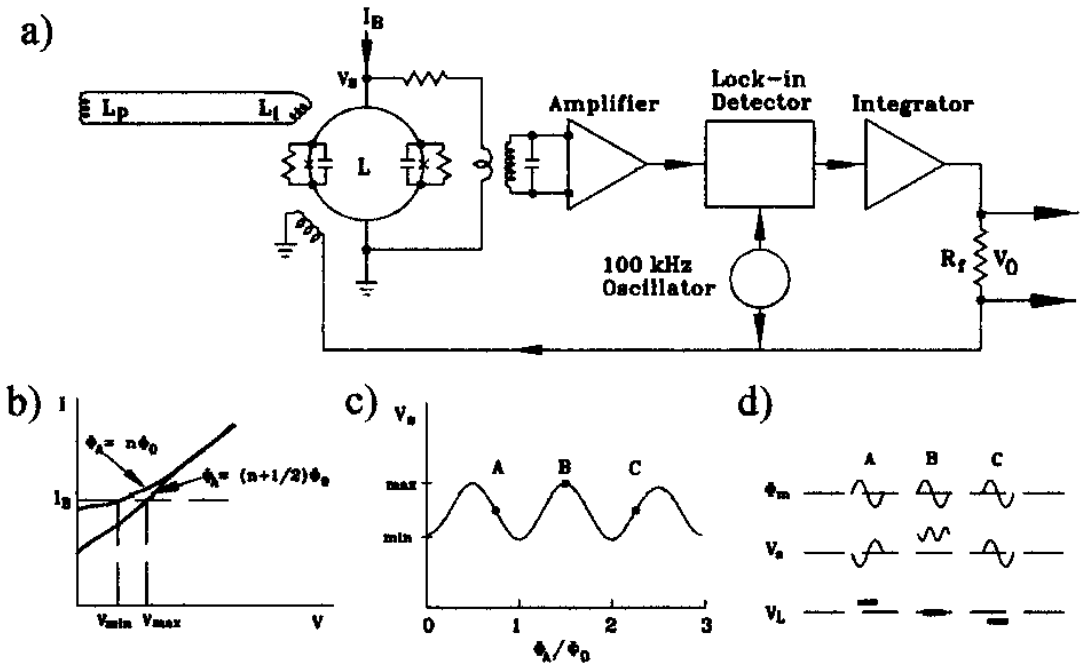

Figure 7. 1. A dc SQUID. a) A simplified circuit for a dc SQUID magnetometer. b) The current-voltage characteristic of a SQUID without feedback with two different values of flux threading the SQUID loop. The amount of applied flux, Φ_A, determines the voltage across the SQUID, V_s, for a particular value of bias current, I_B. As the applied flux varies between $\Phi_A = n\Phi_0$ and $\Phi_A = (n + 1/2)\Phi_0$, the SQUID voltage changes between V_{min} and V_{max}. c) The V-Φ curve of a dc SQUID, with constant bias current. d) The voltage response of the SQUID to a modulating flux, Φ_m. The response varies greatly depending on the value of Φ_A. Three possible points are highlighted to illustrate the response of a SQUID and the feedback needed to "lock" the SQUID to operation at an extreme value. From top to bottom we see: one cycle of the flux modulation, Φ_m, applied to the SQUID operating at three different locations on the V-Φ curve, the voltage response of the SQUID, V_s, and the necessary feedback of the flux-locked loop, V_L, which applies a counter flux to the SQUID loop to return the system to an extreme position on the V-A curve. (From [13], with permission)

type of SQUID, the special properties of the Josephson junction cause the impedance of the SQUID loop to be a periodic function of the magnetic flux threading the SQUID, so that a modulation signal applied to the bias current is used with a lock-in detector to measure the impedance and to linearize the voltage-to-flux relationship. The net result is that a SQUID functions as a flux-to-voltage converter with unrivaled energy sensitivity.

While early SQUIDs were made with point contacts [1,59,60], subsequent designs used thin-film tunnel junctions and toroidal input and rf coils in a toroidal niobium cavity. Hybrid dc SQUIDs, such as those produced for many years by Biomagnetic Technologies, Inc. (BTi), used a pair of tunnel junctions in a toroidal coupling cavity. Today, the majority of dc

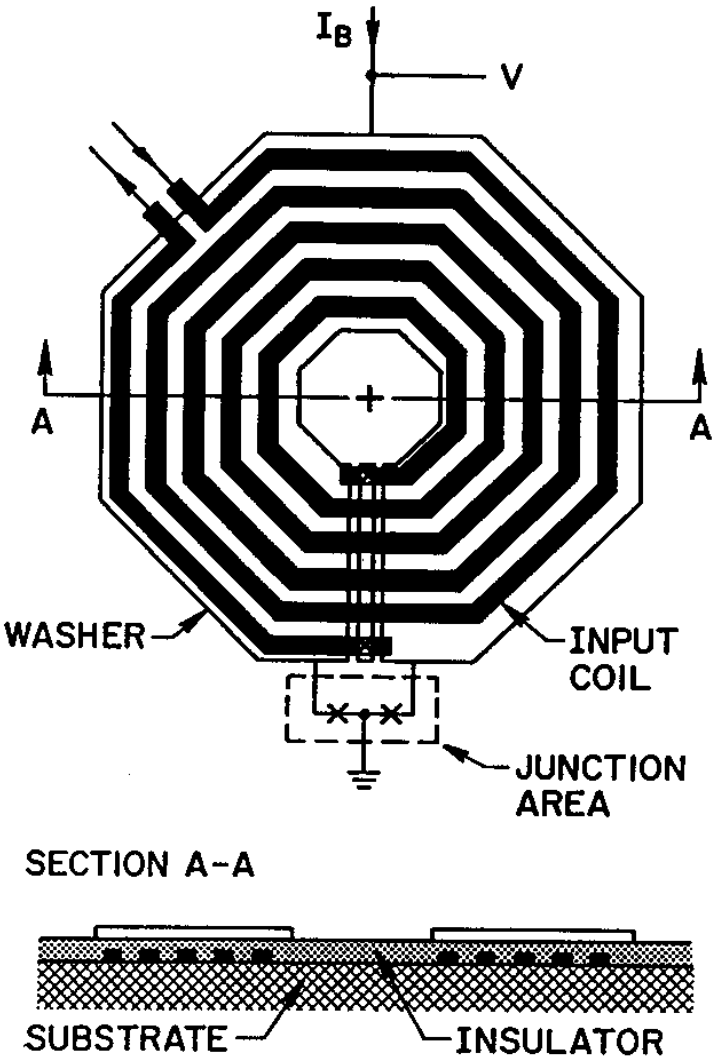

Figure 8. A schematic drawing of a washer-type dc SQUID. The Josephson junctions are the pair of ×'s below the large octagonal washer, which forms part of the superconducting loop containing the Josephson junctions, and also serves as a one-turn winding in the transformer that couples magnetic flux from the input coil to the SQUID. The pickup coils, which are not shown, are connected to the input coil by the two leads at the upper left edge of the input coil. The bias current, applied to the upper edge of the washer, is divided between each side of the washer and the series-connected Josephson junction. The hole in the center of the washer is typically on the order of 50 μm to 100 μm in diameter, so that the diameter of the entire washer is usually a fraction of a millimeter. (Courtesy of Mark Ketchen of the IBM Thomas J. Watson Research Center)

SQUIDs are made using a geometry developed by Mark Ketchen at IBM, as shown in Fig. 8, in which the SQUID loop is partially formed by a large washer that couples the SQUID to the external flux transformer. The dc bias current is applied to one side of the washer, and the other side of the SQUID loop is grounded. This geometry provides SQUID loops with low inductance and hence high sensitivity, while allowing efficient coupling to

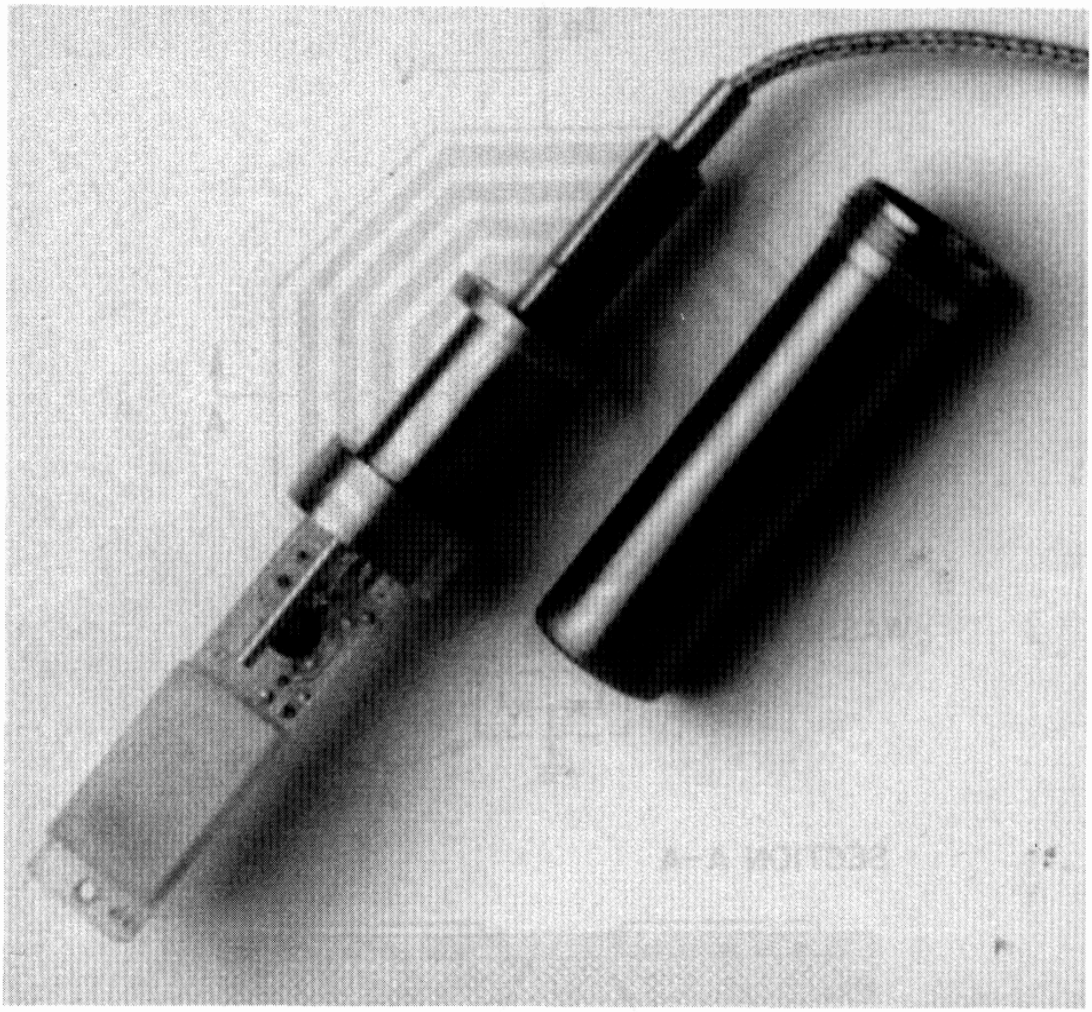

Figure 9. A commercial dc SQUID probe. The SQUID sensor is encapsulated near the end of the circuit board; the dark circle is a toroidal impedance-matching transformer. The threaded cylinder is the niobium shield that encloses the SQUID sensor and circuit board. The braided cable is the transmission line that connects the room temperature electronics to the SQUID. (Courtesy of Quantum Dynamics, Inc., San Diego)

an external flux transformer.

In most LTS SQUID systems in use today, the SQUID is located inside a small cylindrical, superconducting magnetic shield, as shown in Fig. 9. In the United States, Quantum Design is the primary supplier for packaged, user-installable dc SQUIDs. The SQUID assembly is then mounted in a cryostat that is placed inside a superinsulated, fiberglass, liquid-helium dewar, as shown in Fig. 10. Superconducting pickup coils, typically configured as gradiometers that detect the difference in one component of the field between two points, are located at the bottom of the dewar. The test object, for example a section of an aircraft wing or a subject's head, is placed be-

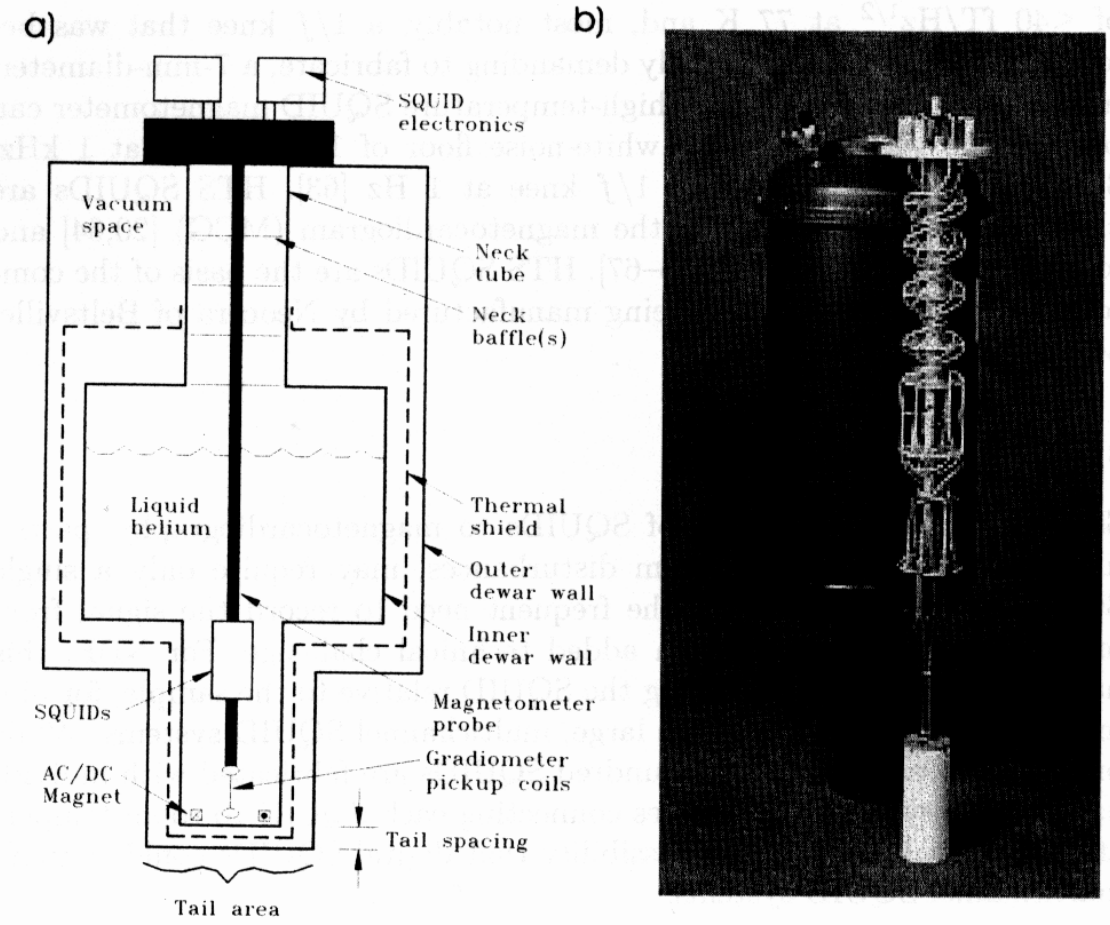

Figure 10. A typical single-channel SQUID magnetometer used for biomagnetic measurements or NDE. a) A cross-sectional schematic of dewar and the cryostat that supports the SQUIDs and the pickup coils. (Adapted from [9]) b) A photograph of a six-channel SQUID system, with the cryostat removed from the dewar. The majority of the dewar is usually fabricated from fiberglass-epoxy composite, although in some designs the helium reservoir and the dewar top are aluminum. (Courtesy of Robert Fagaly of Tristan Technologies, San Diego, CA)

neath the magnetometer. A ferritometer for measuring liver iron, or many NDE systems will have a magnet in addition to the SQUID. The cryostat and the dewar must minimize helium boil off, eliminate rf interference, and not contribute Johnson noise or distort any external ac fields.

3.1.1. *HTS SQUIDs*

HTS SQUIDs are discussed in detail elsewhere in these proceedings [61]. While HTS SQUIDs will always be noisier than LTS ones, the performance of HTS SQUIDs continues to improve. The Jülich single-layer $YBa_2Cu_3O_7$ rf SQUID magnetometer with a direct-coupled pickup coil and a flip-chip flux transformer demonstrated, in a magnetic shield, a field noise at 1 Hz

of $\leq$40 fT/Hz$^{1/2}$ at 77 K and, most notably, a $1/f$ knee that was below 1 Hz [62]. While technically demanding to fabricate, a 7-mm-diameter, multilayer, 16-turn multiloop high-temperature SQUID magnetometer can provide the very respectable white-noise floor of 18 fT/Hz$^{1/2}$ at 1 kHz, 37 fT/Hz$^{1/2}$ at 1 Hz, and a $1/f$ knee at 1 Hz [63]. HTS SQUIDs are clearly suitable for recording the magnetocardiogram (MCG) [20,64] and for some NDE applications [65–67]. HTS SQUIDs are the basis of the commercial SQUID microscope being manufactured by Neocera of Beltsville, MD [68–70].

3.1.2. *Digital SQUIDs*

Some potential applications of SQUIDs to magnetocardiography, particularly those related to rhythm disturbances, may require only a single SQUID, or at most several; the frequent need to record the signal from multiple locations presents an added technical challenge. For NDE, this has been addressed by scanning the SQUID relative to the sample; for biomagnetism, the trend is to use large, multichannel SQUID systems. While present systems with several hundred SQUIDs are fabricated with individual SQUIDs with multiple wires connecting each SQUID to room temperature electronics, there is a possibility that digital SQUIDs could simplify multichannel SQUID systems.

There are two types of digital SQUIDs: room temperature and superconducting. In the former, the analog feedback loop is replaced with an analog-to-digital converter, a digital signal processor, and then a digital-to-analog converter [71–73]. This process linearizes the flux-voltage characteristics, replaces many of the room temperature subsystems such as the electronic lock-in amplifier with signal processor code, and avoids interchannel phase delays arising from differences in component values in the analog circuitry.

With the superconducting digital SQUID, Josephson digital logic provides the feedback on the same chip as the SQUID sensor [74–77]. There are many potential advantages to this approach, including the ability to multiplex the outputs of multiple SQUIDs onto a small number of wires or transmission lines, and a high slew rate and dynamic range that could greatly improve noise immunity. Since it will be possible to mass produce a complete SQUID magnetometer array on an integrated circuit production line, and then mount the finished, packaged chips in a small dewar, the cost of the systems should plummet. This, in turn, could promote the large-volume production of inexpensive, compact, portable magnetometer systems. Digital SQUIDs are discussed in more detail elsewhere in these proceedings [78].

3.2. REFRIGERATORS

The need for liquid cryogens detracts from the acceptance of SQUIDs in both the medical and NDE communities. The development of miniature Joule-Thompson, Gifford-McMahon, and pulse-tube refrigerators offers an exciting alternative, and presents the possibility of a turn-key SQUID system [79]. While mechanical refrigerators present new problems to the SQUID builder, such as power consumption, expense, size, weight, vibration and magnetic noise, this approach has been demonstrated successfully in a number of different systems [44,80–83]. There are possible alternatives that would be even quieter [84,85]. Figure 11 shows an HTS SQUID and dewar that are cooled by a Joule-Thompson cooler. Clearly, there will be increased utilization of refrigerators with SQUID systems.

3.2.1. *NOISE REDUCTION*

While SQUIDs are exquisitely sensitive magnetometers, practical applications that fully utilize this sensitivity require the elimination of environmental noise. Figure 12 shows the magnetic field noise as a function of frequency for a variety of environments ranging from the low field in the best magnetically-shielded room to the magnetic noise in a laboratory or hospital that is seven orders of magnitude larger. There are several ways to reduce noise: magnetic shields, gradiometric pickup coils, and electronic noise cancelation. The quietest magnetic shield to date is the one fabricated at the Superconducting Sensor Laboratory in Japan, with a shielding factor of 15,000 at 0.02 Hz [86]. With adequate care, it is now possible to fabricate magnetic shields that are sufficiently quiet that the limiting noise is produced by the dewar which contains the SQUIDs [87] or by the object under test. The lowest system noise measured in the Berlin magnetic shield was less than 3.5 $\mathrm{fT/Hz^{1/2}}$ in the white-noise region, 35 $\mathrm{fT/Hz^{1/2}}$ at 1 Hz, and 3 $\mathrm{pT/Hz^{1/2}}$ at 0.1 Hz, consistent with the magnetic fluctuations of the inner mumetal layer [88]. Romani *et al.*, summarize the noise of various systems in reference [89].

In general, the magnetic fields produced by distant noise sources are more uniform than the magnetic fields produced by the source of the desired signals close to the magnetometer. As a result, it is possible to fabricate superconducting flux transformers that measure the difference in the magnetic field between two nearby points, *i.e.*, a differential magnetometer. Because of the uniformity of the magnetic noise field, the noise at these two points is almost identical, and hence the field difference can be orders of magnitude smaller than the field itself. In contrast, the magnetic field from the nearby object can be significantly larger at one point than at the other. If the spacing between the two points is small relative to the spatial extent of the signal source, the differential magnetometer acts as a gradiometer,

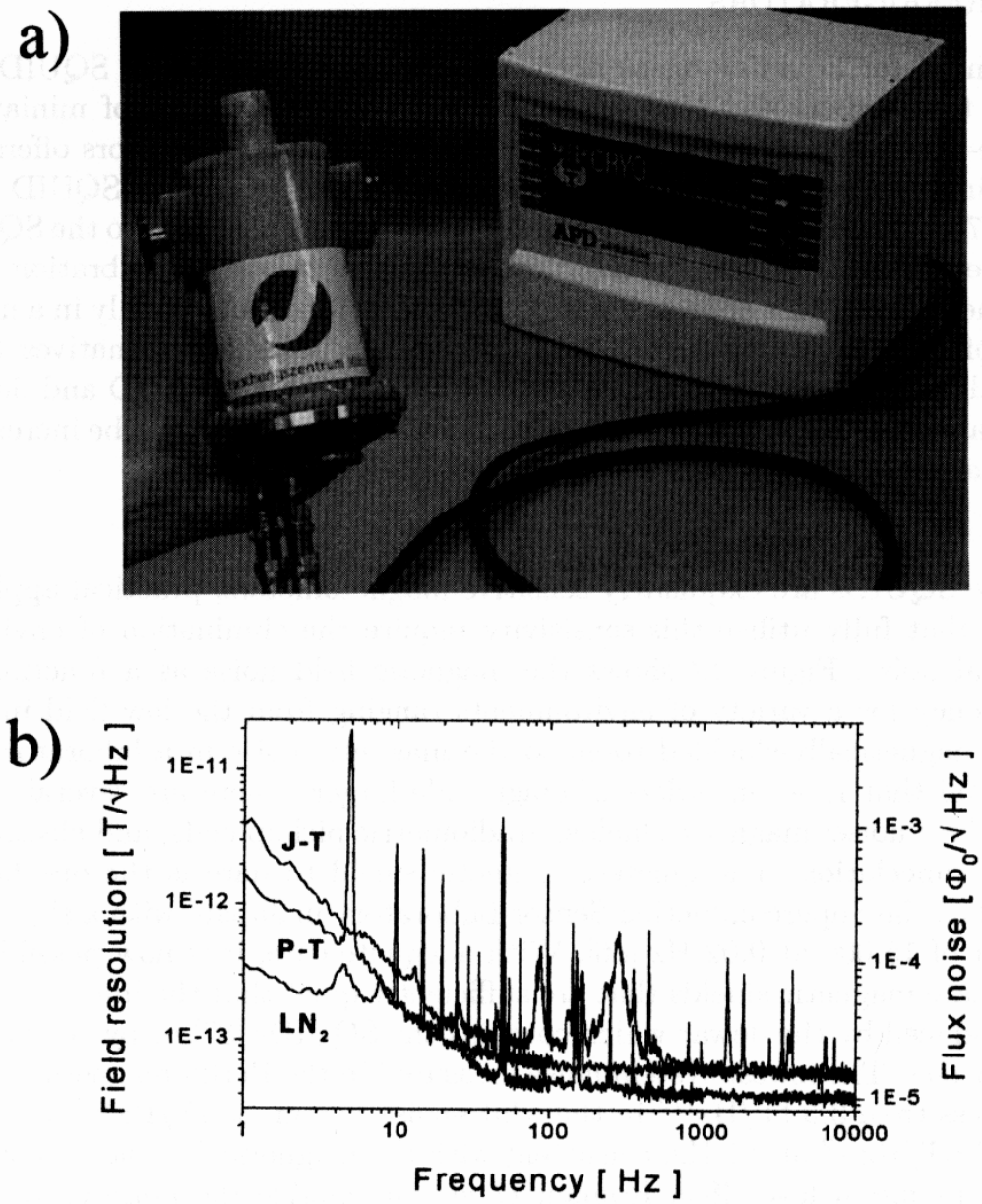

Figure 11. A cryocooled HTS SQUID magnetometer. a) A G-10 SQUID cryostat with a Joule-Thompson cooler and plastic gas lines connected to a compressor. b) The noise spectra of an rf SQUID in liquid nitrogen, and cooled by pulse-tube and Joule-Thompson refrigerators. (From [83], with permission)

measuring the spatial gradient of the magnetic field. Since the field from a magnetic dipole falls off with distance as $1/r^3$, while its gradient falls off as $1/r^4$, a gradiometer in general will be less sensitive to distant noise sources than to a nearby signal source. Figure 13 shows several configurations of SQUID pickup coils, including magnetometers, first and second-order differential magnetometers, and radial gradiometers [90,91].

Axial gradiometers that measure $\partial B_z/\partial z$ can be readily fabricated by

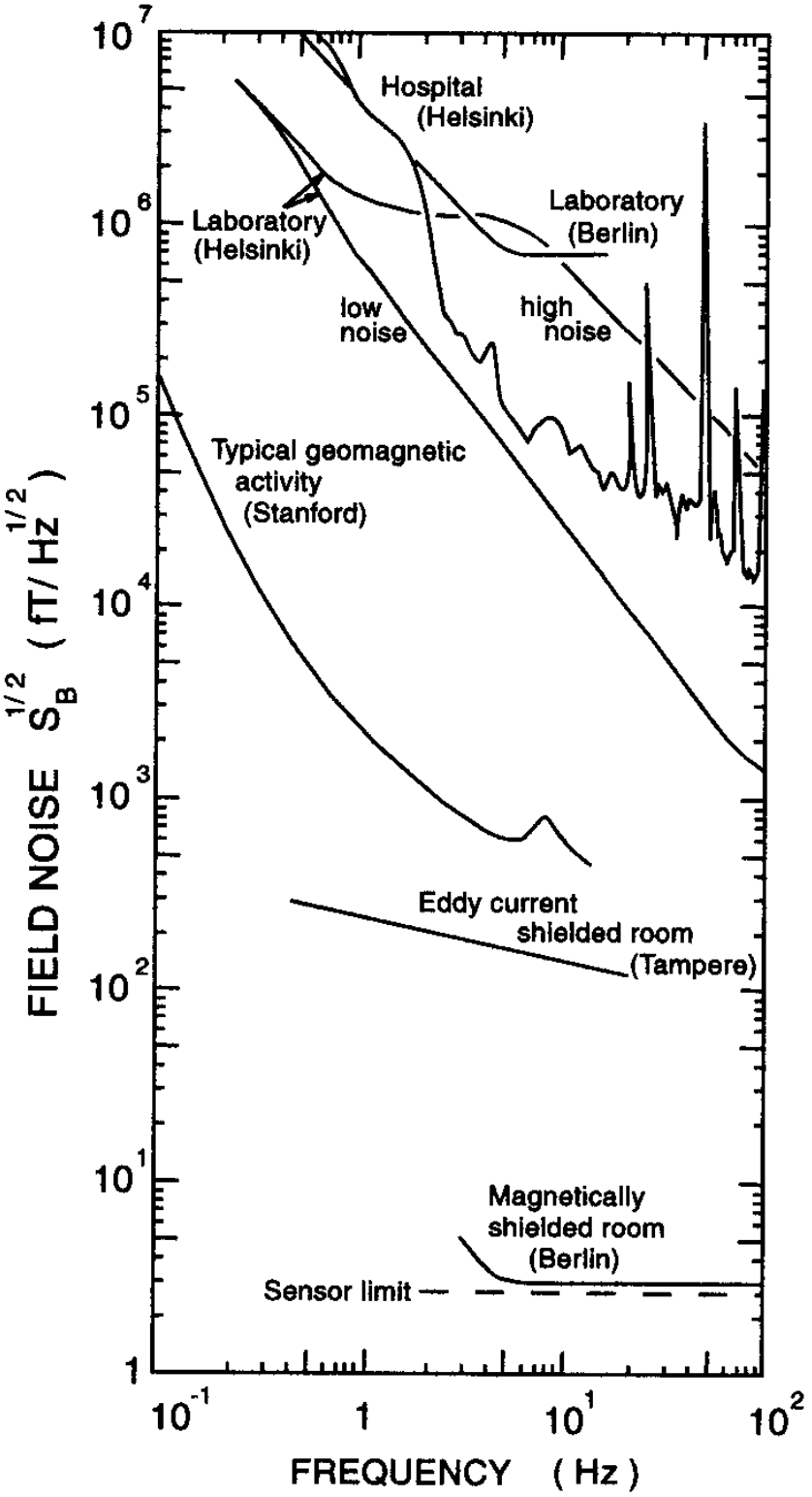

Figure 12. The frequency dependence of magnetic noise in various environments. (Adapted from [89])

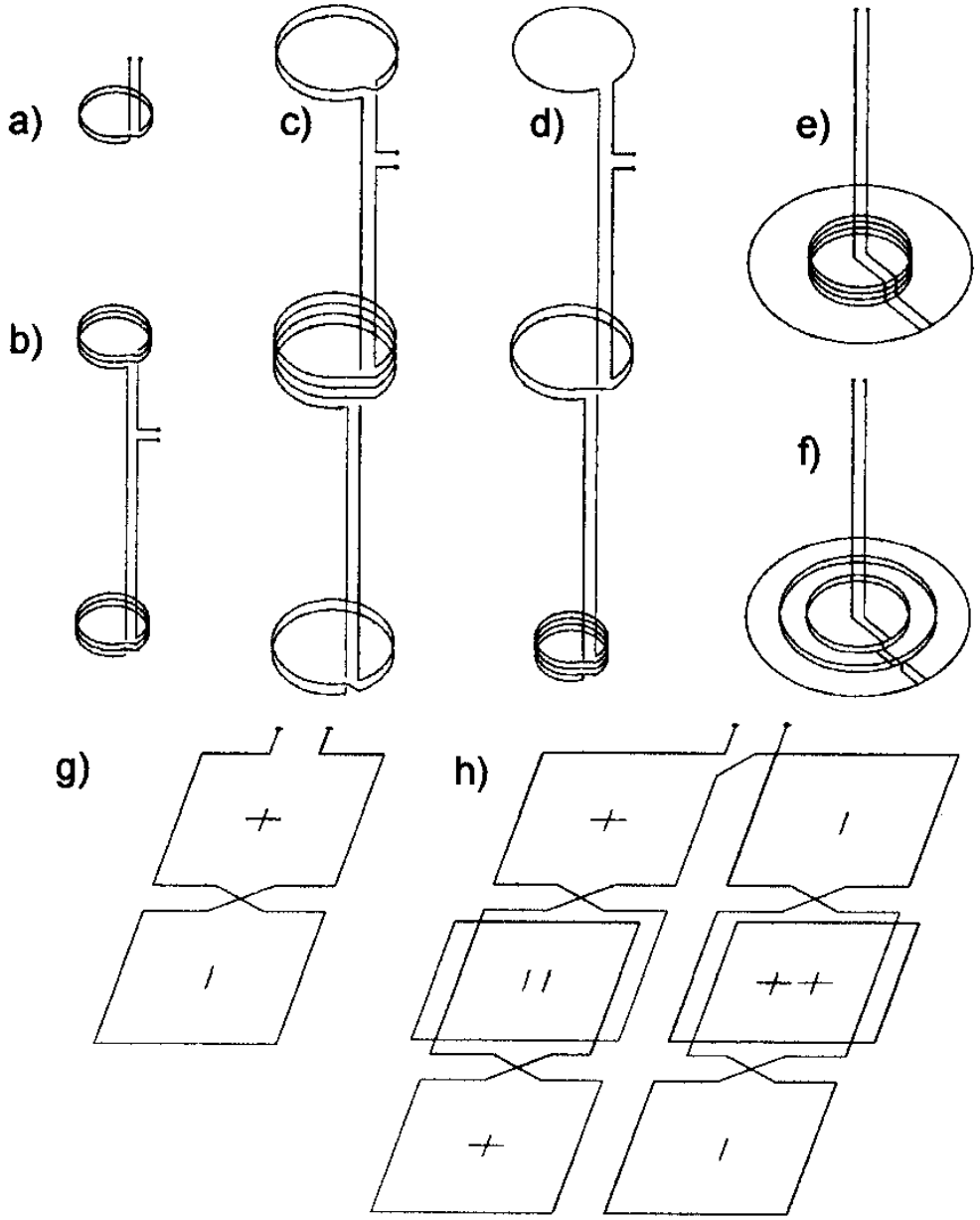

Figure 13. Various SQUID pickup-coil configurations. a) Magnetometer. b) First-order axial gradiometer. c) Symmetric second-order axial gradiometer. d) Second-order asymmetric gradiometer designed for increased face-coil sensitivity. e) Radial first-order gradiometer. f) Radial second-order gradiometer. g) A first-order pair of planar gradiometers. h) A third-order planar gradiometer formed by connecting two opposing planar second-order gradiometers. (Adapted from [90] and [91])

hand-winding superconducting wire on a carefully machined cylindrical substrate (Fig. 13b); with manual adjustment of the small superconducting tabs, this type of gradiometer can be balanced to a part in 10^6 (possibly 10^7), *i.e.*, the contribution of the distant noise source can be reduced by

a factor of 10^6 to 10^7 relative to that of the nearby signal source, for a common mode rejection of 120 - 140 db. Signals from noise sources that are close enough to produce a measurable gradient in their magnetic field can be reduced by using a second-order differential magnetometer (Fig. 13c) that in effect measures the second spatial derivative of the noise from the distant noise source. If the baseline of the gradiometer is long with respect to the distance between the lowest pickup coil and the signal source, the output of the SQUID will be a good approximation of the field at the lowest coil. One limitation of the gradiometric pickup coils in Figs. 13b and 13c is that signal energy is shared not only between the primary pickup coil and the transformer within the SQUID, but also with the balance coils. This effect can be reduced using the asymmetric gradiometer in Fig. 13d, for which as much inductance as possible is concentrated in the pickup coil that is closest to the signal source [90,92]. It is difficult to mass produce axial gradiometers, except by wrapping a flexible, planar coil around a cylindrical substrate, a technology that has yet to be extended to high temperature superconductors.

The first- and second-order radial gradiometer in Figs. 13e and f measure $\partial B_z/\partial r$ and $\partial^2 B_z/\partial r^2$ and provide excellent localization of discrete sources, but may lead to images that are difficult to interpret or deconvolve. A planar gradiometer that measures $\partial B_z/\partial x$ is shown in Fig. 13g. A four-by-four array of long-baseline gradiometers that measure $\partial B_x/\partial z$ and $\partial B_y/\partial z$ have been incorporated into a system for recording the magnetic field components of the human magnetocardiogram that are parallel to the chest wall [93]. Figure 13h shows a high-order gradiometer that is matched to the signature of a flaw as would be detected by a SQUID eddy-current system [94]. The greatest advantage of the planar gradiometers in Figs. 13e-h is that they can be mass-produced with thin-film technology using either low- or high-temperature superconductors, and can either be fabricated on the same substrate as the SQUID, or coupled to the SQUID as a "flip-chip." Their disadvantages are that it can be expensive (in terms of substrate cost) to fabricate long-baseline differential magnetometers, and the shorter baseline planar gradiometers are less sensitive to deep sources than are long-baseline axial gradiometers.

The Neuromag helmet MEG system [95] shown in Fig. 14 uses a pair of orthogonal planar gradiometers that measure $\partial B_z/\partial x$ and $\partial B_z/\partial y$ to provide a vector representation of the approximate strength and direction of an effective current source beneath the gradiometer. While this configuration localizes the current source, indicates its direction, and rejects noise from distant sources, it also has limited sensitivity to sources that are deep within the brain. When these gradiometers are used in conjunction with a magnetometer at the same location, three orthogonal source representa-

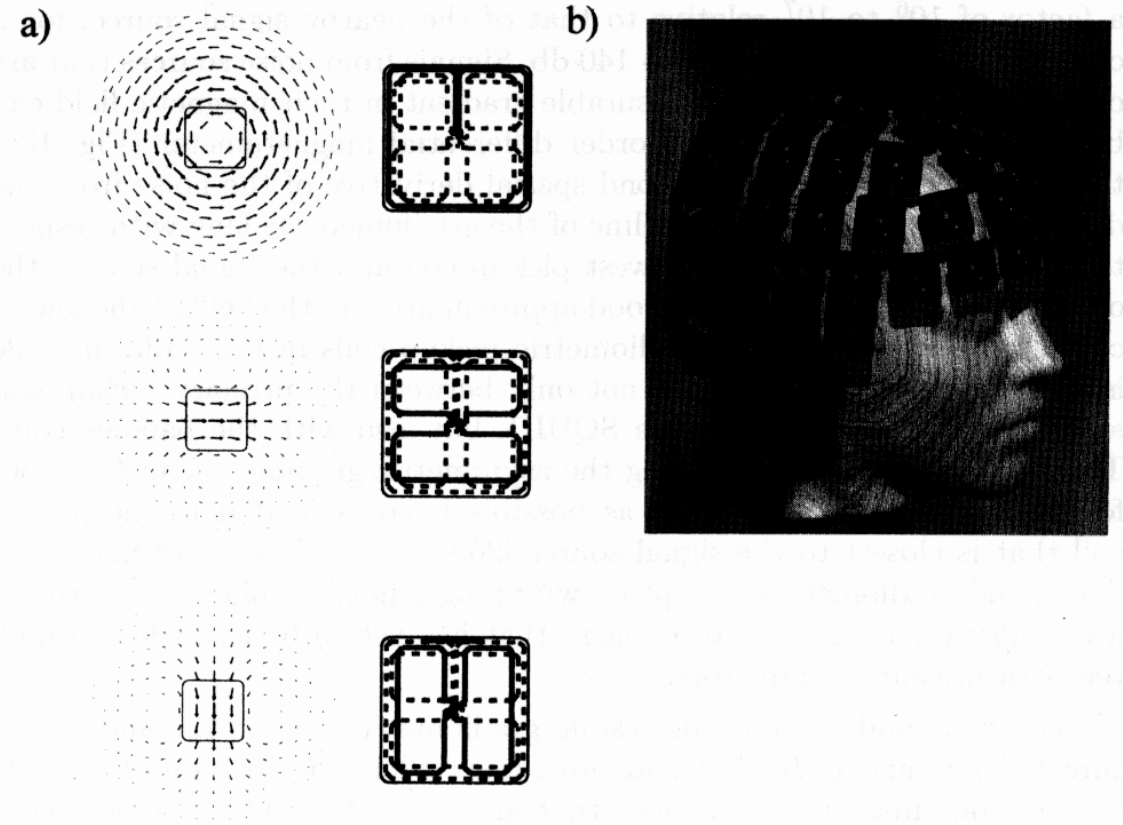

Figure 14. The Neuromag helmet SQUID system for recording the MEG. Top: The configurations of the three SQUID sensors at each site and their orthogonal sensitivity distributions. Bottom: The array of the 102 triple-SQUID units. The average spacing between sensors is 34 mm, and the distance between the pickup coil and the room-temperature surface of the helmet ranges between 17 to 19 mm. (From [95], with permission)

tions are obtained.

An alternative approach to eliminate magnetic noise is to use one or more reference magnetometers distant from the desired signal source that is coupled to a set of coils which cancel external fields over the entire measurement region or, more simply, apply a canceling magnetic flux directly to the SQUIDs or the SQUID pickup coils. The CTF and BTi helmet systems use a number of reference magnetometers and a variety of numerical algorithms to reduce the effect of external noise fields on the recorded magnetoencephalogram. The possible approaches include direct feedback, simple off-line subtraction, or adaptive signal processing. Depending upon the spatial variation of the noise field and the characteristics of the primary magnetometers or gradiometers, it may be necessary to utilize first-order reference gradiometers as well. A straightforward approach to noise cance-

lation is to use three SQUID magnetometers to measure three orthogonal components of the noise field and five more to measure the independent first-order field gradients of the noise. The CTF systems use a proprietary calibration process and algorithm to determine fixed weighting coefficients that are then used to combine the outputs of 64, 140 or 151 first-order gradiometer signal channels and 28 gradiometer reference channels to form a large array of second- and third-order synthetic gradiometers [72,96]. The data in Figs. 15 and 16 show that this approach is successful and can be used to measure auditory evoked responses in an unshielded environment. While the performance of the system is better in a magnetic shield than in an open laboratory environment, this instrument represents a significant accomplishment in electronic noise rejection in that this sensitivity of the system in an open laboratory is approaching the limit of brain noise.

There are two possible limitations to the synthetic gradiometer approach as presently implemented: the coefficients are fixed to form third-order gradiometers that rely solely on the rapid field fall-off from distant sources, and substantial capital is tied up in the reference channels, which contribute SQUID noise to the synthetic gradiometer output, but do not contribute any signal. (While the SQUID noise for the primary and reference sensors should be uncorrelated and hence would add in quadrature, it still represents a net loss in sensitivity. Note that this also occurs in a similar manner with standard gradiometers, in that the signal energy that is coupled into the reference coil is not coupled to the SQUID; the use of asymmetric pickup coils as in Fig. 13d can minimize this effect but not eliminate it [90,92]). The solution to the first problem might be to use adaptive weighting coefficients, but it is not clear how stable such a system would be for time-dependent noise sources with differing spatial characteristics. A possible solution to the second problem is to place all of the SQUID sensors adjacent to the field source, for example, the scalp in a MEG helmet system, and use numerical cross-correlation and inverse techniques to solve for the location of all effective signal sources [97]. The sources outside the helmet are assumed to be noise and are simply ignored, and those inside of the helmet are assumed to be signal. While conceptually elegant, this approach is not yet fully proven. We will discuss one approach to this, termed synthetic aperture magnetometry (SAM), in a later section.

It is important to recognize that the design problems are somewhat different for HTS SQUIDs, since there is not yet an HTS wire that can be attached to a separate SQUID sensor with a persistent-current contact. Hence, the pickup coils and the SQUID either have to be fabricated as an integral unit, or as adjacent planar structures in a flip-chip geometry (Fig. 17a). As a result, it has proven difficult to fabricate extended, non-planar gradiometer pickup coils. This limitation can be addressed by

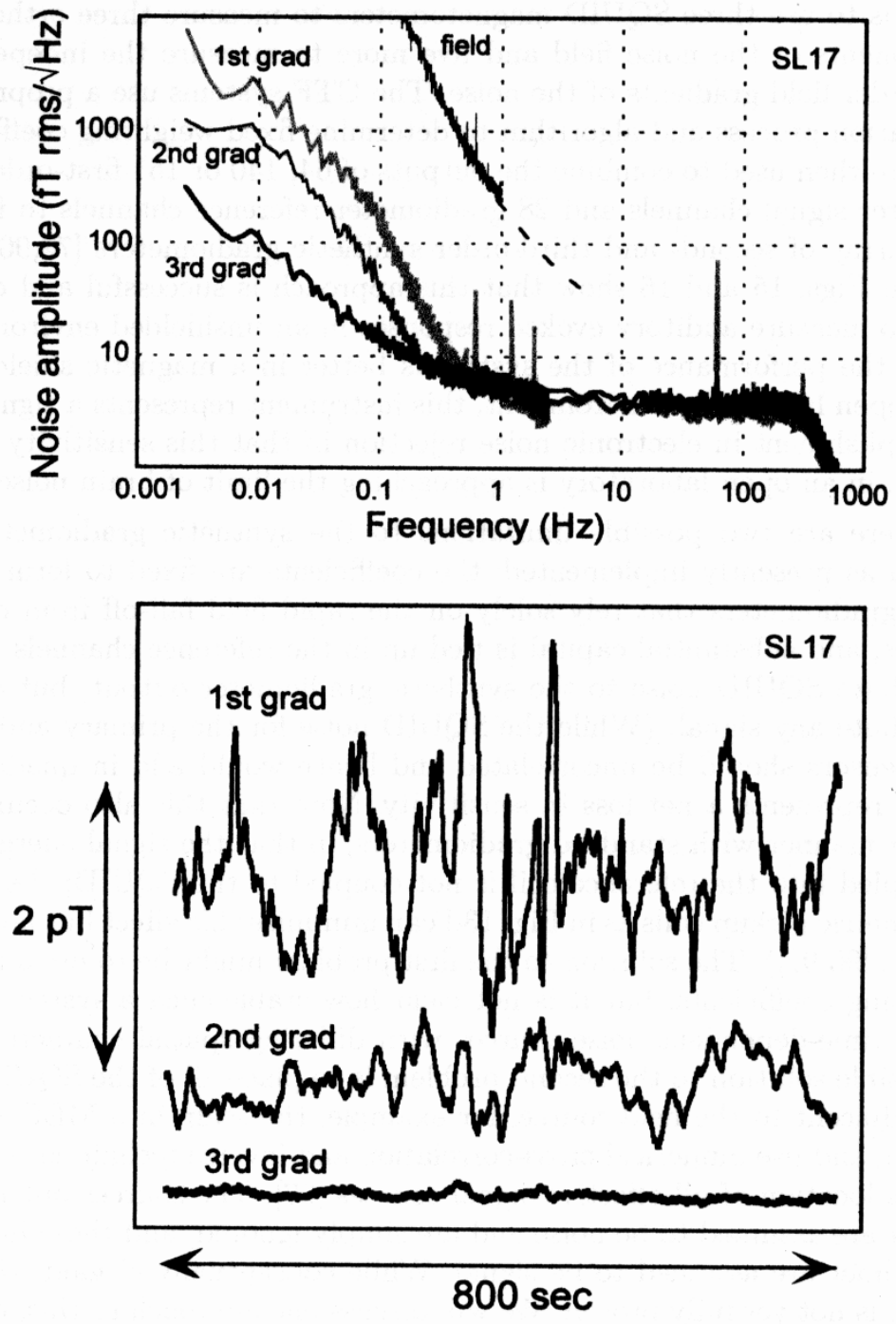

Figure 15. Noise of the 64-channel CTF MEG system in a shielded room with three different orders of electronic gradiometers [72]. (Courtesy of Jiri Vrba of CTF)

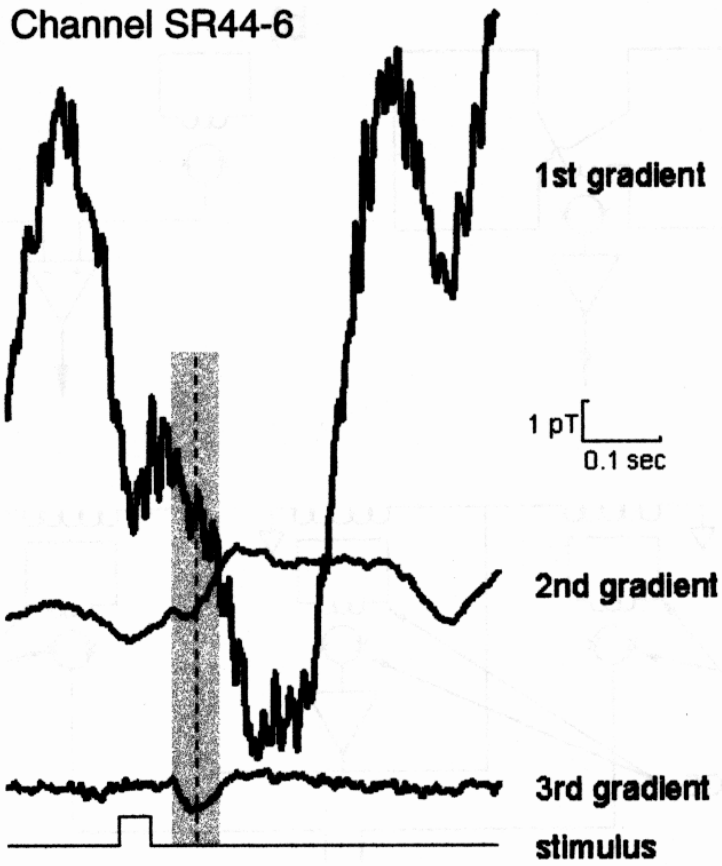

Figure 16. An auditory evoked field experiment in an open environment using the CTF 64-channel MEG system. The second and third gradient signals are synthesized from signals from multiple first-order gradiometers. The auditory response occurs during the shaded, vertical bar. (Courtesy of Jiri Vrba of CTF)

electronic gradiometry [98], since it is much easier to fabricate a pair of HTS SQUIDs that each uses a large washer to directly couple the magnetic field to the SQUID. The outputs of two nearby HTS SQUID magnetometers can be subtracted by a differential amplifier to form a differential magnetometer [99,100], as in Fig. 17b, but this approach requires that the feedback loop of each SQUID maintain lock independently. Examples of MCGs recorded with an HTS electronic SQUID gradiometer were shown in Fig. 5. The three-SQUID gradiometer is a more elegant approach to this problem [101,102]. As shown in Fig. 17c, the three-SQUID gradiometer uses a reference SQUID and two sensor SQUIDs. The reference SQUID feeds back to the other two input circuits and cancels at each sensor SQUID the field sensed by the reference SQUID. Even if the reference SQUID is noisy, its noise is coupled equally to the two sensor SQUIDs, which can be very sensitive, and the differential amplifier removes any common-mode noise introduced by the reference SQUID. Appealing aspects of this approach are that

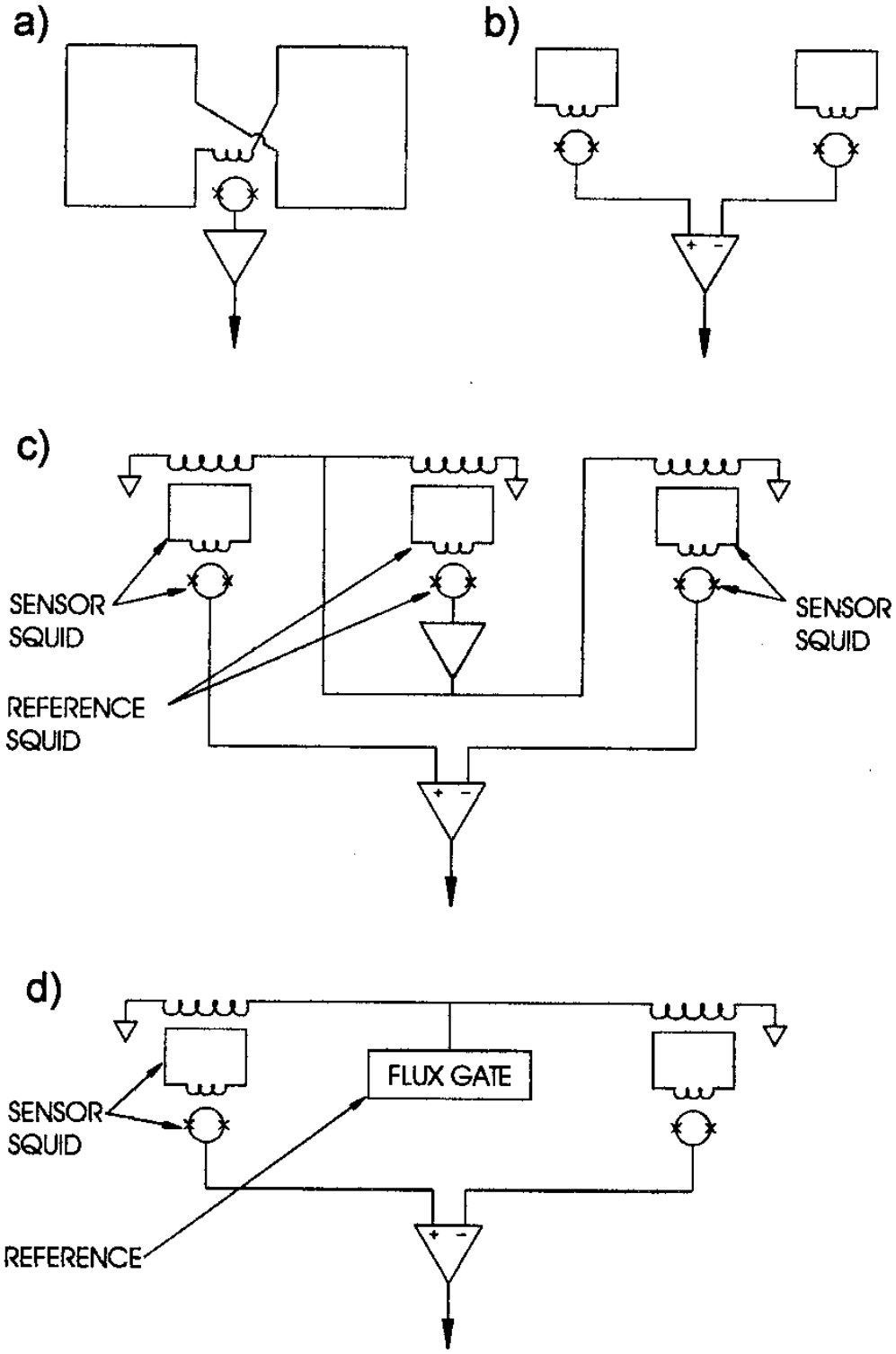

Figure 17. Three approaches to high-T_C gradiometers. a) Planar gradiometer with thin-film gradiometer pickup coil, either on the same substrate as the SQUID or as a flip chip. b) Two SQUIDs whose outputs are subtracted electronically [99,100]. c-d) Three-SQUID gradiometers [101,102] with c) a SQUID and d) with a flux gate as a reference magnetometer. (Adapted from a drawing by Roger Koch of the IBM Thomas J. Watson Research Center)

the reference magnetometer can be a flux gate magnetometer (Fig. 17d), only the SQUIDs need to be superconducting, and the SQUIDs can even be in separate dewars. When fields from distant sources must be detected, for example from submarines or mines, it is possible to achieve long-baseline gradiometers without large dewars. Thus, two high-T_c SQUIDs and a flux gate with a clever feedback system can provide a very high sensitivity, high temperature SQUID gradiometer with a high degree of balance and no need for superconducting wires.

3.3. SQUID SYSTEMS FOR BIOMAGNETISM

Although a single SQUID magnetometer can be used to map the spatial variation of the magnetic field from a repetitive, evoked process in the brain, such studies are tedious and prone to errors in determining the location of the SQUID pickup coils relative to the subject's brain. Furthermore, single channel SQUIDs are of little use in studying the spatial distribution of asynchronous electrical activity such as the alpha rhythm, or the interictal spikes that occur between seizures of epilepsy patients. This limitation was first addressed with a 5-channel SQUID system produced for Sam Williamson by BTi in 1983; subsequently, BTi introduced a pair of 7-channel magnetometers that could study signals occurring on opposite sides of the head. Unfortunately, the 7-channel systems covered only a small fraction of the cortex, and provided insufficient data for accurate localization and characterization of many sources. BTi then introduced a 37 channel system, and they subsequently developed a dewar that could be operated with the SQUIDs located above the helium reservoir so that it could be placed beneath the subject's head; thus a pair of 37-channel systems could be operated simultaneously above and below a reclining subject's head. Elsewhere, the University of Twente developed a 19-channel system [103]; a research group at the Institute of Radio Engineering and Electronics of the Russian Academy of Sciences in Moscow formed a company, Cryoton, that built a 19-channel system [104,105]; and Philips [106] in Hamburg built a double SQUID system with 31 channels in each dewar. Flat-bottomed dewars for the MCG are used in 37- and 63-channel systems built at the PTB in Berlin [21], in a 256-channel system developed at the Superconducting Sensor Laboratory (SSL) in Japan [107], and a 67-channel system (with 11 additional reference channels for noise reduction) built by BTi. The Instituto Technologie Avanzate Biomedicine (ITAB) in Chieti, Italy has built a planar system with 55 sensing channels and 22 reference channels (19 located 9 cm above the sensing plane and a triplet at 16 cm above the plane) to perform software noise compensation; all of the SQUIDS are magnetometers with a square-shaped, 9×9 mm^2, integrated pickup

coil [108]. Such systems can provide very low noise, for example the BTi system has a noise of 5 - 6 $fT/Hz^{1/2}$, while the ITAB one has 4 $fT/Hz^{1/2}$ for individual SQUIDs, and less than 7 $fT/Hz^{1/2}$ after compensation.

The real advance with SQUIDs for measuring the MEG came with the introduction of helmet-shaped dewars that have a hundred or more SQUIDs and cover much of the head. The advantage of these systems is that they provide partial or full head coverage so that you can do measurements that acquire data from multiple regions at the same time. They also reduce the length of time required for measurements. The potential advantage of using multiple signal channels for imaginative digital signal processing to eliminate noise is just now being realized [109], as we will discuss in more detail later. There are three companies that are marketing whole-head MEG systems: Biomagnetic Technologies, Inc., of San Diego, CA; CTF Systems, Inc., of Port Coquitlam, British Columbia, Canada; and Neuromag, Ltd, of Helsinki, Finland. Each has approximately a dozen whole-head systems installed worldwide.

The Neuromag system developed at the Helsinki University of Technology and being sold by Instrumentarium/Picker has 122 channels in the form of pairs of orthogonal, planar, thin-film gradiometers [95]. The use of a pair of orthogonal planar gradiometers provides excellent localization and visualization of current dipoles close to the scalp; a 306-channel system has just been introduced that has 102 sensor sites, each with a pair of orthogonal gradiometers as well as a magnetometer that can detect deeper sources than gradiometers, as was shown in Fig. 14. At present, the Neuromag system does not have reference SQUIDs distant from the scalp surface, which have been shown to be highly effective in reducing external noise, particularly when using magnetometers as the primary signal sensors.

CTF's standard whole-head system has between 64 and 151 channels, as shown in Fig. 18, with first-order gradiometers connected to SQUIDs with digital feedback, and with digital signal processing and 27 reference gradiometers to synthesize third-order gradiometers [72,96]; the more advanced systems that have been installed have 143 or 153 channels with additional reference SQUIDs; the intercoil spacing is about 3.1 to 3.2 cm, and the spacing between the 2-cm diameter pickup coils and the inner surface of the helmet is less than 17 mm. A 262-channel system, with an average inter-channel spacing of 2.3 cm, is under development [109].

BTi has as a standard product a whole-head system with 148 SQUID magnetometers and 11 reference channels for noise reduction, shown in Fig. 19. The SQUIDs and the pickup coils are located in the vacuum space outside the helium reservoir so that the system can achieve a spacing of 1.6 cm or less between the pickup coils and the inner surface of the helmet. The system is designed to cover the exposed cortex with an average interchan-

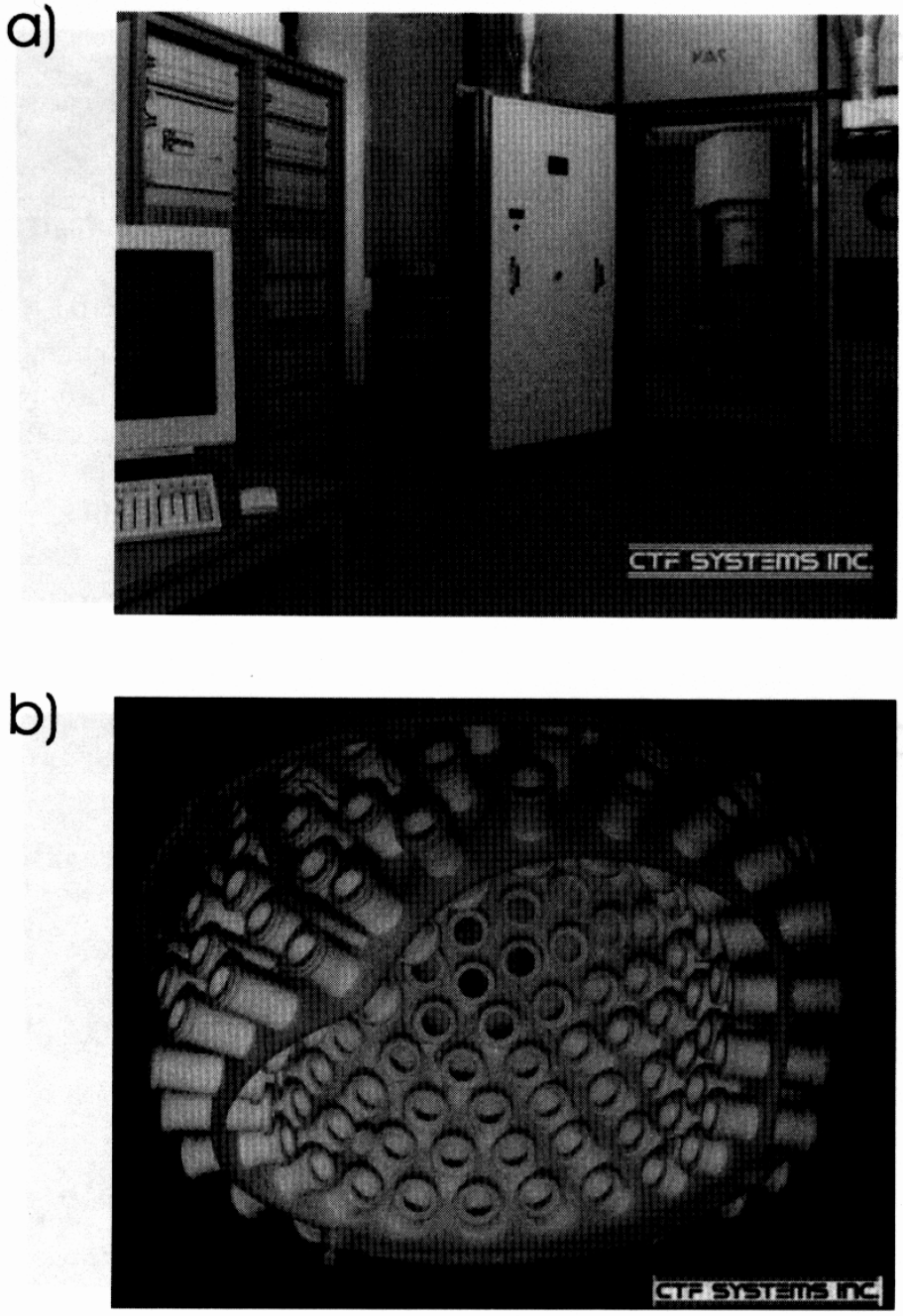

Figure 18. The CTF whole-cortex SQUID system. Top: A subject having her magnetoencephalogram recorded with the 143-channel CTF unit installed in Vienna. Bottom: The form that holds the 2-cm diameter, 5-cm baseline, first-order gradiometer coils in the 140 channel system. There is less than 17-mm spacing between the sensor coils, within liquid helium, and the outer dewar surface. (Courtesy of Jiri Vrba of CTF)

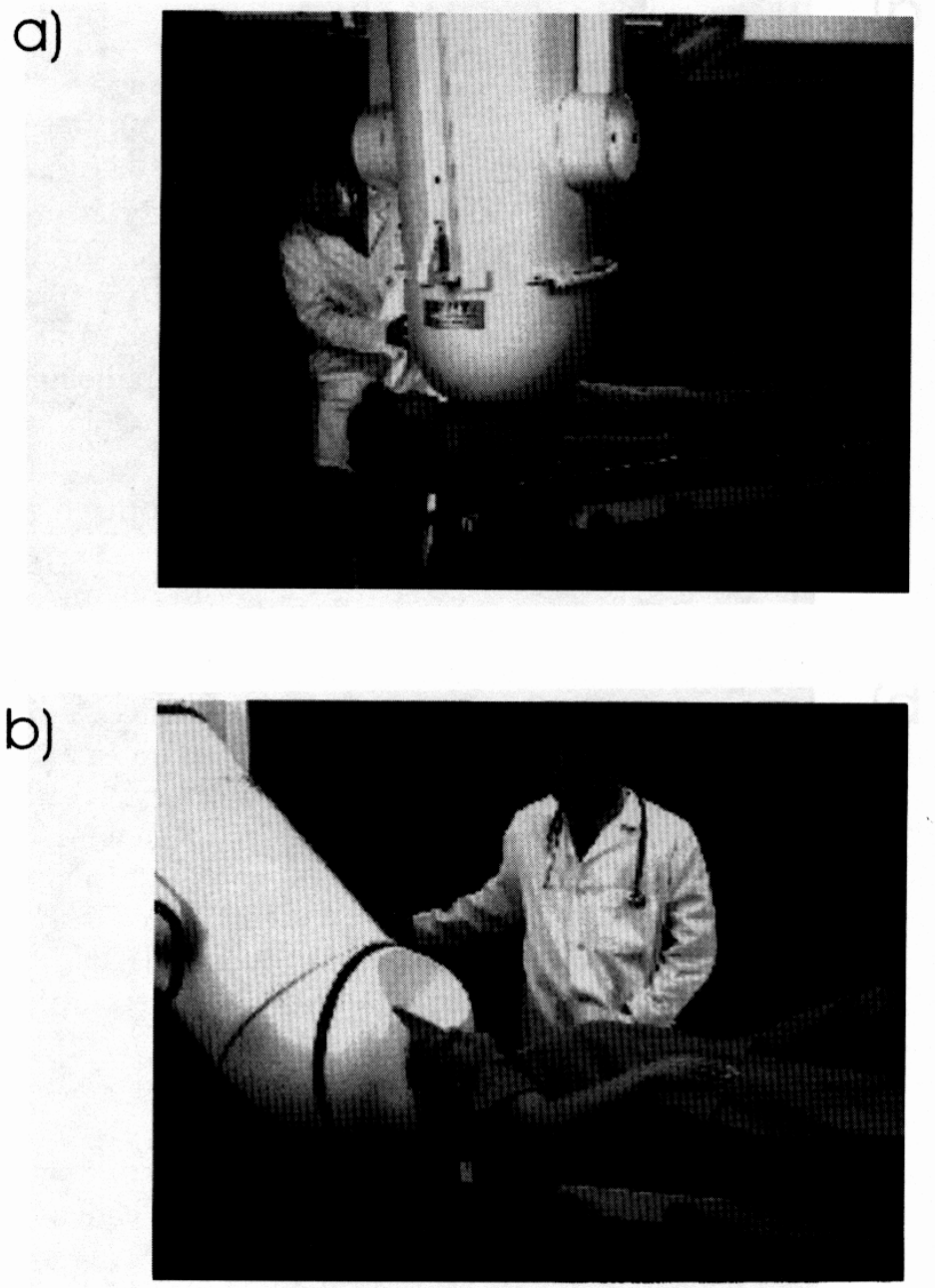

Figure 19. The BTi multichannel SQUID systems. Top: A 61-channel system designed for recording the magnetocardiogram. Bottom: The 148-SQUID helmet system for the MEG. (Courtesy of Gene Hirschkoff of BTi)

nel spacing of 2.9 cm, with 2-cm diameter coils. Because of the relatively close spacing between the coils and the head, and the use of magnetometers rather than gradiometers, the BTi system should have substantially better sensitivity to deep sources than do other gradiometer-based systems with the pickup coils in the helium. BTi is also developing an advanced system

which has 248 channels plus 17 broadly distributed references channels, all of which are radial magnetometers [110]. The coils-in-the-vacuum technology has also been used for a system designed for mapping the MCG, as shown in Fig. 19.

In addition, other groups have developed multichannel systems, such as the 256-channel SSL helmet system [111], and Kanazawa Institute of Technology (KIT) and Yokagowa 64- and 160-channel, whole-head systems for supine subjects [112]. ITAB is completing a helmet system that consists of 153 sensing channels and four orthogonal triplets located at about 7 cm from the sensing surface, to be used to form software gradiometers. The sensing channels are spread over a surface covering the whole head, with an average inter-channel spacing of about 3.2 cm [108].

The real limitation of helmet systems arises from their fixed geometry: the CTF helmets come in two sizes, one for a standard Japanese head and other for a standard Canadian head. The design of the Neuromag system was based on military studies of the distribution of head sizes of adult males in the Finnish army. As a result of variation in the size and shape of the subjects' heads, and the cryogenic difficulties encountered with building large, concave dewars, the source-to-pickup coil separation is typically larger by a centimeter or more over what can be achieved with simple, several-channel systems. As a result, the signal amplitude is reduced, and more importantly, the high spatial frequencies present in the magnetic field close to the scalp are selectively attenuated by the increased distance. This in turn reduces the spatial resolution of the instrument [113]. To counter this, BTi utilizes magnetometers rather than gradiometers in its helmet systems, so that each sensor has increased sensitivity to deep or distant sources as compared to a gradiometer configuration, and Neuromag had recently added magnetometers to its sensor array.

There is no agreement yet as to the maximum number of channels required for an MEG helmet system. CTF believes that high density arrays with more than 250 channels will be particularly useful when using advanced analysis techniques, such as Synthetic Aperture Magnetometry (SAM) or minimum norm methods [109]. The issue is the extent to which the information gained by the additional channels is offset by the increased cost and complexity. I believe that the users of the helmet systems, particularly those who study pediatric subjects or do extensive mathematical processing of the data, will eventually address the limitations posed by the increased and variable coil-to-source spacing, possibly by developing alternative approaches, such as segmented [114,115] or otherwise adjustable helmets, but this does present problems with dewar cost, increased tangential separation between the channels at the edges of adjacent segments, and multiple cryogen transfers.

The helium consumption of the present helmet systems is also significant, between 8 and 20 liters per day, due to the large surface areas where the coil-to-room-temperature spacing must be kept small, the thermal leak that arises from the six to ten wires required to operate each dc SQUID, and from the size of the neck tube in some dewar designs. This in turn can be offset by the use of closed-cycle refrigerators, with an increase in capital cost that offsets the reduced operating expenses.

It is important to recognize that these systems are becoming quite complicated and expensive: Typical systems will have two to three hundred channels of SQUID electronics, and various electroencephalogram and other signal channels that create a great deal of costly and bulky hardware. These systems also generate a tremendous amount of data quite quickly, which in turn makes demands upon data processing, display, and storage. While the CTF system is presently unique among the helmet systems in that it can be used in an unshielded environment, other systems require a magnetically-shielded room; the performance of the CTF system is improved within a shield. Helmet systems cost between one and two million dollars, and the cost of the shield can increase this by another half million dollars. Thus, the helmet systems are just that: major systems with all the inherent problems of systems integration and escalating costs; the SQUIDs and their electronics probably contribute only 10% of the total cost! Just as MRI systems utilize superconducting magnets that are becoming increasingly invisible to the customer or the patient, MEG systems are using SQUIDs that will become less significant to the product than the overall clinical capabilities of the modality and the user-friendliness of the software that analyzes the data. This is good, if the technology is ever to be widely accepted.

3.4. SQUID SYSTEMS FOR NDE

Several companies build SQUID systems specifically for NDE, designed either for use in the laboratory or in the field. In contrast to biomagnetism, where system sensitivity and total number of channels are of the greatest importance, for NDE sensitivity is not generally an issue, since the strength of the signal can most often be controlled by the strength of an applied field or current. Multiple channels would be convenient, but are not generally necessary because the signals are regular rather than stochastic. The primary challenge for SQUID NDE systems is spatial resolution, which affects the ability of the system to identify small flaws and discriminate between a flaw and adjacent structural details or spatial variations in material properties.

3.4.1. *SQUIDs for Laboratory NDE*

The spatial resolution of SQUIDs has been increasing steadily for the past decade. The greatest advances in SQUID resolution came with the development of several scanning SQUID microscopes, in which an HTS or LTS SQUID is positioned within a few microns of a cryogenic sample, or several tens of microns from a room temperature one. These systems and many of the measurements done with them are reviewed in detail elsewhere [13].

The first high resolution SQUID used for NDE and biomagnetism, MicroSQUID, was built for me by BTi and Quantum Design, and has four, 3-mm pickup coils 1.5 mm from room temperature [116]. The Strathclyde group has also built a high-resolution system for NDE [117]. Quantum Magnetics (QM) developed a five-channel High Resolution Scanning Magnetometer (HRSM) that is designed to scan a corrosion cell in an unshielded environment [118,119]. The system is equipped with a custom-made fiberglass-epoxy translation stage. The stepper motor controller and the data acquisition process are controlled by a desktop computer.

Our group at Vanderbilt has developed several other SQUID systems for laboratory NDE measurements [7,120,121]. The most recent one is optimized for the measurement of the spatial and temporal dependence of the magnetic fields associated with hidden corrosion in aircraft lap joints [122]. The system, shown in Fig. 20, uses a Conductus, three-axis vector gradiometer, and includes a magnetic shield, a scanning stage with a custom sample-handling system, a computer control system, and custom scanning and analysis software. Such a laboratory instrument requires a significant effort in devising the experimental procedures required for SQUID measurements on corroding systems, including sample design for calibration studies, kinematic techniques for accurate repositioning of multiple samples, moisture delivery systems such as tubing, wicks and valves, techniques for gas venting, effective seals and sealants, sample preparation procedures that minimize magnetic contamination, sample chambers for lap joints that provide controlled temperature and humidity, and techniques for identification and minimization of magnetic contamination. We will present data obtained with this system in a later section.

3.4.2. *SQUIDs for Field Deployment*

Tristan Technologies, Inc., transiently Conductus Instrument and Systems Division San Diego, has developed a number of specialized NDE systems, such as a 6-channel NDE system with 1 mT ac and 0.1 T dc magnets and a small dewar that can be held by a robot moving within a nuclear reactor.

The SQM Technology electromagnetic microscope has an ac source coil and a pickup coil on the end of a flexible thermal link connected to a closed-cycle refrigerator [44,82]. A 2-mm diameter, differential pickup consists of

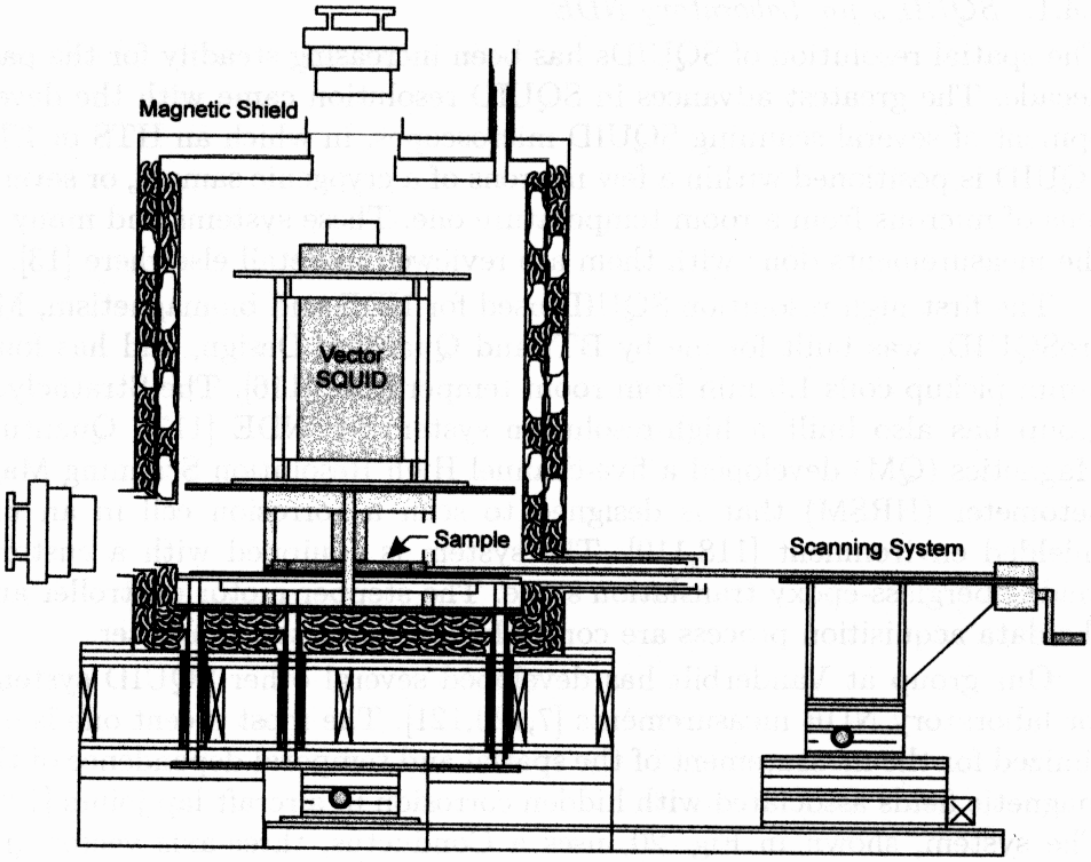

Figure 20. A schematic drawing of the Vanderbilt Corrosion SQUID system. The SQUID is supported in the center of the shield by a framework of G-10 and aluminum. The kinematic design of the frame simplifies the adjustment of rotation and tilt of the pickup coils with respect to the scanning coordinate system. The shield is mechanically isolated from the scanning system to prevent contact-induced vibrations. (From [122], with permission)

two counterwound, semicircular loops. Current oscillation in a 10-turn, 10-mm diameter superconducting source coil concentric with the pickup, induces eddy currents in conductive objects under test. A 16-mm coil is for compensation. Axisymmetric currents induced in unflawed test pieces generate a null response in the gradiometer pickup; flaws break symmetry and produce a signal.

The greatest progress in the development of field-deployable HTS SQUID systems has been made by Dr. Joachim Krause and his group at the Institut für Schicht-und Ionentechnik (ISI) of the Forschungszentrum Jülich in Jülich, Germany. Figure 21 shows the mobile cryostat developed for them by ILK, Dresden, and the scanning system in use on an aircraft fuselage [67]. The Tristan hand-held high-T_c system in Fig. 22 is an example of a compact, portable SQUID system that could be field-deployed.

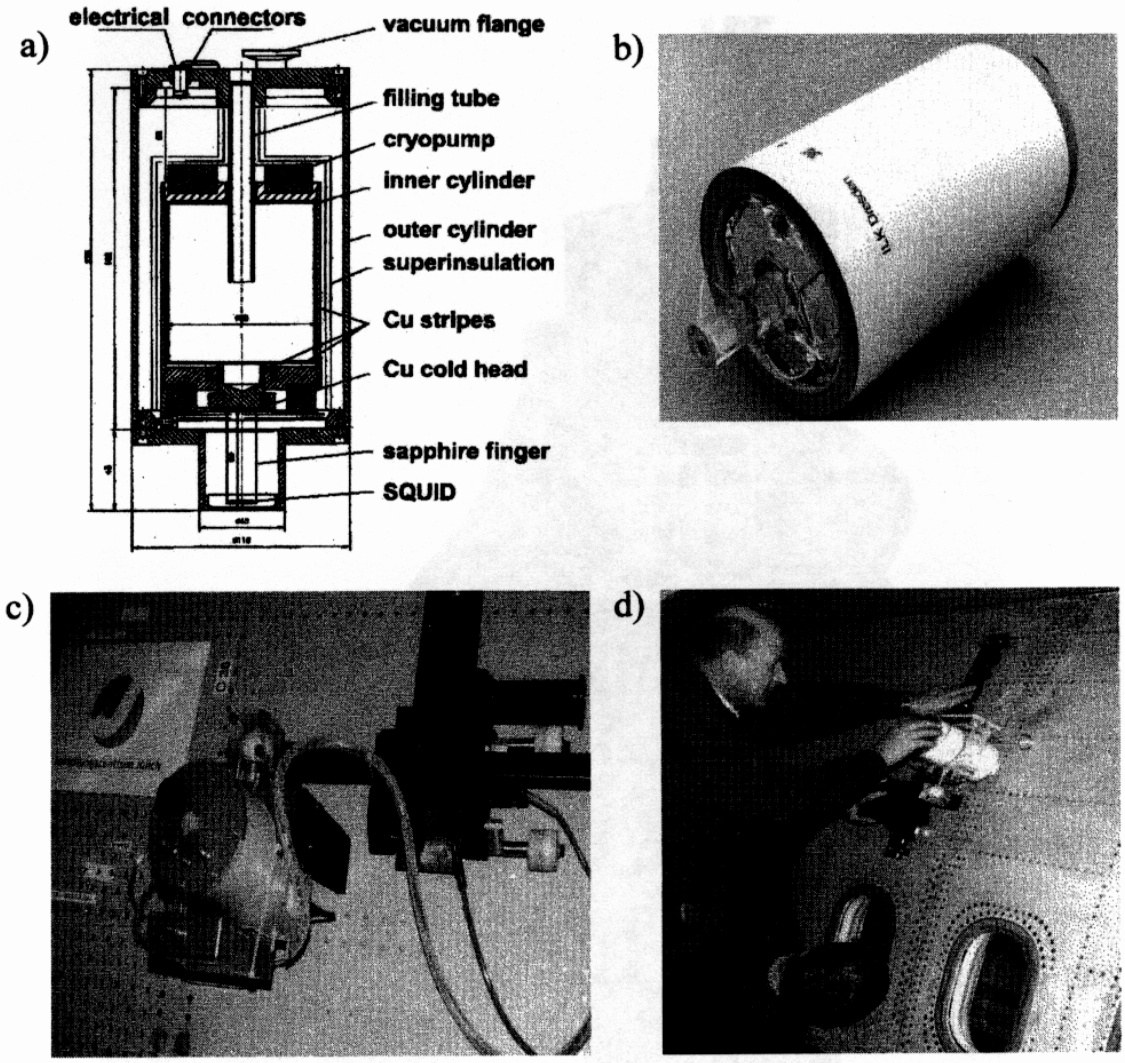

Figure 21. The Jülich field-deployable NDE system. a) A schematic drawing of the *Mobile Cryostat ILK 4*. b) A photograph of the cryostat with the tail and lower flange removed to show the sapphire cold finger and the SQUID. c) and d) The cryostat and scanning system in use on an aircraft fuselage. (Adapted from [67], with permission)

4. Modeling of Sources and the Inverse problem

When a SQUID is used to map the magnetic field above a nearby, two-dimensional source, such as a current distribution or a magnetized sheet, there is in general a readily-interpretable correlation between the magnetic field and the underlying sources. For complex three-dimensional sources such as the brain or a complex object undergoing non-destructive evaluation, SQUIDs do not usually present as their immediate output a three-dimensional image that is readily interpreted and correlated with the structure of the object being imaged. This difference between SQUID imaging

Figure 22. A hand-sized liquid nitrogen dewar developed by Tristan Technologies, Inc. that has a single high-T_c SQUID in it. It has an 8-hour hold time when vertical and a 4-hour hold time in any other orientation. (Courtesy of Robert Fagaly, Tristan Technologies, Inc.)

and many other medical and NDE imaging modalities such as x-rays, MRI, and ultrasound arises because the magnetic fields that are detected by SQUIDs obey Laplace's equation, and as a result, there is no unique solution to the three-dimensional inverse problem of determining the source of the magnetic field from the field itself. For this reason, magnetic measurements with SQUIDs on three-dimensional sources have come to rely heavily on mathematical modeling. In this section, we will describe several types

of models that are used for both biomagnetism and NDE.

4.1. MODELING OF BIOMAGNETIC FIELDS

Much of the MEG work to date has been done by looking at biological signals from sources that are highly localized in space, and hence are suitable for analysis as a single electric dipole. In these situations, the observed field pattern is simple and is strongly suggestive of a dipolar source, but with unknown strength or depth. As an example, cognitive science studies benefit from determining the location of the cortical neurons that respond first to a particular auditory or visual stimulus. The potential for MEG to locate such sources was clearly demonstrated in the early studies by Sam Williamson and Lloyd Kaufman at New York University [123–126]. If one uses the rather drastic simplification that the head can be modeled as a sphere, information about the depth of the source can be obtained directly from a map of the component of the magnetic field that is perpendicular to the scalp: in this approximation, the effective source dipole lies midway between the maximum positive and negative values in the MEG map, at a depth that is $\sqrt{2}/2$ times the spacing between the two extrema shown in the isofield pattern in Fig. 2d. While this approximation was used extensively in early MEG studies and it still provides useful results for some regions of the head, such as over the visual cortex at the back of the head, more advanced models that account for the non-spherical shape of the inner surface of the skull are more uniformly applicable. Because of the high conductivity of the scalp and the low conductivity of the skull, such simplistic models have not proven useful for the electroencephalogram. As shown by Fig. 23, the ability to localize sources from the MEG is improved by using more realistic models of the head that include the shape of the head surface, and the inner and outer surfaces of the skull; typical accuracies for a single-sphere model are on the order of 0.5 cm at the cortical surface, and 2.5 cm near the center of the head, whereas an accuracy of 0.23 and 0.5 cm can typically be achieved using a realistic three-layer model [127,128]. It is worthwhile to note that while there have been a number of studies to ascertain the localization accuracy of the MEG, the accuracy of the competing, conventional imaging techniques is not widely studied – one study demonstrated that MRI images of the head had an average 1 to 1.5 mm distortion due to field gradients [129], dependent in part upon the pulse sequence and field gradients used.

The fundamental limitation of dipole models is that some sources either are not dipolar, or are distributed over such a large area that the dipole moment conveys only a fraction of the information about the nature of the source. A detectable interictal spike from an epilepsy patient may be the

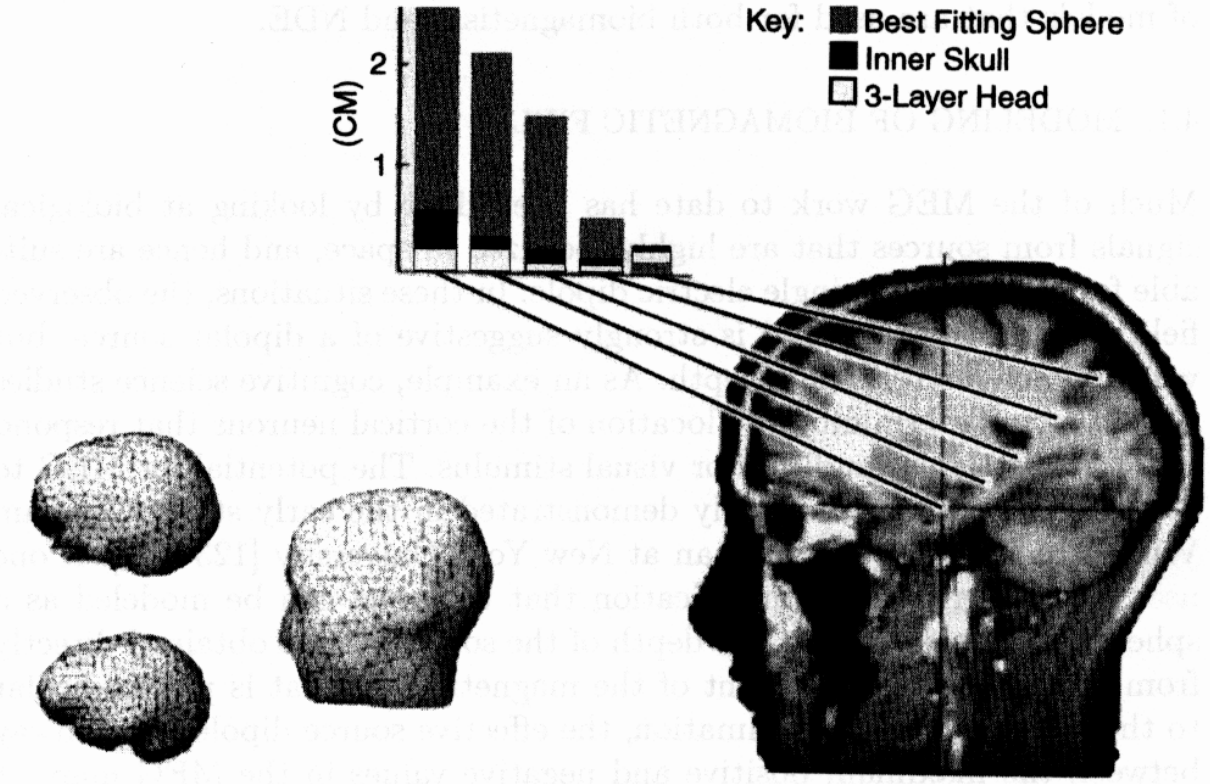

Figure 23. Error in dipole localization for head volume-conductor models of increasing anatomical realism [128]. a) A series of computational meshes defining major conductivity barriers in the head: the head surface, the outer and inner surfaces of the skull. These meshes are used for boundary integral computations of the head surface potential and magnetic field distributions due to current dipoles at arbitrary locations and orientations within the head. b) A series of assumed dipole sources relative to an MRI anatomical rendering. The input data from the forward model simulated a 127-channel SQUID system with a 10:1 signal-to-noise ratio. The bar graphs illustrate the error for each source location for three models: the sphere that best-fits the inside of the head, a single-surface model representing the inner surface of the skull, and the full three-layer model. (Courtesy of John George of Los Alamos National Lab)

result of the simultaneous activation of as much as 6 cm^2 of cortical surface [130,131]. The temptation is then to attempt to solve the generalized inverse problem of determining the distribution of cortical currents that produced the magnetic field. Unfortunately, this problem has no unique inverse solution, and can be solved only with the addition of physiological constraints or mathematical regularization. A variety of approaches have been taken. Figure 24 shows the output of the Los Alamos MUltiple SIgnal Classification (MUSIC) algorithm [132]. Figure 25 compares the three types of minimum norm solutions; the success of the FOCUSS (FOCal Underdetermined System Solution) algorithm demonstrates that a series of carefully designed constraints, including that the number of active generators not exceed the number of measurements, can produce reasonable

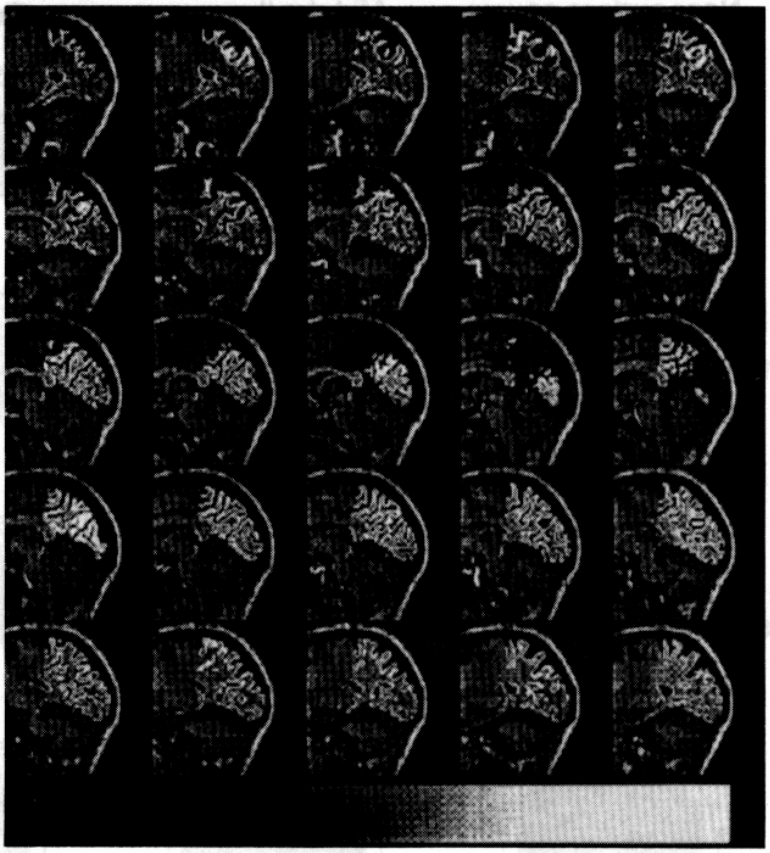

Figure 24. The Los Alamos MUltiple SIgnal Classification (MUSIC) algorithm [132]. Slices of the MRI anatomy with superimposed, as brighter regions, the values of the cortically constrained MUSIC metric - a functional measure derived from MEG in a series of slice images. MUSIC allows assessment of the distribution of probability of a dipole source by systematically scanning a predefined grid. By adding constraints based on the location and orientation of the local cortical surface, the MUSIC metric becomes more diagnostic, with sharper peaks corresponding to (relatively) localized regions of neural activity. This figure illustrates a region of the occipital lobe of the brain and suggests several discrete areas of activation. (Courtesy of John George of Los Alamos National Laboratory)

reconstructions for certain types of source distributions [133]. More recent FOCUSS results [134] are shown in Fig. 26. Synthetic aperture magnetometry (SAM) is a recently introduced technique, illustrated in Figure 27, that uses adaptive beam-forming techniques to estimate the source power and uncorrelated noise variance at specified coordinates in the head [135]. As described by Steve Robinson, SAM is not an inverse solution, as it does not fit all source parameters to account for the measured data. Instead, SAM behaves as "spatially selective noise reduction." For each coordinate selected inside the head, SAM attenuates all signal except for that of the selected coordinate. Thus, external magnetic noise and brain noise have negligible effect on the estimated source strength. A tomographic image of

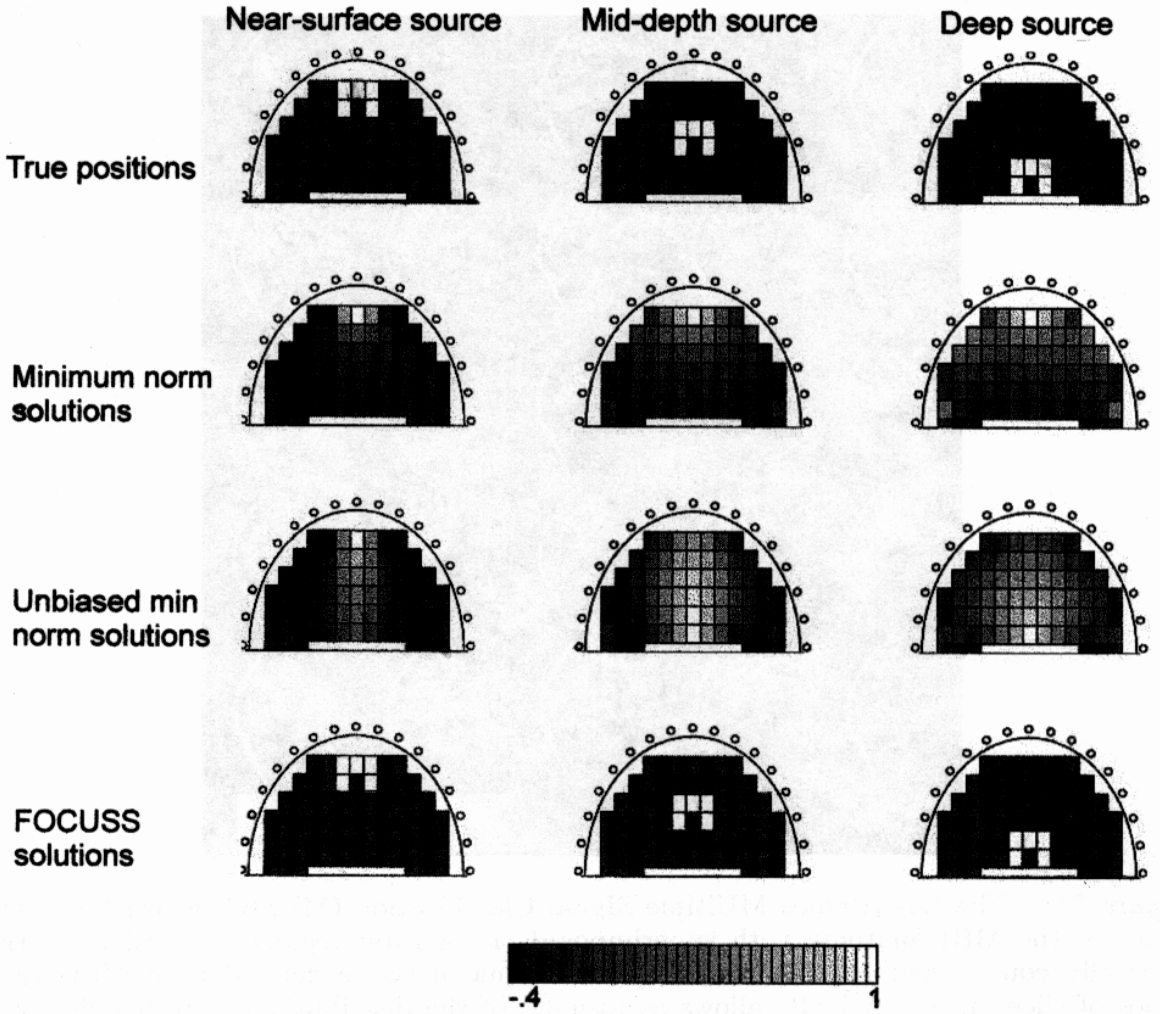

Figure 25. Reconstructions achieved with different techniques for an extended source at different depths [133]. Each column illustrates a different depth source, and each row illustrates a different reconstruction method (minimum norm, unbiased minimum norm, and FOCUSS (FOCal Underdetermined System Solution) solutions; the top row is the simulated current distribution. Each sub-image is normalized by dividing each element by the maximum value in the image. (Courtesy of Irina Gorodnitsky of the University of California, San Diego)

source current is built by "scanning" coordinates within the head [97]. The appeal of this approach is that it offers stable and reproducible functional images, albeit with a reduction in time resolution as compared to the raw MEG, without requiring the use of dipole models. It is important to note that the competing functional techniques, positron emission tomography (PET) and functional magnetic resonance imaging (fMRI), have response times substantially less than the MEG and are considered the gold stan-

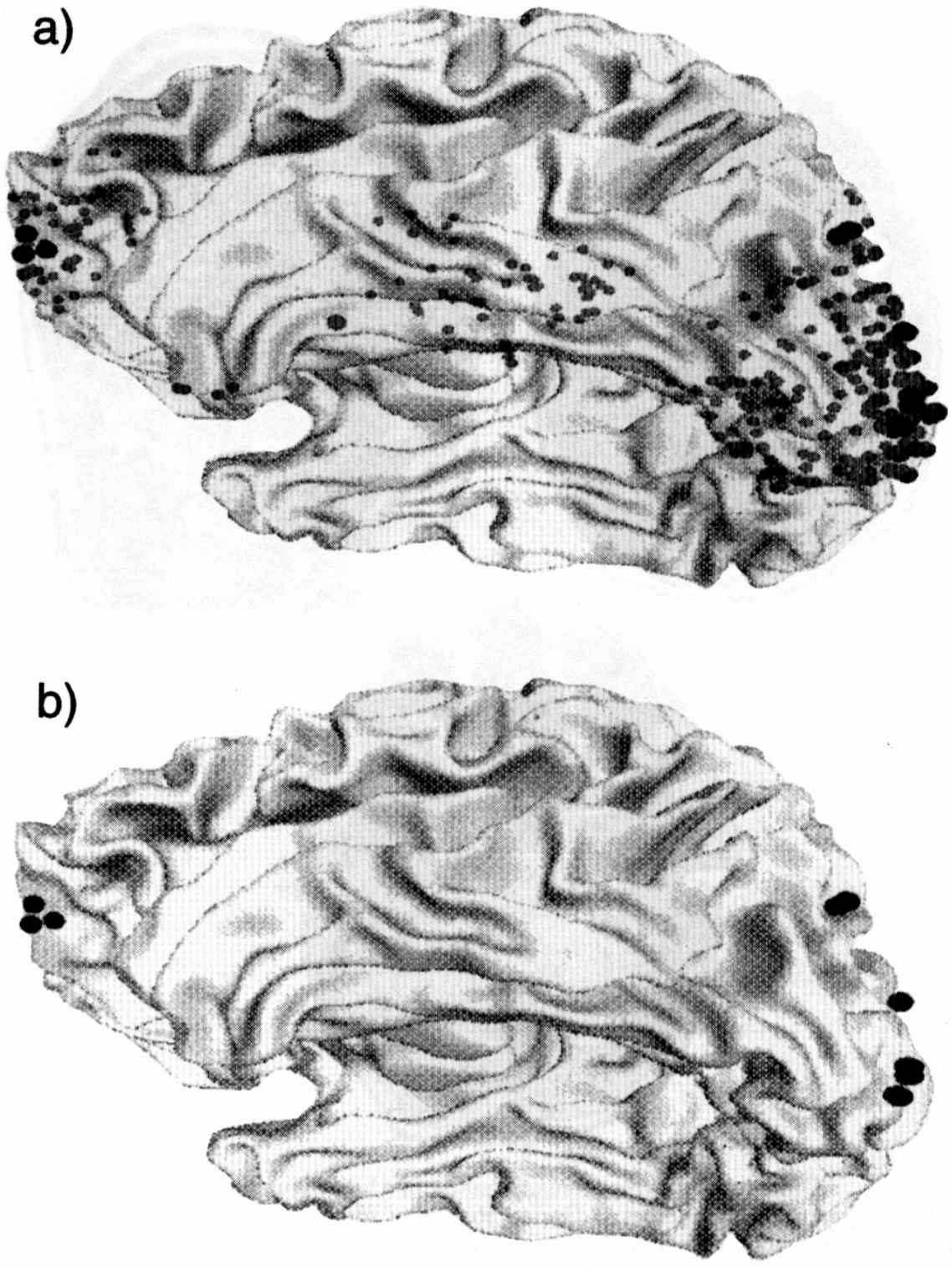

Figure 26. MEG reconstructions of three neuronal ensembles represented by 3, 2 and 4 active nodes, respectively, with a 150-sensor array. (a) The solid black circles mark the nodes of the three active sites. The weighted minimum norm solution that includes a compensation for the bias as described in the text is marked by gray transparent circles. (b) FOCUSS reconstruction of the active nodes shown in solid black circles. (From [134], with permission)

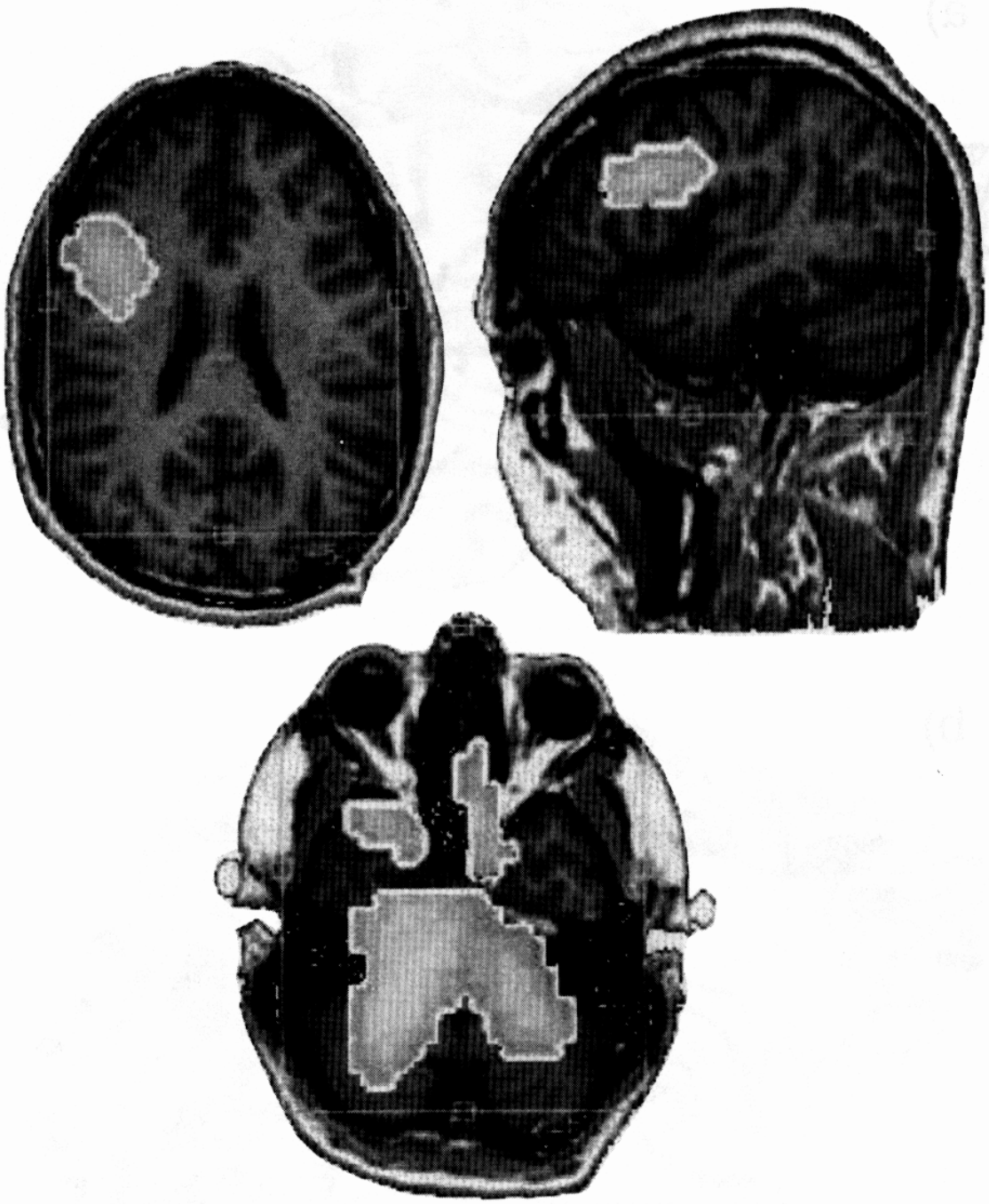

Figure 27. Differential current-density maps of the language center, obtained with synthetic-aperture magnetometry. Upper: Region of focal suppression of source activity, slightly superior to Broca's area. Lower: A region of activation at the posterior, apparently due to the cerebellum. Data are from one, unaveraged six-minute collection. (Courtesy of Steve Robinson and Jiri Vrba of CTF)

dards of noninvasive functional imaging. There should be a large number of applications of this technique to cognitive and clinical MEG studies [136].

There are other numerical approaches to MEG inverse imaging, such as the minimum-norm least-squares (MNLS) approach [137,138]. Work on improved inverse calculations should prove to be a fruitful area of research

for years to come.

4.2. MODELING FOR NDE

Modeling has proven useful in SQUID NDE to assess the various contributions to the observed signals. For example, Fig. 28 shows how SQUIDs can be affected by the structural details of the system under test, and how properly-configured gradiometers can separate the flaw signature from that of the underlying structure [94]. Models have also demonstrated that cancelation plates can be used for removing edge effects when current is injected into some conducting shapes [139].

Other models have been used to study the magnetic signature of cracks in metal plates and tubes, the effects of excitation frequency and detection phase on the detectability of subsurface cracks in aircraft aluminum [38–40,43,45,140–143], and to examine the factors that affect the probability of detection of cracks in aircraft [144–147].

5. Applications

Now that we have described how SQUIDs are built, where the signals come from, and how signals can be interpreted, we can look at applications of SQUIDs to biomagnetism and NDE. We will not present an exhaustive list, but instead will describe a number of specific applications that most clearly present unique capabilities of SQUIDs.

5.1. APPLICATION: BIOMAGNETISM

The earliest biomedical application of a SQUID magnetometer was to measure the magnetic field of the human heart, recorded as the magnetocardiogram (MCG) [1]. As we will discuss later, there have yet to be definitive demonstrations of the clinical utility of the MCG and it is not widely used outside the research setting. In contrast, there are a number of research groups and clinical facilities that are actively pursuing studies of the magnetoencephalogram (MEG) for both basic research in neuroscience and for clinical medicine. A promising application is the measurement of the magnetic field from the spontaneous electrical activity of the gastrointestinal tract, recorded from the stomach as the magnetogastrogram (MGG) and from the small intestine as the magnetoenterogram (MENG). There are a number of *in vitro* laboratory applications as well. We now touch on each of these.

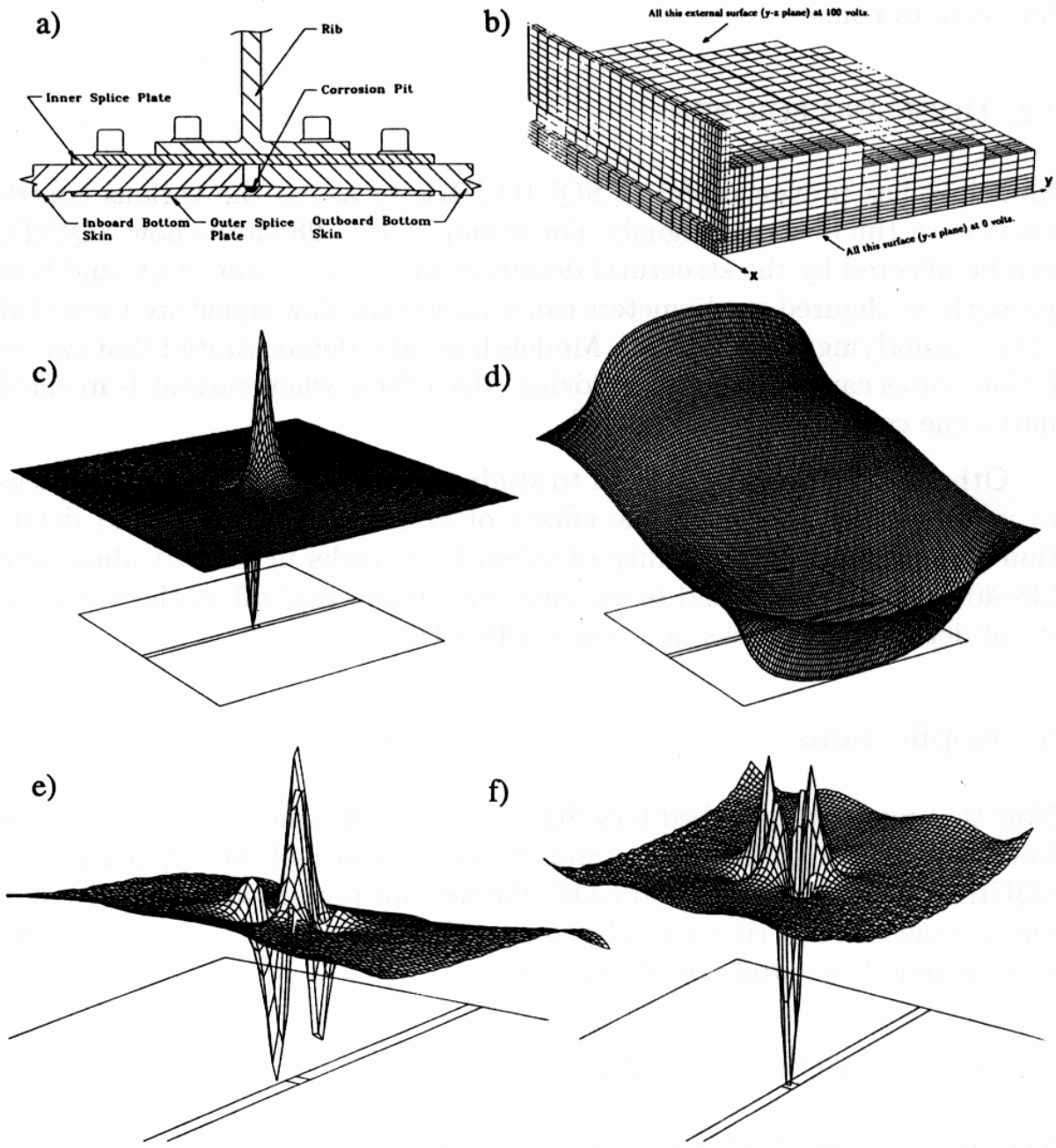

Figure 28. Simulations of the magnetic signature of a small region of hidden corrosion in an F-15 lower wing splice. a) Schematic cross-section of the splice. b) The finite element mesh describing one-quarter of a section of wing splice. A uniform current is applied parallel to the x-axis. c) The magnetic signature of the flaw alone. d) The magnetic field from the wing structure and the flaw. The peak-to-peak signal arising from the edges of the various plates in the splice is 400 times larger than that of the flaw. e) and f) The simulated output of two SQUID gradiometers configured to reject large-scale spatial variations such as from the wing structure and selectively detect fields from localized flaws. (Adapted from [94])

5.1.1. *Cognitive Science*

The first significant application of SQUIDs to neuroscience was to map the location of regions of cortex activated by a specific stimulus [123,124]. These and other studies have shown that many such cortical current sources are highly dipolar, and hence can be interpreted with simple models. Examples of the use of SQUIDs in neuroscience include providing a noninvasive, tonotopic map of the response of the auditory cortex to auditory stimulation at different frequencies [125], studies of tonal memory [148,149], brain activity during eye blinks [150] and picture naming [151], mapping of the visual field on the retina onto the cortex [126], and mapping of the hand and face to the cortex. As shown in Fig. 29, the application of a nonmagnetic mechanical stimulator to various points on the hand allows the SQUID to map the locations on the brain that correspond to the hand locations [152]. Similar studies on subjects who had one arm amputated showed that the signals from the face and shoulder for the amputated side had moved closer together, and overlapped into the space that would have otherwise corresponded to the hand, providing the first direct demonstration of cortical plasticity in humans, and proving that some phantom sensations from the amputated limb arise from the cortex [153].

5.1.2. *Clinical applications*

A wide variety of clinical applications of biomagnetism have been examined in neurology, including studies of epilepsy, stroke, trauma, and the recording of signals from the spinal cord, nerves, and skeletal muscle. The practical aspects of such measurements are reviewed elsewhere [154]. One of the problems with the acceptance of magnetometry as a clinical tool is the length of time that it has taken to demonstrate clinical utility. This is hard in any single field, and biomagnetism is being applied to many different ones. More importantly, because the technique represents a significant departure from existing clinical techniques, and few clinical centers will purchase an expensive and unproven instrument, corporate involvement has been required in developing clinical applications. Even so, there are several dozen research or clinical centers worldwide that are active in biomagnetic recordings. For example, there are about twenty-five sites with BTi whole-head or cardiac or Magnes I or II systems, some of which are clinically oriented with regular patient flow of 3 to 5 patients a week, and others that are more research oriented and have possibly only 2 to 3 subjects a week with long periods of setup or evaluation between acquisitions. If these sites together produce between 50 to 60 recordings made per week on patients and normal volunteers, there could be perhaps 2500-3000 recordings per year using BTi instrumentation [110]. Given the instrumentation produced by other firms, at least 4,000 MEGs and MCGs should be recorded annually worldwide.

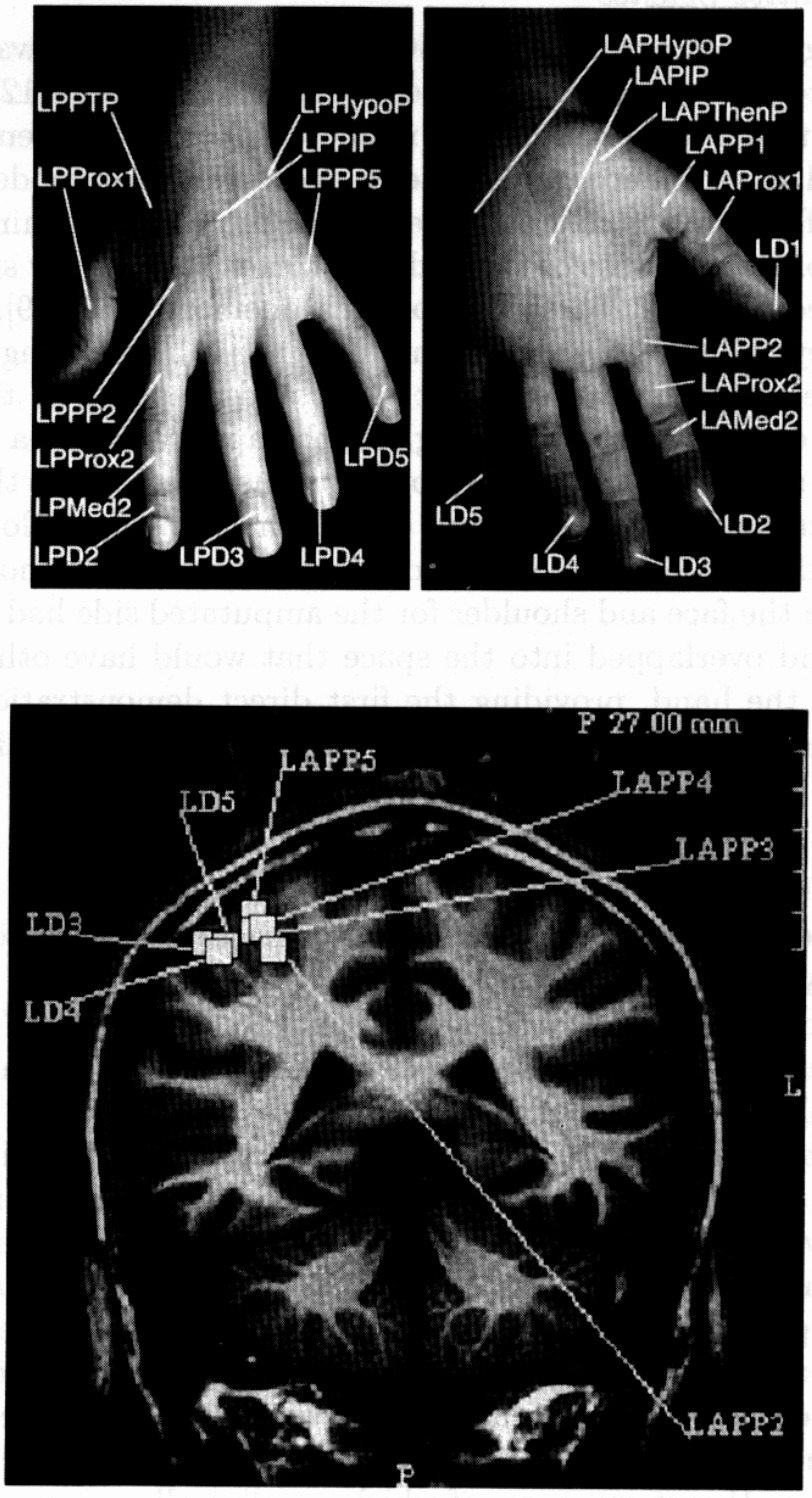

Figure 29. Demonstrations of noninvasive mapping of hand stimulation sites onto the cortex [152]. Top: Sites of mechanical stimulation; Bottom: the sites of cortical response. (Courtesy of Christopher Gallen, formerly of the Scripps Institute, and Gene Hirschkoff of BTi)

The first application that has been clinically proven and recognized for third-party reimbursement is the presurgical functional mapping for brain tumors, arteriovenous malformations, and epilepsy, in which the MEG is used to identify key regions of functioning cortex before they are inadvertently removed or otherwise damaged during surgery. This procedure is now accepted by a number of insurance companies - in part because there is a 20% morbidity rate for the 100,000 intracranial surgeries performed each year, and the MEG is proving useful for reducing the risk. Presurgical mapping can be considered a routine, reimbursed procedure that is used regularly in eight or more clinical MEG centers in the US and one in Japan. However, it does not appear that the need for presurgical mapping is sufficiently great on its own to justify the MEG as a successful commercial instrument [110].

Clinical applications that are still in the process of being proven include the use of the MEG to provide a more definitive diagnosis of stroke, head trauma, and transient ischemic attack (TIA) in the brain, and the use of the MCG to localize and classify cardiac arrhythmias. Promising applications that are just now being examined include the use of SQUIDs for fetal heart monitoring [155,156], for measuring the fetal MEG [157], studies of the signals from the spinal cord and peripheral nerves [158–160], the diagnosis of bowel function disorders [161], and the study of schizophrenia and metabolic brain disorders such as uremic or hepatic encephalopathy. I will now discuss some of the applications in more detail.

Studies of the brain. Because patients with epilepsy often exhibit electrical spiking in the interictal period between seizures, substantial effort has been directed toward using the MEG to localize the site of origin of the spikes, which is believed to coincide with the site of origin of the seizure. Early studies by groups in Rome and at UCLA demonstrated the validity of this approach [162,163]; Fig. 30 shows how a helmet MEG system can quickly localize the source of the spikes, and also shows how the mirrored activity on the left side of the brain of the subject being studied lags after the activity on the right side [164].

A potentially important application is the use of the MEG to diagnose head trauma and damage from transient ischemia [165–167]. The activity of the normal brain is dominated by alpha waves in the 8-13 Hz range. Patients with neurological disorders often show slowing of the EEG, and also show extensive, large amplitude, abnormal low-frequency magnetic activity (ALFMA) in the theta and delta range. The MEG ALFMA examination is quite sensitive to demonstrating pathophysiology in these patients. Many patients who suffer mild traumas have normal MR and CT examinations, but significant post-concussive psychological changes. As an example, the circles in Fig. 31a correspond to the locations of ALFMA activity at 2.5

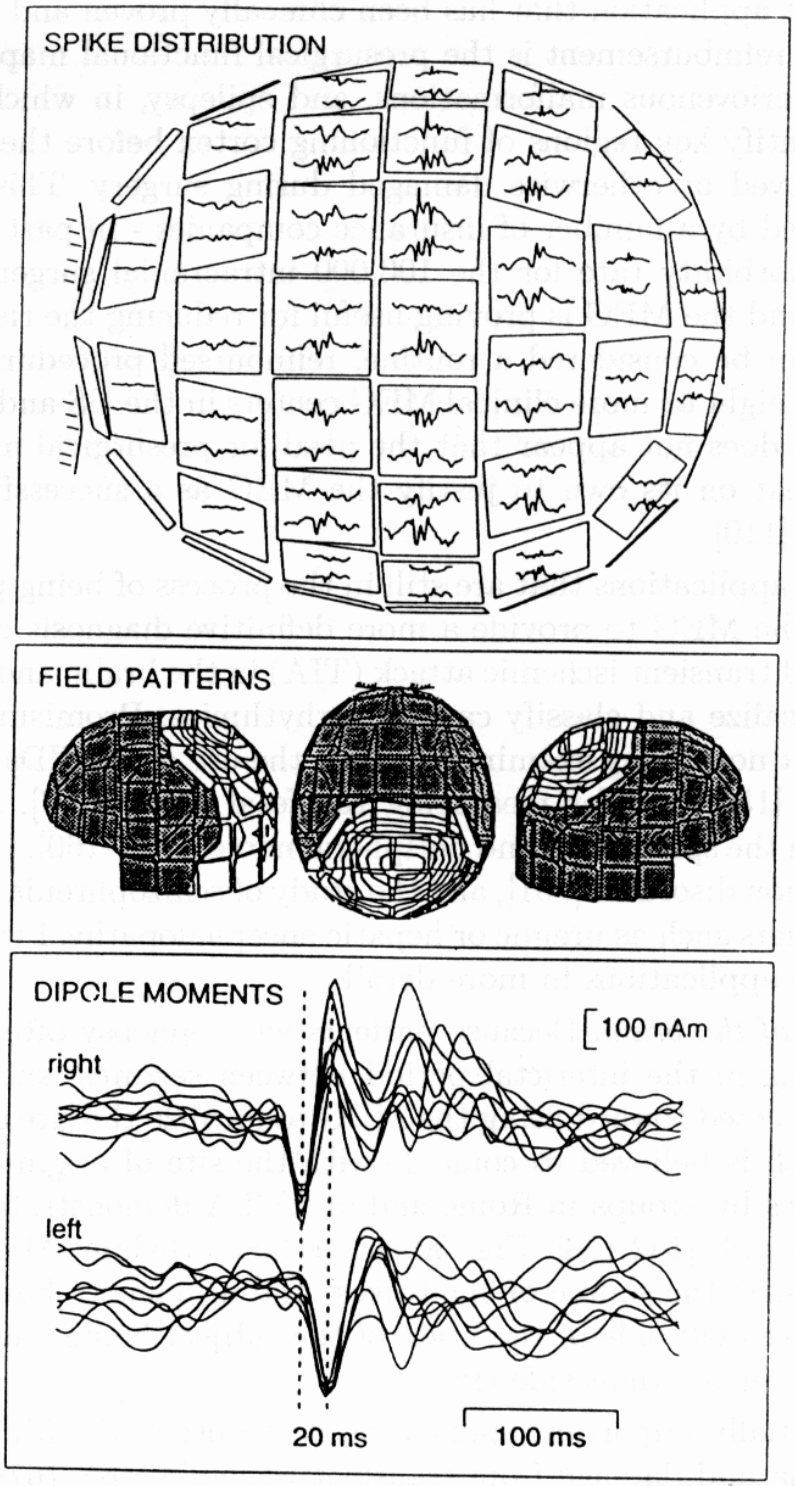

Figure 30. Top: Spatial distribution of one interictal spike displayed on the sensor array; only about half of the measured signals are shown in this projection. The two traces on each sensor unit illustrate the two orthogonal derivatives of the magnetic field measured at that location. Middle: Field patterns during a single time moment of one spike. The sensor array is viewed from the left, from above, and from the right. The shadowed areas indicate magnetic flux emerging from the head; the isocontours are separated by 400 fT/cm. The arrows indicate the sites and orientations of the two equivalent current dipoles required to account for the field pattern. Bottom: Dipole moments as a function of time in both hemispheres. Each trace corresponds to one unaveraged spike, whose distribution was explained by the two-dipole model. (From [164], with permission)

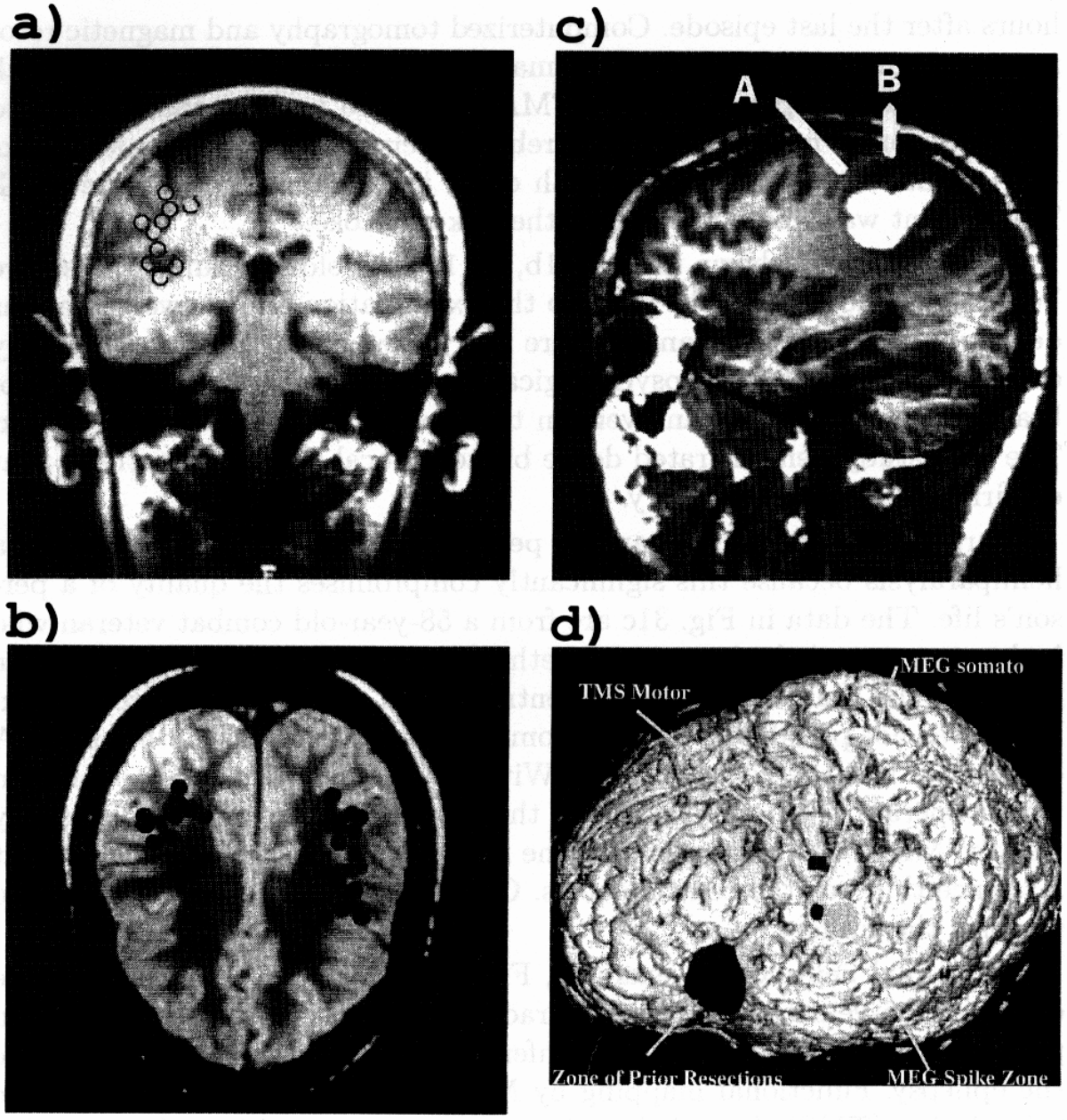

Figure 31. Examples of the use of the MEG recorded with the BTi 37-channel Magnes^{tm} system for clinical diagnosis and treatment [167]. a) Sites of abnormal low frequency magnetic activity in a 65-year-old woman with transient facial numbness and slurred speech. b) Magnetic source imaging of focal slow-wave activity, indicated by the dots in one of several different slices of the MRI scan, in an 18-year-old boy 3 months after a severe beating. c) Magnetic determination that the location of the central sulcus that contains the somatosensory cortex was at A and not B, thereby allowing surgical resection of the tumor. d) Magnetic determination that the source of recurring, intractable epileptic seizures was a previously unnoticed vascular malformation far from the site of two previous resections. (Courtesy of Jeff Lewine and BTi)

Hz in a 65-year-old woman who had three episodes of facial numbness and slurred speech within the four hours prior to her admission to the hospital. Her clinical symptoms resolved by the time she went to the hospital 10

hours after the last episode. Computerized tomography and magnetic resonance imaging could find no abnormalities. Magnetic source imaging with MEG found multiple sites of ALFMA slow-wave activity that confirmed the suspicion of multiple middle cerebral artery transient ischemic attacks (TIAs) that were undetectable with other imaging methods or the EEG. The patient was treated to reduce the risk of stroke.

In the example shown in Fig. 31b, an 18-year-old boy suffered a severe beating at school 3 months prior to the examination and showed a serious decline in school performance. There was no evidence of traumatic injury on EEG, CT or MRI, yet psychological tests supported the explanation of brain trauma instead of an aversion to school for fear of repeated attack. The MSI study demonstrated dense bilateral focal slow-wave activity that confirmed serious brain injury.

Surgeons are very reluctant to perform operations that may cause a hemiparalysis because this significantly compromises the quality of a person's life. The data in Fig. 31c are from a 58-year-old combat veteran who had a tumor, and the issue was whether the tumor could be resected. The groove in the brain known as the central sulcus contains the motor cortex, but it was not possible to discern from anatomical images whether point A or point B was the central sulcus. Without this identification, no surgeon would operate. The only technique that could identify that noninvasively was the MEG, which showed that the motor signals from the hand were at A; hence this was the central sulcus. Given this data, a surgeon agreed to perform the surgery.

As a final neurological example, Fig. 31d shows an MRI image of the cortex of a 5-year-old male with intractable partial-complex seizures. Two prior surgical interventions in the inferior frontal cortex failed to alleviate the epilepsy. Functional mapping by MEG and Transcutaneous Magnetic Stimulation (TMS) showed that the resection zone could not be extended more posteriorly without compromise of the motor cortex. However, the MEG showed that the epileptic activity was arising from a region far removed from the prior resection zones. Re-examination of the patient's MRI data showed a small vascular malformation in this region that had been previously overlooked. Surgical intervention in this area has controlled the patient's seizures. There are obviously many other potential applications of the MEG to clinical neuroscience, for example the study of migraine headaches [168].

Cardiac Studies. The magnetocardiogram, shown for example in Figs. 4 and 5, has a waveform that is similar to that of the electrocardiogram (ECG). To first order, the electrical activity of the heart produces a spatial distribution of the electric field on the torso surface that is dipolar, with the electric (current) dipole moment, termed the electric heart vector, pointing

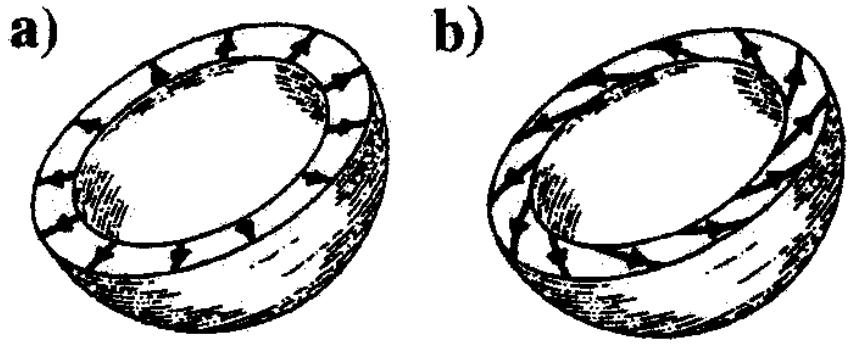

Figure 32. Two hypothetical, cup-shaped cardiac activation wavefronts that would have identical electrical fields, as determined by the shape of the rim of the cup, but differing magnetic fields, as determined by both the shape of the rim and the circulating currents within the wavefront. (Adapted from [170])

toward the lower left within the chest. The magnetic field recorded outside the chest is, to first order, that of this electric dipole, *i.e.*, it encircles the electric dipole. Hence the time variation of the magnitude and orientation of the electric dipole moment of the heart produces corresponding, but orthogonal, variations in the magnetic field [3,169].

Although the various waves of the ECG and MCG have differing orientations throughout the cardiac cycle, simple measurements of the two signals do not demonstrate any advantage for either technique in the detection of a variety of clinical disorders. It is, however, theoretically possible for the MCG to contain information not present in the ECG. The pair of depolarization wavefronts shown schematically in Fig. 32 are indistinguishable electrically, but would have different magnetic field distributions, associated with action currents which would have a component of current that flows around the heart as a result of the fiber structure of the heart [3,170]. While this early prediction simply stated that these circulating currents might arise as a result of the cardiac fiber architecture, it was subsequently shown that the electrical anisotropy of the cardiac tissue could result in the magnetic signals containing information about off-diagonal elements of the anisotropy tensor that are not present in the electric potentials [171]. The identification of such sources from the body-surface potential maps and magnetic maps will require a mathematical model that is sufficiently detailed that the error associated with the effects of the heterogeneities and anisotropies within the thorax will be smaller than the as-yet not detected contribution from swirling currents. Until this is accomplished, it will be

impossible to state whether or not the differences between the ECG and MCG that have been observed for some time [172,173] are the result of electrically silent sources or simply differences in the spatial sensitivity to the primary cardiac sources and the secondary thoracic ones [174].

Despite the first-order similarity of the ECG and the MCG, there are several promising areas of MCG research, particularly now that multichannel MCG SQUID systems are becoming more common. A detailed and excellent review of cardiomagnetism is presented in reference [175], and a briefer update in reference [176].

The MCG can also be used to localize noninvasively the site of origin of cardiac arrhythmias, such as those responsible for atrial or ventricular tachycardias, in advance of a catheter ablation procedure to remove the source of the abnormal activity. Currently, the invasive catheterization procedures used to localize an arrhythmogenic focus require several hours of concentrated effort by a large staff, are costly in both personnel and supplies, are not without risk to the patient, and can result in a significant X-ray exposure to the patient and particularly to the physicians. Possibly the MCG could mitigate some of these problems. However, advanced, multielectrode mapping catheters may prove more useful [177,178], since the ablation of the site of the tachycardia beat still requires invasive catheterization. Furthermore, some cardiac arrhythmias are normally silent, and can be provoked experimentally only during catheter stimulation and with the administration of drugs. Thus, the unanswered question is to what extent does the noninvasive MCG study simplify or shorten the catheterization procedure required for the ablation.

While many of the most exciting MCG studies are as yet only published in conference proceedings, there are a number of intriguing preliminary results that bear further examination, in particular in the estimation of risk for cardiac arrhythmias and the detection of ischemic heart disease. In addition to the summaries by Stroink [175,176], recent work is described in references [160,179–188]. There is one word of caution in interpreting the relative information content and diagnostic capabilities of the ECG and MCG: it is important that the multi-channel MCG be compared to the comparable body-surface potential map, with both measurements covering comparable thoracic areas and with the data being processed similarly. Once differences are documented, it will be important to obtain a clear understanding of the mechanism by which the MCG could convey more information than the ECG. Likely candidates for such mechanisms are the fiber architecture and anisotropy of cardiac tissue, and the reduced filtering effect of thoracic conductivity heterogeneities on the MCG relative to the ECG. As stated by Stroink [176], this will require careful measurements and mathematical modeling.

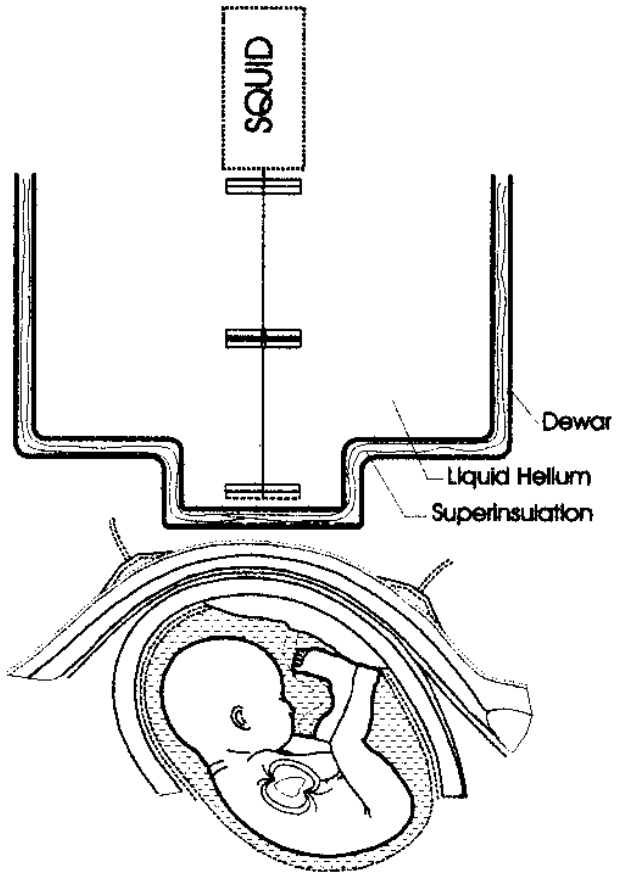

Figure 33. A schematic view of a SQUID gradiometer positioned above the fetal heart. (Adapted from [16])

SQUID magnetometers can also be used to record the fetal magnetocardiogram (FMCG), as has been studied in detail by Ron Wakai at the University of Wisconsin in Madison [155]. Figure 33 shows a SQUID placed over the fetal heart. Note the substantial distance between the SQUID and the heart. Figure 34 shows a vector FMCG recorded at Vanderbilt [189, 190]. In the upper FMCG trace, the X component shows both maternal and fetal signals. The orthogonal Y component shows very strong maternal signals interspersed by smaller fetal signals, whereas the Z component shows negligible maternal contamination and clear fetal signals. The net result is that it should be possible to build compact SQUID instruments for recording the fetal magnetocardiogram in the hospital, possibly with digital SQUIDs. Because of the small size of the fetal heart and its depth below the SQUID, it is unlikely that mapping of the FMCG over the abdomen will produce much more than a dipolar map, so that it may be sufficient to use a vector SQUID magnetometer such as the one used to obtain Fig. 34 to record three orthogonal FMCG components [169,189,190], which could then be used to correct at least in part for the effects of the variable and often unknown

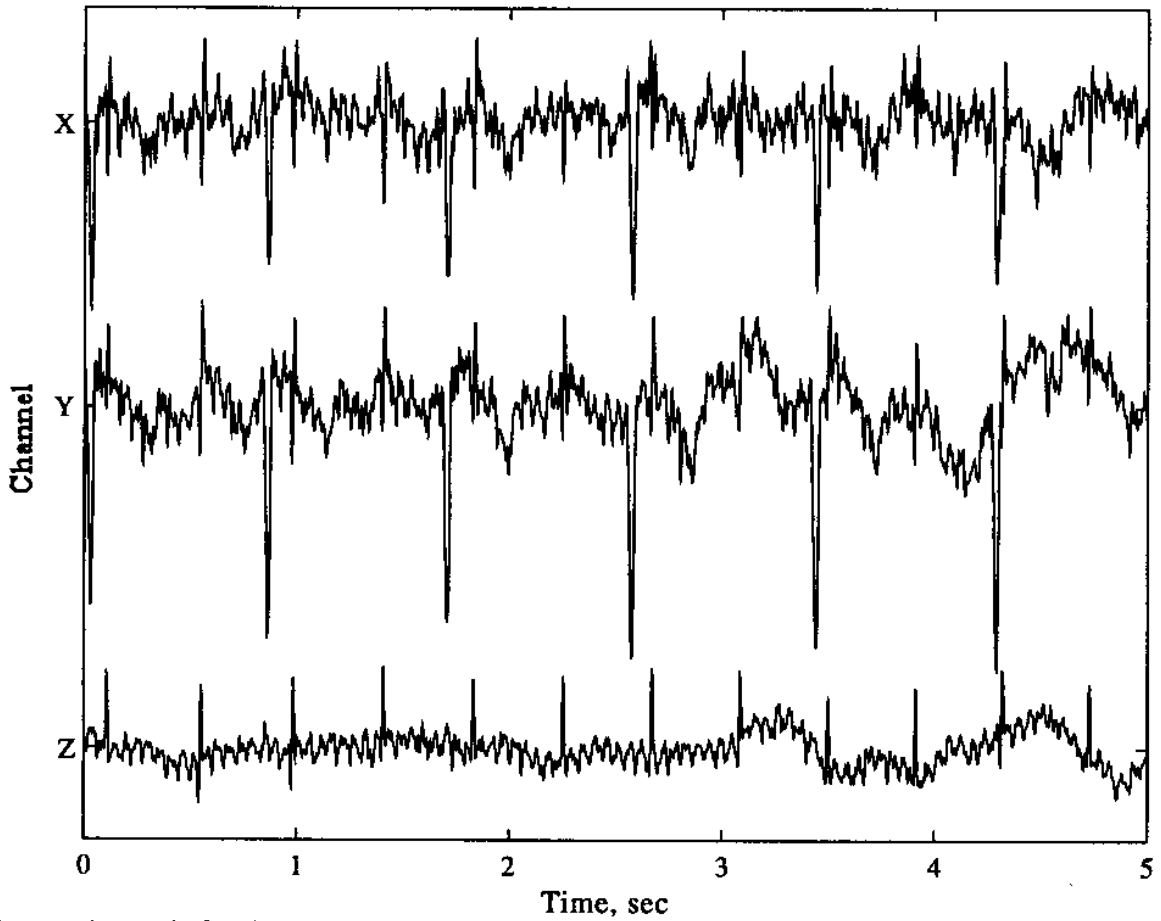

Figure 34. A fetal vector magnetocardiogram. Raw data filtered with a passband of 0.3 to 80 Hz. The three orthogonal gradiometers have a 15-cm baseline. The maternal signal dominates in channels X and Y, while the fetal signal is predominant in channel Z. (Courtesy of William Drake)

fetal orientation, and could provide excellent separation of maternal and fetal signals, and clear identification of fetal P, QRS, and T-waves [190]. The challenge will be to develop sufficiently-sensitive SQUIDs and suitable noise-rejection algorithms so that signal-to-noise ratios are high enough that the entire P-QRS-T complex can be clearly resolved without signal averaging, which could then make the fetal MCG an invaluable tool for the diagnosis of fetal cardiac arrhythmias and overall fetal cardiovascular stress. The even greater challenge for SQUID magnetometry is recording the fetal magnetoencephalogram (FMEG). It has already been shown that a SQUID can record, with signal averaging, the fetal auditory evoked response [191]. Advanced multichannel SQUID arrays and adaptive signal processing should provide much-improved signal-to-noise ratios, and may eventually allow recording of the spontaneous fetal MEG.

Another application of SQUIDs to cardiac studies is the use of a high resolution SQUID to map the spread of current through thin slices of cardiac tissue, which will provide information about the electrical properties

of the three-dimensional, anisotropic cable-like behavior of the heart [192].

Gastroenterology. The magnetoenterogram (MENG) and the magnetogastrogram (MGG) are new applications of SQUIDs that are being pursued by William Richards, Alan Bradshaw and other members of our group at Vanderbilt. The electrogastrogram, the electrical signal from electrical activity in the stomach, was first recorded in the 1930's. David Cohen first detected the magnetogastrogram, the magnetic equivalent, twenty years ago. While it is relatively easy to use electrodes on the surface of the abdomen to record electrical signals from the stomach, the multiple layers of fat and muscle between the small intestine and the abdominal surface make it virtually impossible to record noninvasively the electrical activity of the small intestine. As with the brain, these intervening layers serve as a harsh, spatial low-pass filter that smears and attenuates the electric signals, but this tissue has little effect on the magnetic fields. Hence, we have been able to use SQUIDs to record the magnetoenterogram, which does not have an equivalent electrical recording. Figure 35 shows typical magnetogastrogram and magnetoenterogram data [193].

Our signals, recorded for the first time in humans in 1992 [194,195], may be of potentially great clinical significance in diagnosing electrical disorders of the stomach and intestine, such as arrhythmias, angina, ischemia, and infarct: Death often occurs within two days of an intestinal infarct, and the SQUID may provide an early, noninvasive diagnosis. These studies are described in a number of recent publications [161,196–198]. The vector MENG and vector MGG offer additional advantages, in that the vector nature of the field from electrical activity in differing regions of the abdomen can be utilized to separate the different contributions to the signals and even characterize propagation of activity in the stomach [199].

While the magnetogastrogram and the magnetoenterogram are measures of the electrical activity of the gastrointestinal system, SQUIDs can also be used to track the associated mechanical activity through the motion of magnetic tracers or marked capsules with temporal and spatial resolutions of milliseconds and millimeters [200].

Liver Iron Susceptometry. SQUIDs have been shown to be useful for the assessment of elevated liver iron stores in patients with iron overload. Fischer [22] reviews the subject in detail. Recent work suggests that these measurements can be made with permanent magnets and an HTS gradiometer and SQUID [201].

5.1.3. *Laboratory and Other In Vitro Applications*

In contrast to humans, SQUID measurements on laboratory animals and isolated tissue preparations require much higher spatial resolution, and hence smaller pickup coils and closer coil-to-sample spacing than can be

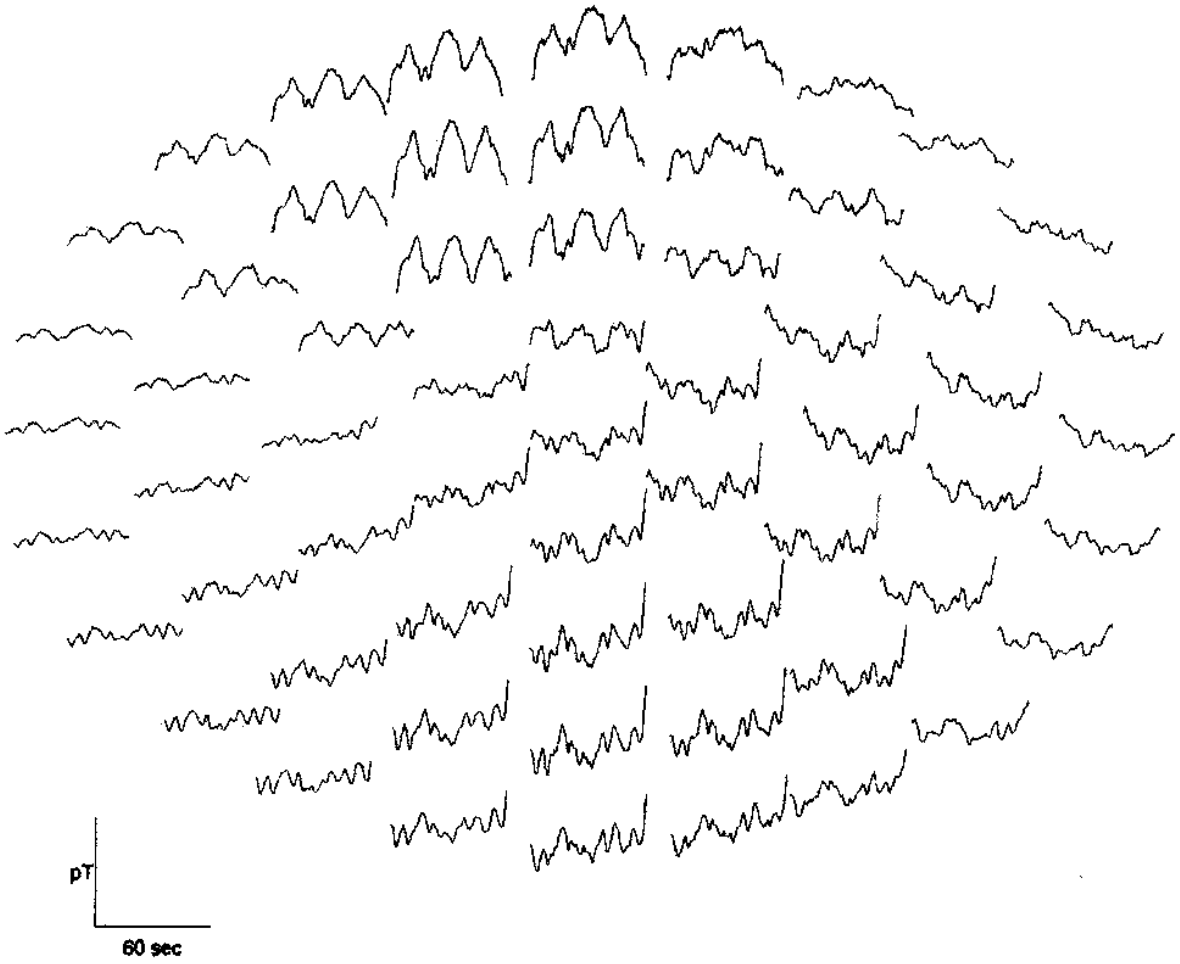

Figure 35. Magnetic recordings of the basic electrical activity of the human gastrointestinal tract obtained with a 61-channel BTi SQUID system [193]. The upper traces show the 3 cycle-per-minute signals from the stomach, termed the magnetogastrogram (MGG), while the lower traces show the 10- to 13-cycle-per-minute signals from the small intestine, the magnetoenterogram (MENG). (Courtesy of Alan Bradshaw)

provided with a conventional biomedical SQUID. For example, early measurements of the variety of magnetic signals during epileptic seizures in rats were made with a SQUID whose pickup coil was larger than the brain of the rat [202]. I have reviewed elsewhere our high-resolution biomagnetic measurements [10], which are summarized in Fig. 36. Figure 37 shows the magnetic field that was evoked upon electrical stimulation of a thin slice of rat hippocampus in a dish placed beneath a MicroSQUID magnetometer [203]. These data demonstrate that biomagnetic recordings on the scale of millimeters require low-noise SQUIDs, particularly since the measurements must be made with a kHz bandwidth.

Magnetopneumography, the measurement of the relaxation rates of the magnetic contamination in the human lung, utilizes a transient magnetic field to magnetize microscopic ferri/ferromagnetic particles, so that a mag-

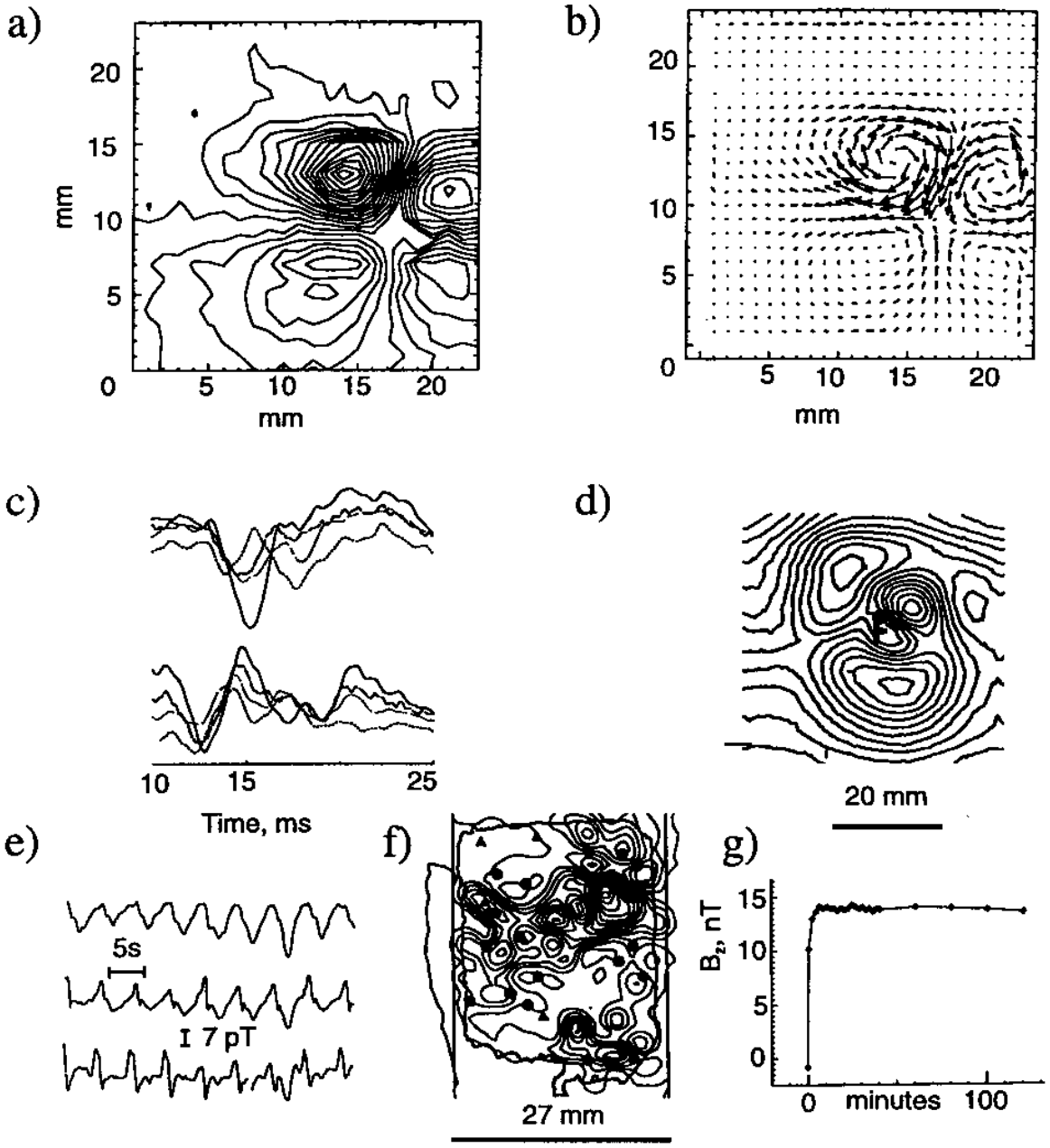

Figure 36. Representative data from the high resolution MicroSQUID magnetometer at Vanderbilt. a) Magnetic field (25 pT contours) and b) current densities recorded 6 ms after the stimulus in a slice of canine cardiac tissue [192]. c) Simultaneous four-channel recordings of two different single motor units in the human thumb [204]. d) Magnetic field from a 94-hr chick embryo [205]. The embryo is the hook-shaped line. e) Simultaneous, three-channel recording of the magnetic field from the basic electrical rhythm of isolated prairie dog small intestine [195]. f) The induced magnetization distribution from a 50-μm thick slice of pyroclastic rock in a 285-μT applied field with the locations of the magnetic (circles) and biotite (triangles) inclusions [33] (2 mA/m contour spacing). g) The time-course of the uptake of a 900-$\mu\ell$ sample of superparamagnetic microspheres by a rat liver [206] in a 171-μT applied field. The applied field in (f) and (g) was provided by Helmholtz coils outside the cryostat. (From [16], with permission)

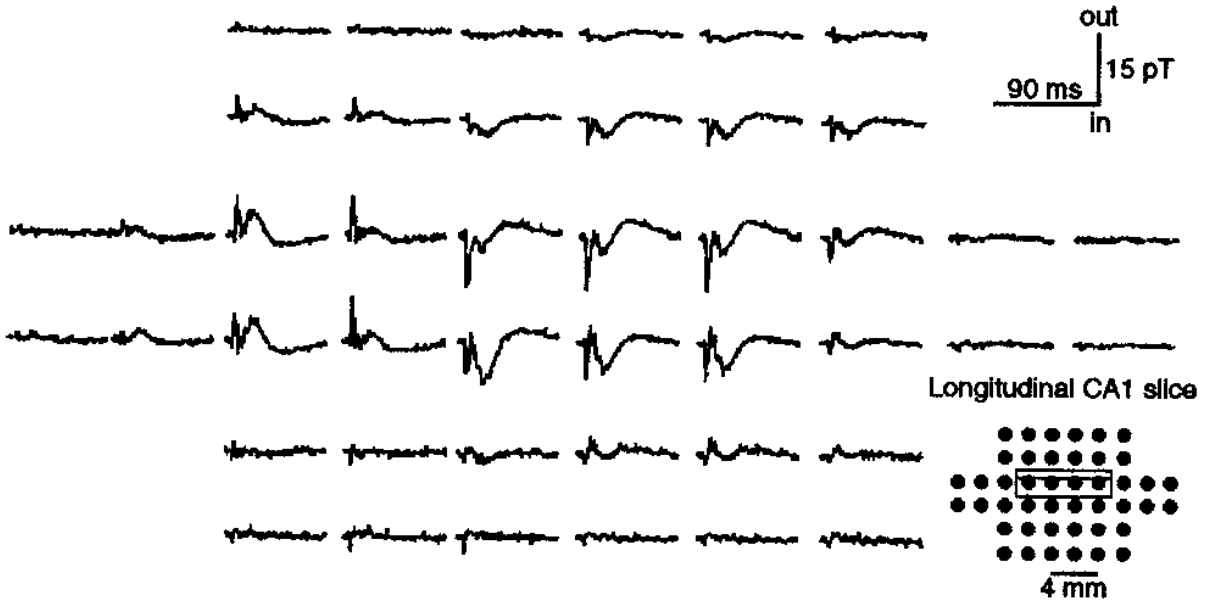

Figure 37. The spatial variation of the magnetic field that was evoked by stimulation of a slice of rat hippocampus. Each tracing lasts for approximately 90 ms. The recording locations are separated by 2 mm. The peak-to-peak amplitude of the largest signal is 15 pT, recorded in a 1-kHz bandwidth. (Adapted from [203], with permission)

netometer can measure the relaxation of this magnetization with time [23]. This concept has been extended to a promising laboratory immunoassay that utilizes the difference in the relaxation rates of magnetic nanoparticles that are free to rotate in a carrier liquid and those that are physically bound by an immunological reaction to a fixed substrate [25,26]. SQUIDs are critical to this approach, in that the sensitivity of the SQUID is required to detect small number of nanoparticles, and hence provide the most sensitive possible immunoassay. The primary advantage of this technique over fluorescent or radiological immunoassays is the fact that the binding is measured directly through the response of the particle following removal of the magnetic field, and it is not necessary to wash out the unbound fluorescent or radiological tracer.

5.2. APPLICATIONS: NDE

The greatest challenge for SQUID NDE is that there are a large number of conventional eddy current techniques that are inexpensive, technically-simple, easy-to-use, and widely accepted. Because of their cost, complexity, and unfamiliarity, SQUIDs will be considered for only those applications where existing techniques are inadequate. As a result, many potential applications for SQUIDs present a number of significant technical, economic, and even political difficulties, independent of those that are presented by the

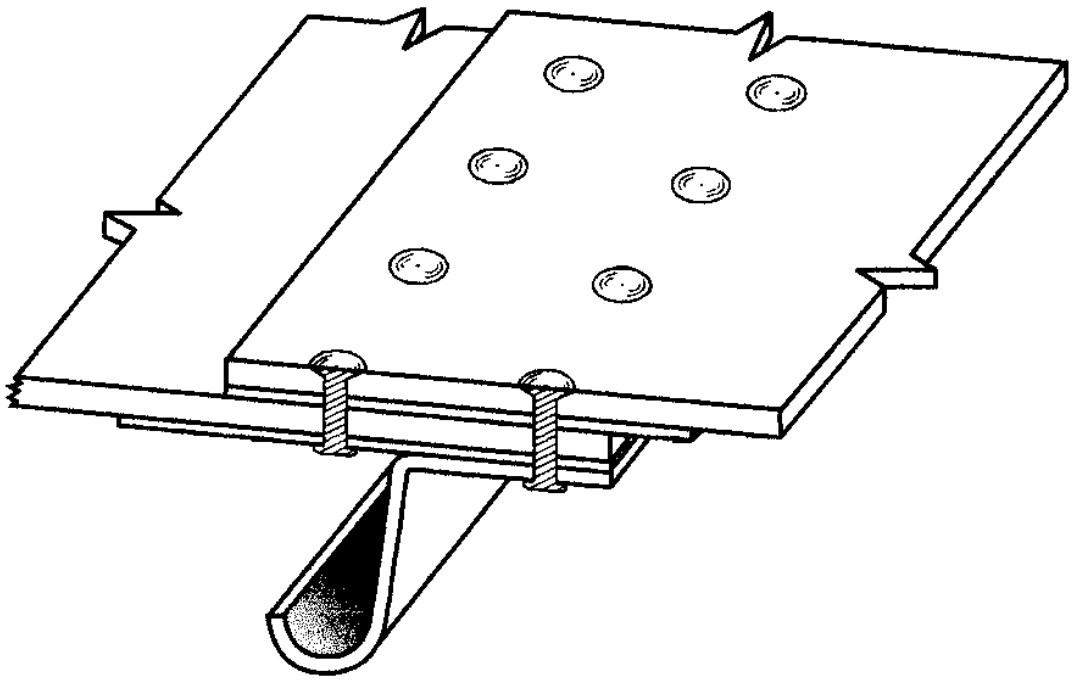

Figure 38. A schematic representation of an aircraft lap joint that would be well suited for SQUID NDE and not suitable for ultrasonic or eddy-current tests.

SQUIDs themselves. Many of the most promising applications appropriate for SQUID NDE at this time may well be those that involve systems where the economic or personal risk of an undetected failure is great, or where the value of the individual item being tested is high. Consistent with this, there are several applications of SQUIDs to NDE that have been examined in great detail: aging aircraft, including the detection of cracks and corrosion damage in aircraft aluminum, such as lap joints and wheels, and the detection of hidden corrosion in aircraft lap joints; the detection of cracks and altered stress states in ferromagnetic materials, including steel plates in nuclear reactors and reinforcing rods in concrete; the detection of fault currents in integrated circuits and multichip modules; and the detection of flaws in wires prior to their being drawn to a finer gauge.

5.2.1. *Aircraft NDE*

In contrast to other major industrial systems, airplanes are to a large extent nonmagnetic, being fabricated primarily out of aluminum alloys. In addition, aircraft fleets in the United States and elsewhere are aging, and aging aircraft are prone to fatigue and stress-corrosion cracking [207, 208]. Some of these flaws are difficult to detect with conventional eddy current, ultrasound, or x-ray techniques. In the typical aircraft lap joint shown in Fig. 38, there are three to five layers of metal. If there is no sealant or bonding between the layers, one cannot use ultrasound to find second- and

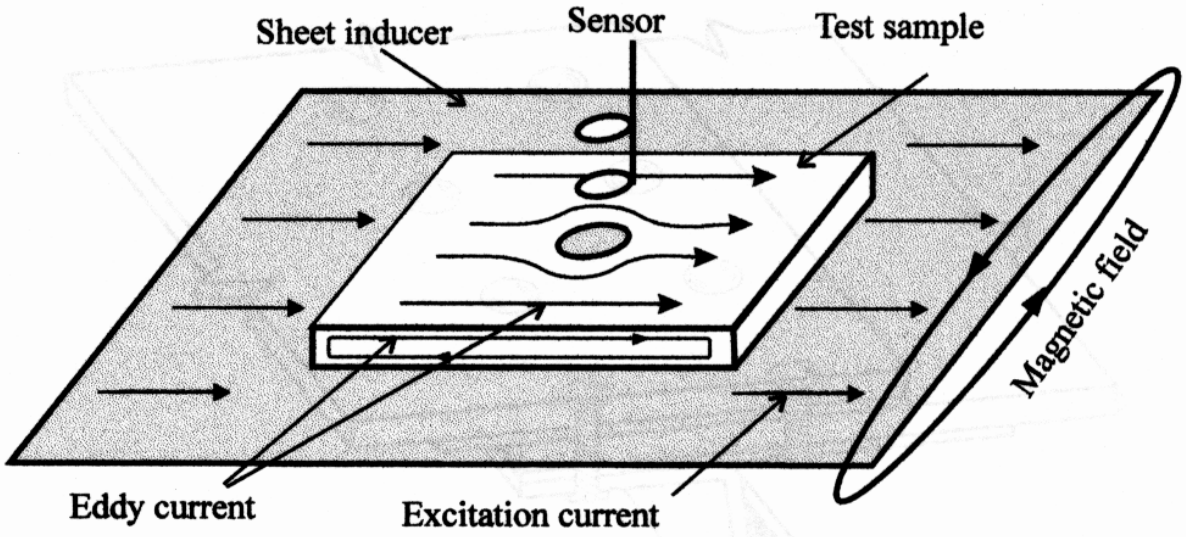

Figure 39. A schematic representation of a current-carrying sheet used to induce planar eddy currents in a metallic sample. In practice, the sheet inducer would normally be attached to the SQUID, so that the SQUID and inducer could be scanned relative to the sample. (Adapted from [210])

third-layer corrosion or cracks. The metal can be sufficiently thick such that, because of the skin depth of eddy currents, conventional eddy-current techniques cannot find the deep flaws and the deep cracks. To give some idea of the nature of the problem, 7075-T6 is a typical aircraft aluminum. Eddy-current detection of a flaw that is 1 cm into a wing structure would require that the eddy-current instrument operate at frequencies as low as 100 Hz, where it is very difficult to obtain adequate sensitivity with conventional eddy-current instruments. SQUIDs work well at 100 Hz, or 10 Hz, or even dc [38,39], and hence are well suited for very low frequency eddy-current measurements. The preliminary data obtained so far suggests that SQUID NDE may live up to its promise of great sensitivity with high spatial resolution [40,41,43,45,82,143].

A SQUID technique that has undergone extensive development at Vanderbilt for aircraft NDE is the use of a sheet conductor carrying an alternating current to induce planar eddy currents in the test sample [209], shown in Figure 39. The advantage of this technique over other inducer geometries is that the uniformity of the induced currents simplifies interpretation of the resulting magnetic images and thereby should provide a more direct, quantitative means for identifying cracks and determining their size. Furthermore, the use of phase-sensitive detection and analysis techniques allows the SQUID to be used for depth-selective detection that can distinguish the signature of a subsurface crack from the larger signal from an adjacent rivet [45, 210, 209].

One of the major problems in crack detection arises from the often unknown orientation of the crack. Application of currents from two orthogonal directions allows oriented, depth-selective eddy-current imaging. Figure 40 shows data recorded at Vanderbilt from a section of simulated aircraft wing that has cracks in both layers, neither layer, lower layer, upper layer; we found very clear signatures that were related to the depth and size of the crack [45]. In Fig. 40, the test sample is made of two layers of 7075-T6 aluminum panels bolted together by four 6-mm-diameter aluminum flat-head pins and nuts. Each panel is 25 × 25 mm^2 and 3-mm thick. The crack defects beneath the surface are simulated by 6-mm-long EDM slots beneath the fasteners. Adjacent to fastener #2 are 6-mm slots in both the top and bottom layers. Fastener #1 has a slot in the bottom layer and fastener #3 has a slot in the top layer. Fastener #4 is without slots and is used to determine the signature of the hole and fastener alone. The induced eddy current is disturbed by both the pins and slots. The lower portion of Fig. 40 shows surface plots of the magnetic field obtained at various phase angles and for induced currents parallel and perpendicular to the slots. The field has been squared for better visualization.

At a phase angle of 0^o with the current perpendicular to the slots (left column), the signal is largest from fastener #2 (with slots in both layers), and smallest for pin #4 (without slots). With the current parallel to the slots, the signals from all four fasteners are equivalent, in that none of the cracks contribute to the magnetic image. At a phase angle of 85^o, the signature of the fasteners changes from dipolar to quadrupolar, as a result of the reversal of the direction of the induced currents at a particular phase angle and depth within the sample. At that phase angle, each signal has four peaks: the sharper peaks reflect the contribution of the current densities near the surface, while the broader peaks reflect the contribution of the current densities below the surface, as predicted by theory [211, 212]. At the phase angle of 95^o, the signal for fastener #1, with the second-layer crack, is larger than that of cracks #3 or #4, thereby demonstrating the ability of the depth-selective technique to distinguish between cracks in the upper (#3) and lower (#2) layers.

One issue in SQUID NDE that has yet to be examined in detail is feature extraction. The challenge is to devise automated techniques that can identify and quantify a flaw, rather than rely solely on the ability of a inspector to recognize a particular signature as that of a flaw. Neural nets are one approach that has been examined for the identification of cracks in steel [213]. Another is to use the rotational assymetry of a crack adjacent to a rivet in an airplane wing or fuselage to separate the signature of the crack from the larger signature of the hole. Figure 41 demonstrates that the peak-to-peak signature depends upon the angle that the current makes with

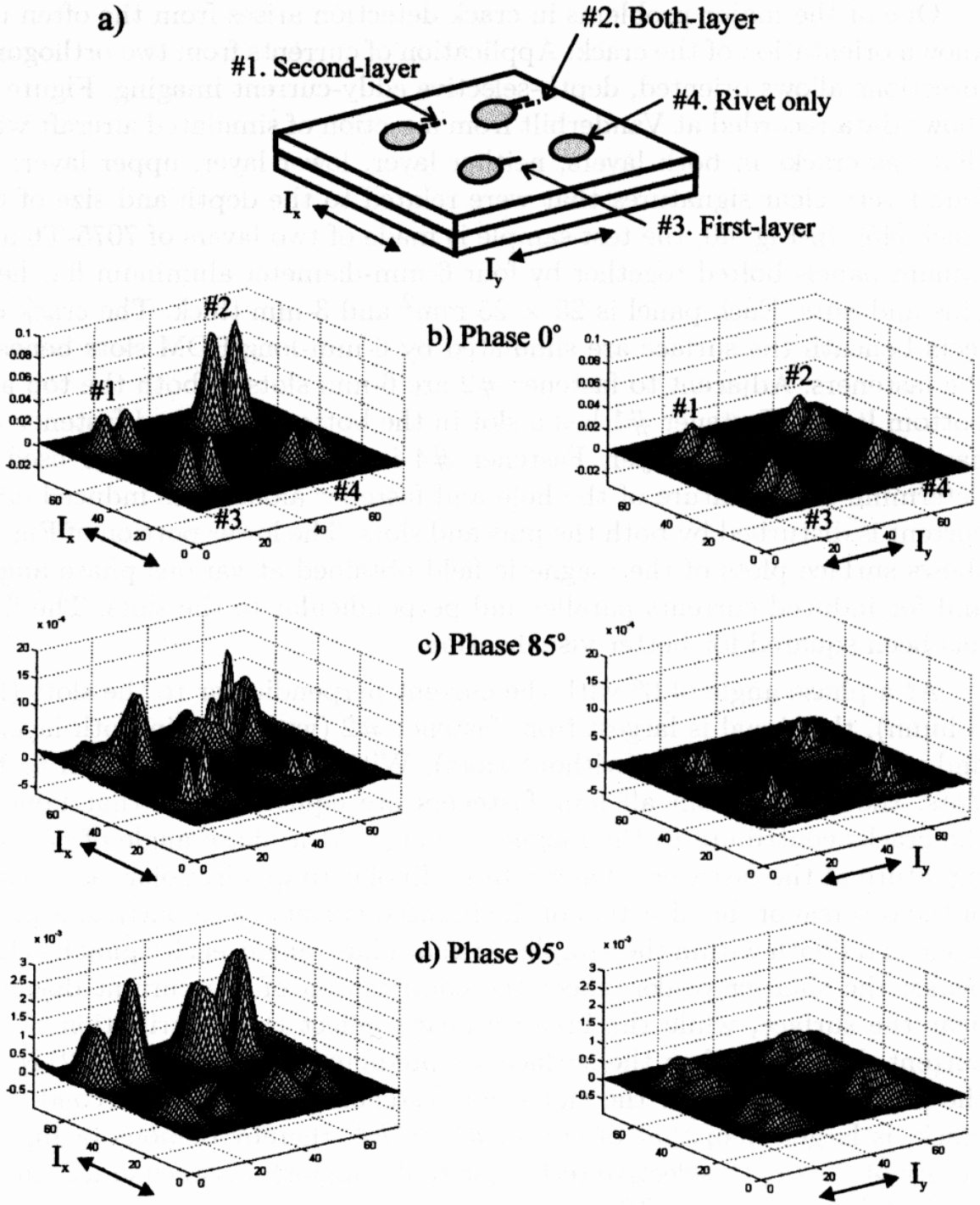

Figure 40. SQUID images of the cracks beneath rivets obtained at Vanderbilt with the MicroSQUID magnetometer and a sheet inducer. Top: the experimental setup (not to scale). Fastener #2 has a crack in both layers, while #1 has one in the second (lower) layer, and #3 in the first (upper) layer only. Fastener #4 has no cracks. Bottom, left column: The magnetic images for current induced perpendicular to the cracks for three different phase angles of the magnetic field relative to the current in the inducer. Bottom, right column: current parallel to the cracks. See text for additional details. (Adapted from [45])

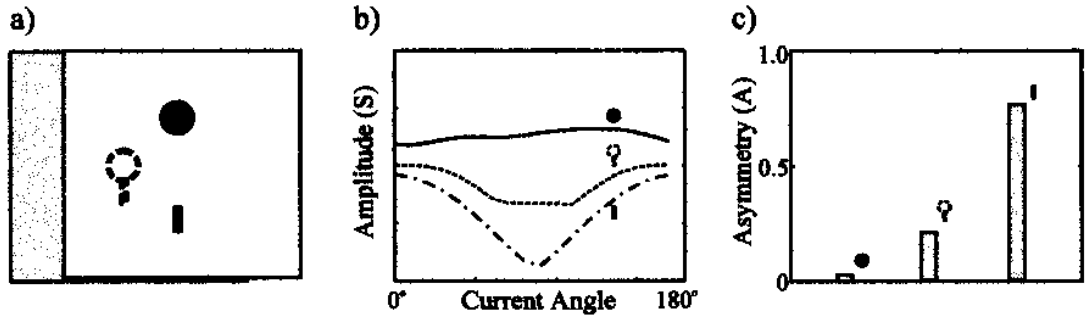

Figure 41. An example of the use of oriented imaging to distinguish between a circular hole, a hole with a slot, and a slot alone. Left: The test sample. Middle: The maximum amplitude recorded from each feature of a magnetic map as a function of the orientation of the applied current. Right: The ratio of the maximum to minimum amplitude from the middle figure. There is clear discrimination between the three types of flaws. (Adapted from [210])

respect to a crack. This can be used to provide a self-referencing technique to correct for varying (and unknown) liftoff between the SQUID and the sample [210].

As shown in Fig. 42, an application of SQUIDs that has already been demonstrated in an aircraft maintenance facility is the detection of cracks in aircraft wheels, which are subject to enormous stress and heat during takeoff and landing [67]. In this measurement, the data demonstrate that the SQUID sensor is superior to other conventional NDE techniques.

5.3. NDE ON STEEL

Although the sensitivity of SQUIDs is generally not required for measuring magnetic fields outside of ferromagnetic samples, there have been several interesting studies using SQUIDs for NDE on steel. Harold Weinstock has measured the response of ferromagnetic materials to stress [2,46], and has shown that a SQUID can remotely detect changes in the flux expelled from the sample as it is stretched multiple times, as indicated in Fig. 43. This may have applications to the nondestructive testing of steel structures.

The Strathclyde group has done a great deal of work on steel plates [91,117,215] and has shown that they can detect flaws induced in a steel plate both thermally and in the manufacturing process, as shown in Fig. 44. They can find hidden, simulated fatigue cracks in a ship hull plate, shown in Fig. 45. In this measurement, a fatigue crack was artificially induced in a standard issue UK Admiralty steel hull plate. The crack grew from the underside in the view shown in (a), with the tip finally visible over a 137-mm length near its center. Note that the crack was uneven; it developed most near the ends of the loading bar where the stresses were highest, and

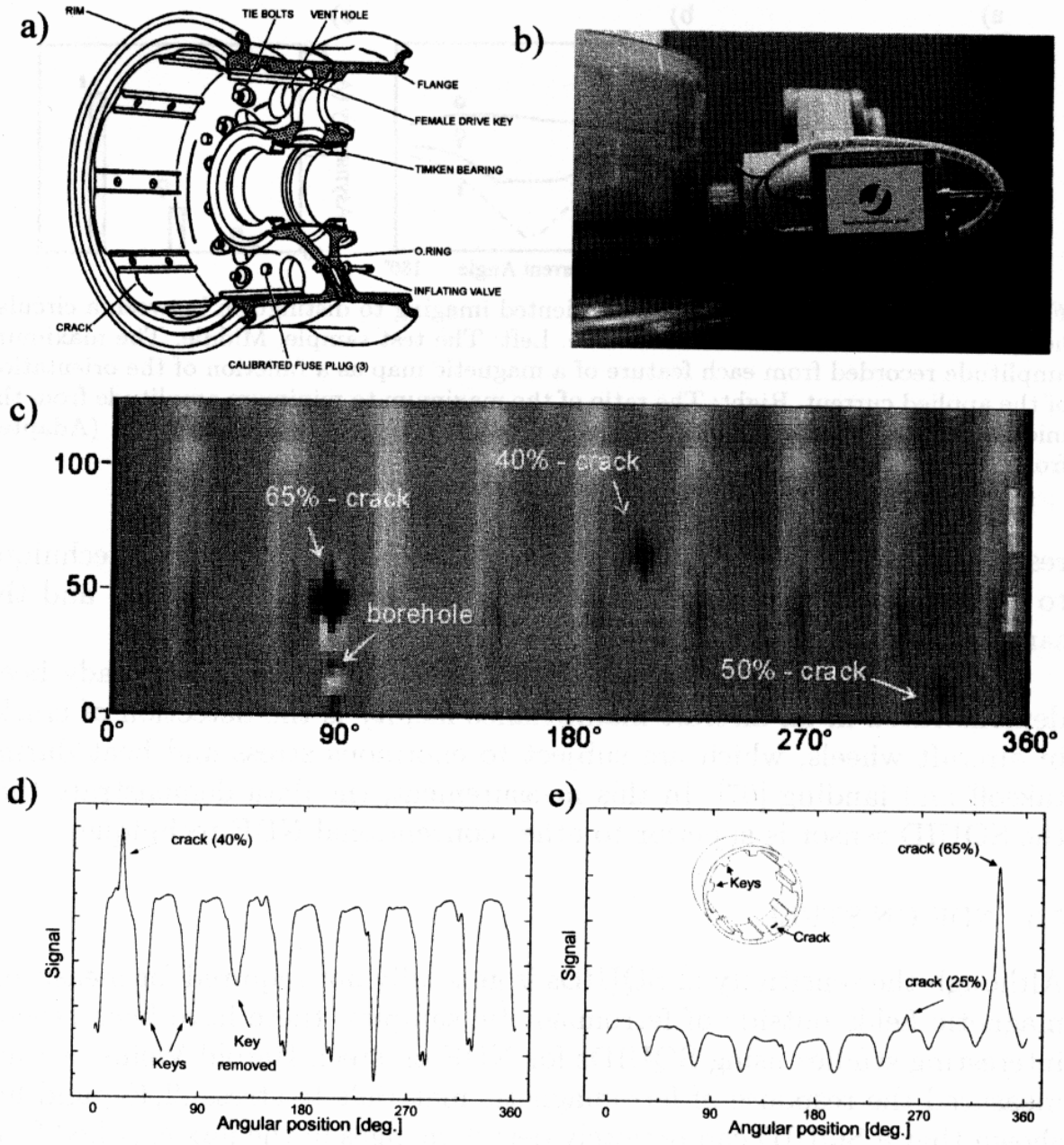

Figure 42. SQUIDs for detecting cracks in airplane wheels. a) Sketch of an Airbus aircraft wheel, with typical crack positions. b) Automated aircraft wheel testing unit, the SQUID mounted on a robot. c) Map of the in-phase SQUID response of the outer wheel surface (x-axis: angle around the circumference of the wheel; y-axis: axial height in mm). The nine vertical stripes are the magnetic signal from the ferromagnetic keys for attaching the brake drum, and signals between them are from artificial flaws. d) and e) Two in-phase signal tracks recorded at different axial heights in one rotation of the wheel. The signals from artificial flaws and a removed key are evident. (Adapted from [67], with permission)

toward higher lateral distances because of the alignment of the three-point loading machine. The eddy-current map of the cracked plate in (b) was made with an induction-coil current of 5.25 mA peak-to-peak at 175 Hz

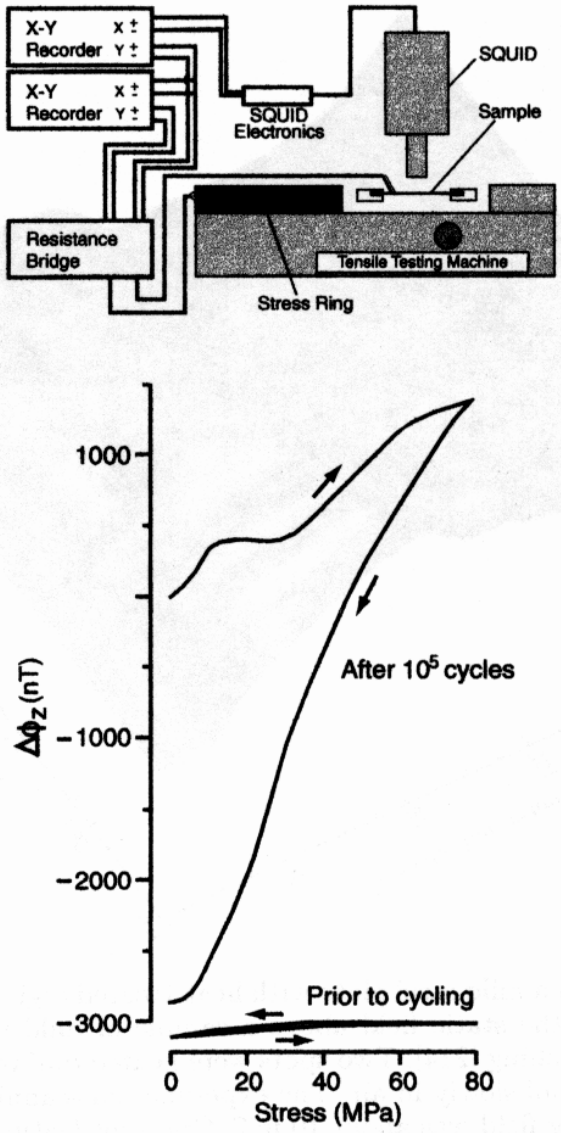

Figure 43. The test setup (upper) and typical data (lower) from SQUID measurements on the effects of cyclic stress on the magnetic field outside of a steel sample. (From [46], with permission)

(skin depth about 0.5 mm), giving a field of about 6 μT at the surface of the plate. The stand-off distance was 3.6 mm. A lock-in amplifier was used for demodulation of the SQUID signal. In (c), the static field map of the cracked plate was obtained with a polarizing field of 20 mT and a stand-off of 4.1 mm. For current injection into the plate, the inversion in (d) of the magnetic map of current flow around the artificially induced crack was for a 190-Hz, 1.73-A peak-to-peak current injected diagonally across the plate between the points shown in (a); a lock-in amplifier was used for demodulation. From these data, we see that it may be possible to use SQUIDs to look deep into steel plates and find cracks that would not be readily detectable otherwise. A group at Hitachi has also used SQUIDs to

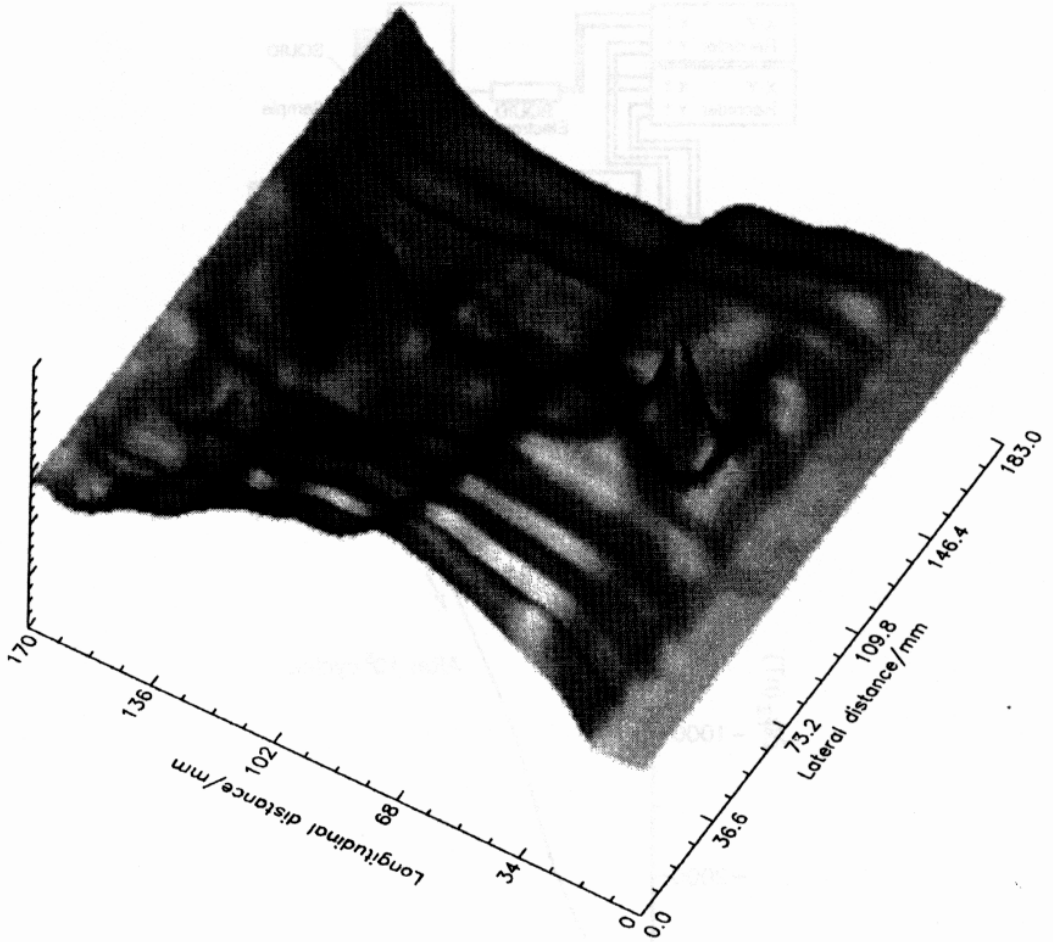

Figure 44. Field map of a mild steel plate with heat-treated regions and a manufacturing flaw. A surface plot of the static field above a sample of mild steel as rolled from the mill, without surface finishing [214]. Two spots were heated dull red with an oxyacetylene torch, then allowed to cool slowly in air. The experimental scanning stand-off was about 5 mm, and the polarizing field was about 10 mT. One spot feature is larger in amplitude than the other because that spot was heated slightly more. Also visible is a linear feature along the plate which was caused by an inconsistency in manufacturing, visible on the plate surface as a series of faint bubble-like marks along the direction the plate was rolled. (Courtesy of Sandy Cochran and Luke Morgan of the University of Strathclyde)

study ferromagnetic materials [216].

There is a need to detect noninvasively the condition of reinforcing steel in airport runways, bridges and buildings. For example, currently the accepted way to determine the integrity of the steel reinforcing rod in an aircraft runway is to core it. A similar problem exists with the detection of failures of the steel cables that are used to prestress highway bridge beams. The Jülich group has demonstrated a multichannel SQUID and flux-gate system that uses a yoke magnet to apply a magnetic field to the cable, and five magnetometers that measure the stray field produced by a fracture in the cable [217]. Figure 46 shows the principle, implementation and results obtained with the system. Obviously, there are relative advantages and

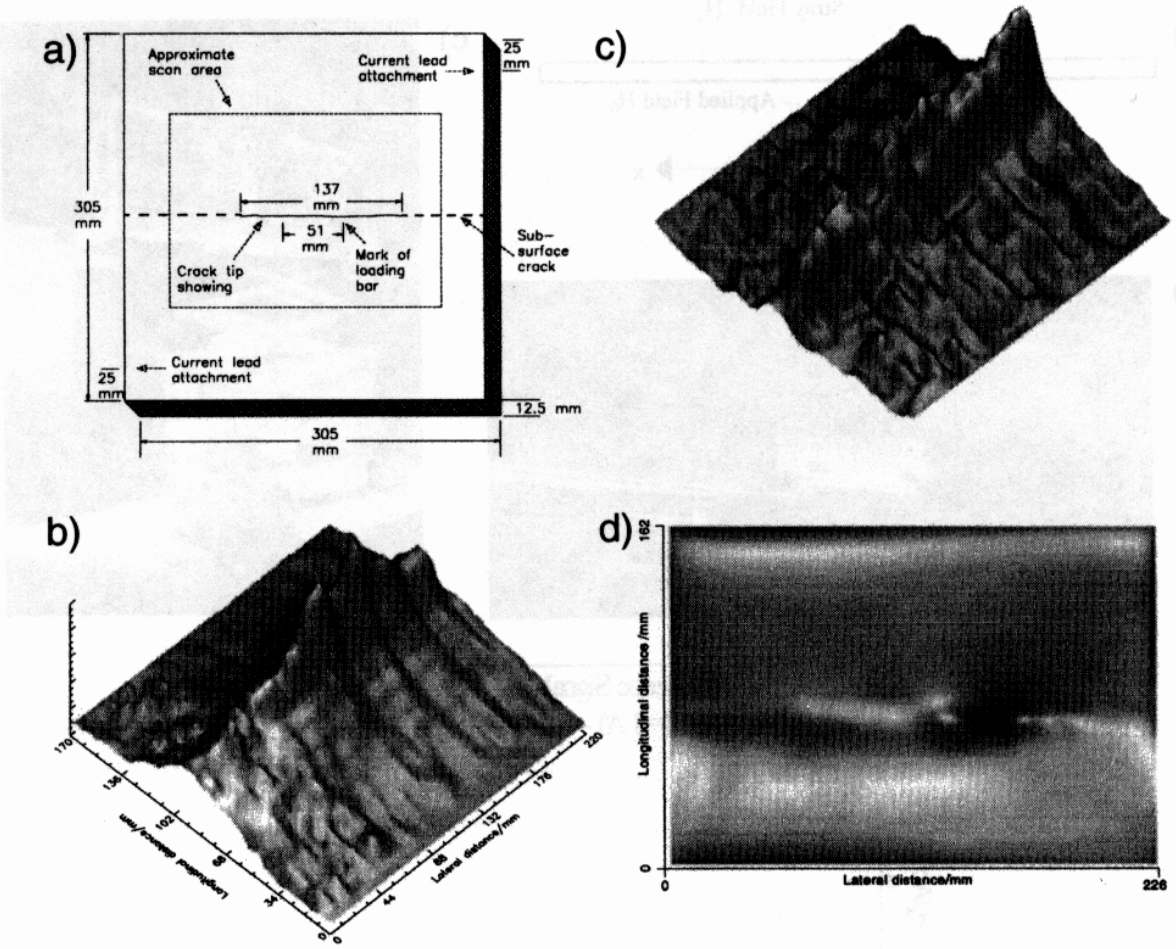

Figure 45. SQUID measurements on an artificially-cracked steel hull plate [215]. a) A fatigue crack was artificially induced in a standard issue UK Admiralty steel hull plate. b) Eddy-current map of the cracked plate. c) Static field map of the cracked plate in a 20-mT polarizing field. d) Inversion of the magnetic map of current flow around the crack. A 190-Hz, 1.73-A peak-to-peak current was injected diagonally across the plate between the points shown in (a). (Courtesy of Sandy Cochran and Luke Morgan of the University of Strathclyde)

disadvantages with both flux gates and SQUIDs, in terms of sensitivity, stability, cost, and ease of use, that would determine whether SQUIDs or flux gates would be used in practice.

There are other possible applications of SQUIDs for the NDE of steel. Detecting corrosion underneath the lagging in pipes is quite a challenge, particularly when the insulation, termed lagging, is asbestos. There is concern about finding long-term degradation of material in nuclear and conventional power plants.

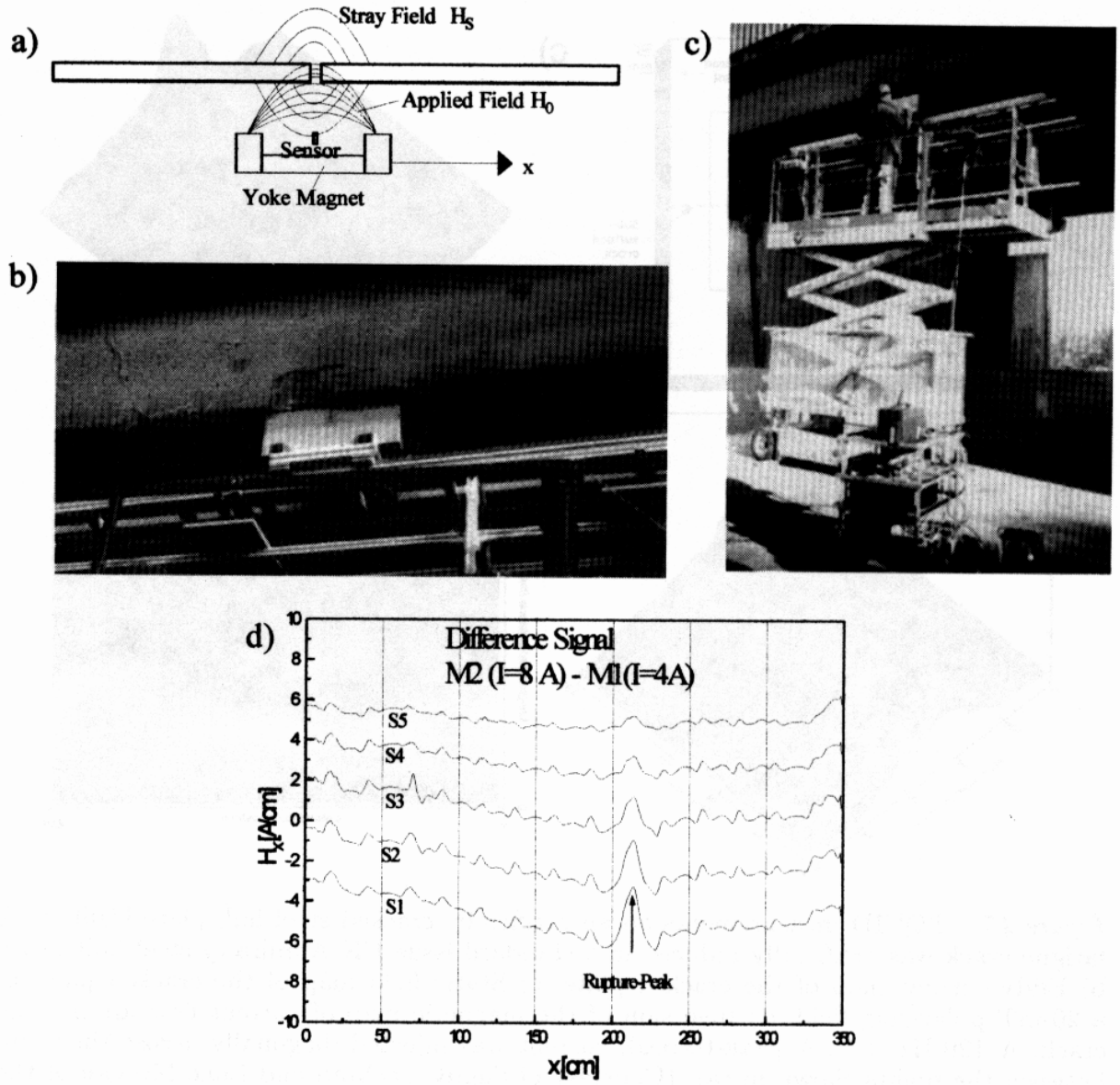

Figure 46. The magnetic measurement of leakage flux from broken steel cables in prestressed concrete. a) The principle of the measurement. b-c) Photographs of the SQUID/flux gate system in use. d) Signals from five magnetometers as they are scanned along two cables, one of which is ruptured, in a highway bridge. (Adapted from [217], with permission)

5.4. NDE ON DIAMAGNETIC AND PARAMAGNETIC MATERIALS

Because SQUID magnetometers can achieve their full sensitivity in the presence of strong applied magnetic fields, they are well suited for imaging of plastics and other materials that are generally considered nonmagnetic, but in fact have a measurable diamagnetic susceptibility. Two- and three-dimensional magnetic susceptibility imaging offers potential advantages for imaging composites with dilute magnetic tracers, and for magnetic imag-

ing of materials such as plastic, titanium or aluminum. One example of this approach involved the mapping of the remanent magnetization and magnetic susceptibility of a 50-μm slice of volcanic rock to allow identification of which component of the matrix is responsible for various aspects of the magnetic properties of the bulk composite [33].

In an application that clearly requires the sensitivity of the SQUID, we have used our MicroSQUID magnetometer to image plexiglass [47], which is a diamagnetic material, as shown in Fig. 47. We found that it is also possible to image water, titanium and non-metallic composites magnetically [28]. As demonstrated in Fig. 47, it is possible to detect minute amounts of paramagnetic tracer trapped in flaws on a surface of test blocks [36], allowing the detection of flaws with volumes as small as 2×10^{-12} m^3.

5.5. CORROSION STUDIES

In terms of basic studies on corrosion, SQUIDs are ideal because you can map dc or ac currents without having to contact the sample. Relative to the sensitivity of a SQUID, it takes substantial electric current to dissolve an airplane - approximately 300 coulombs of charge are required to corrode away a 0.1-mm-thick layer of aluminum from a 1-cm^2 sample, which would correspond to a current of 160 nA flowing for 80 years. SQUIDs can easily detect nanoamps! Despite the potential of SQUIDs for research into the prevention of corrosion of aircraft aluminum, there have been only limited published studies regarding the application of SQUIDs to corrosion research. Several years ago, a group at MIT demonstrated that SQUIDs could be used to measure corrosion noise in a zinc sample immersed in concentrated hydrochloric acid [218–221], but these studies effectively utilized the SQUID as a low-impedance, low-noise ammeter incorporated into a conventional electrochemical measurement system, and did not explore the ability of SQUIDs to make measurements that would otherwise be impossible with conventional techniques.

A 5-channel high-resolution scanning system was then constructed by Quantum Dynamics to examine corrosion in simulated lap joints. Hibbs *et al.* used this system to show that SQUIDs can detect filiform corrosion underneath the paint covering aircraft aluminum and can map the corrosion in a simulated lap joint exposed to concentrated sodium hydroxide [222,223,119]. They pointed out that the observed magnetic fields were significantly smaller than would be expected from Faradaic considerations alone. Recently, a German group has shown that an HTS SQUID can be used to detect corrosion in aluminum aircraft components [224], but it is unclear whether HTS SQUIDs will have sufficient sensitivity at the very low frequencies required to map corrosion activity.

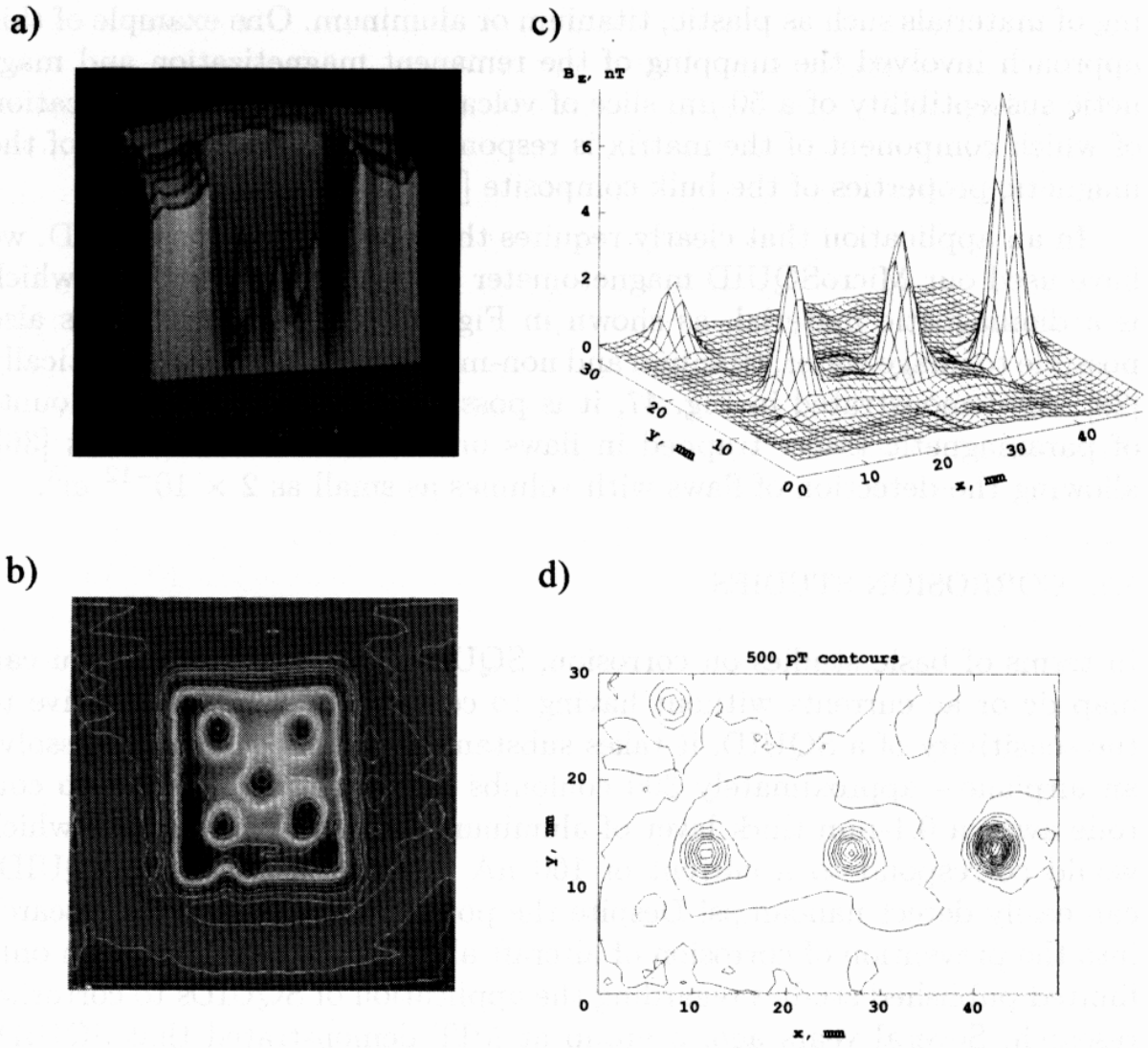

Figure 47. Magnetic susceptibility images. (a-b) A 25.4-mm square sample of plexiglass containing five 1.8-mm diameter holes was magnetized in a 110-μT applied field and scanned at a distance of 2.0 mm. The images show the distribution of diamagnetic material. (Adapted from [47]) (c-d) A nickel NDE sample containing EDM slots with dimensions of about 100 μm was surface decorated with paramagnetic microspheres. The magnetic field was mapped 2.0 mm from the sample with a 174-μT applied field. The images display the location and size of surface defects, including one (upper left) that was the result of a previously undetected scratch. (Adapted from [36])

Our group at Vanderbilt has conducted a number of studies that are defining the capabilities of SQUIDs for quantitative measurements of corrosion [42,225–228]. We have shown that a SQUID can image the temporal

and spatial variation of corrosion in aircraft aluminum, distinguish between the time course of corrosion in 2024 and 7075 aluminum, detect crevice and stress-corrosion cracking, detect corrosion of aluminum in salt solutions as dilute as one part per million NaCl, and map the distribution of corrosion activity from the opposite side of aluminum samples as thick as one centimeter. Figure 48 shows examples of one of these measurements.

More recently, we have used the SQUID system shown in Fig. 20 to image hidden corrosion in a simulated splice joint in aircraft aluminum[122], with typical data shown in Fig. 49. Expanding upon this type of measurement, our group is conducting a pair of studies of corrosion in aircraft aluminum. The first is designed to determine the quantitative relationship between corrosion activity and magnetic field, and utilizes samples with a carefully controlled geometry [229]. The second involves nondestructive measurements of corrosion in lap joints removed from aging KC-135 and Boeing-707 aircraft [230]. Other applications under consideration include the magnetic measurement of filiform corrosion under paint, exfoliation corrosion within thick aircraft wing planks, and the effectiveness of corrosion prevention compounds in preventing hidden corrosion.

The preliminary work using SQUIDs to monitor currents from either exposed or hidden corrosion demonstrates that SQUIDs are well-suited for the periodic, non-destructive analysis of corrosion test specimens where the corrosion activity is not directly accessible to a potentiostat, *e.g.*, corrosion that is hidden under a thick coating or one or more layers of metal, such as in an aircraft lap joint. In fact, while numerous techniques (such as x-rays, ultrasound, thermal-wave, visual, and eddy-current measurements) can detect the accumulated metal loss associated with long-term corrosion in aircraft structures, SQUIDs may be the only instrument that can detect nondestructively the instantaneous currents associated with hidden corrosion. However, before the full capability of SQUID magnetometers can be utilized for obtaining the rates of hidden corrosion, research is required to establish from fundamental principles the factors governing the relationship between corrosion currents and their magnetic fields.

While SQUIDs appear to be a powerful technique for studying corrosion in the laboratory, one must be careful not to assume that transition of this technique to the flight line will be easy. Because properly prepared and treated aircraft do not corrode rapidly, the magnetic fields associated with corrosion in aircraft aluminum are weak relative to the geomagnetic field, environmental magnetic noise, the magnetic field from ferromagnetic fasteners, and the magnetic fields resulting from thermoelectric currents associated with temperature gradients and galvanic fields associative with contact between dissimilar metals [122]. Each of these other field sources can be controlled in a laboratory environment either through magnetic

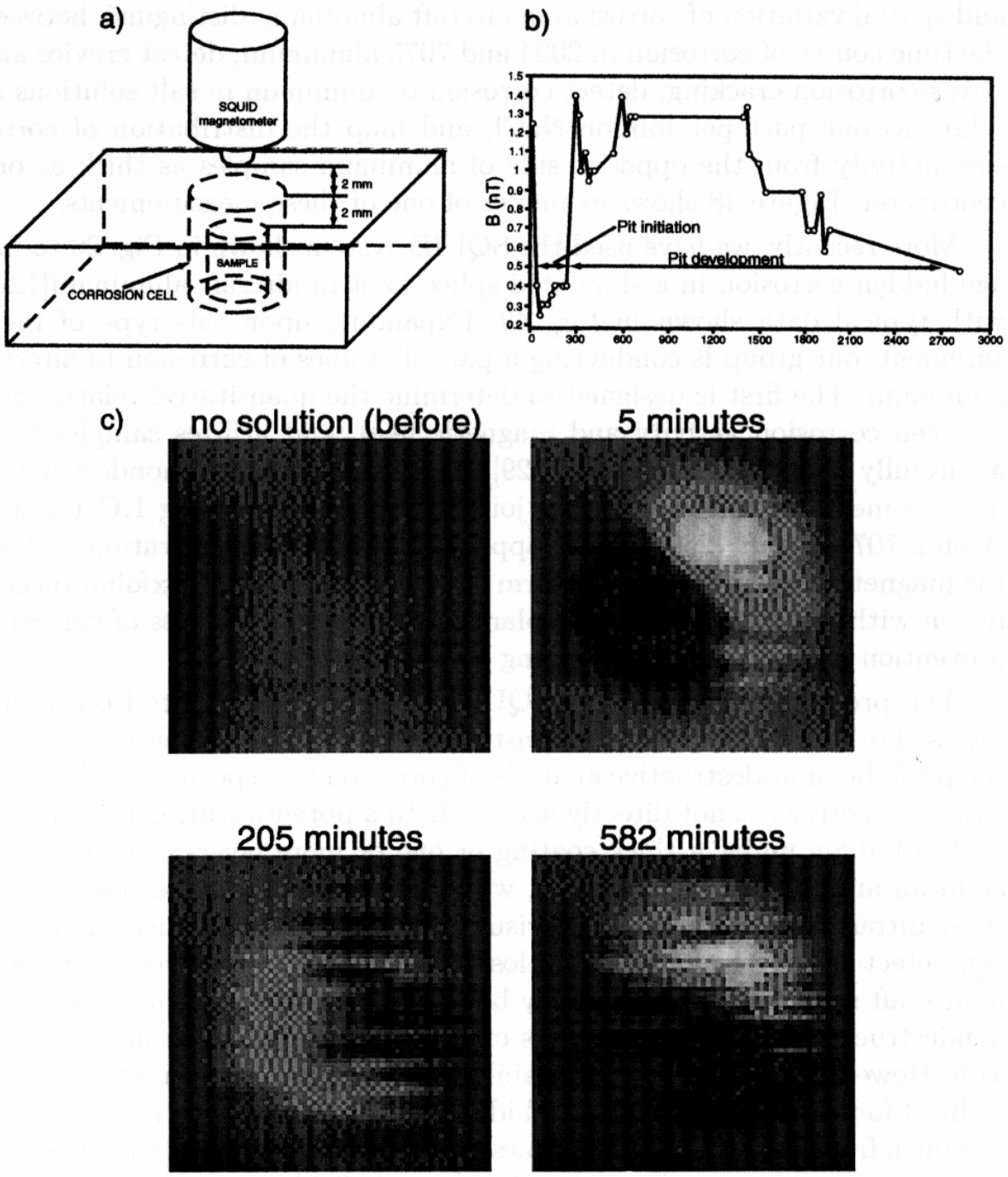

Figure 48. Active pitting corrosion mapped with MicroSQUID [225]. (a) A schematic of the active in-situ corrosion system, with 7075 aluminum alloy in a solution of 3.5% NaCl + 5ppm Cu^{++}. (b) The maximum magnetic field as a function of time during pitting corrosion. The first 300 minutes represents pit initiation followed by an increase in magnetic field magnitude signifying the onset of the pit development phase. (c) Images of the magnetic field as a function of time. (Courtesy of Yu Pei Ma)

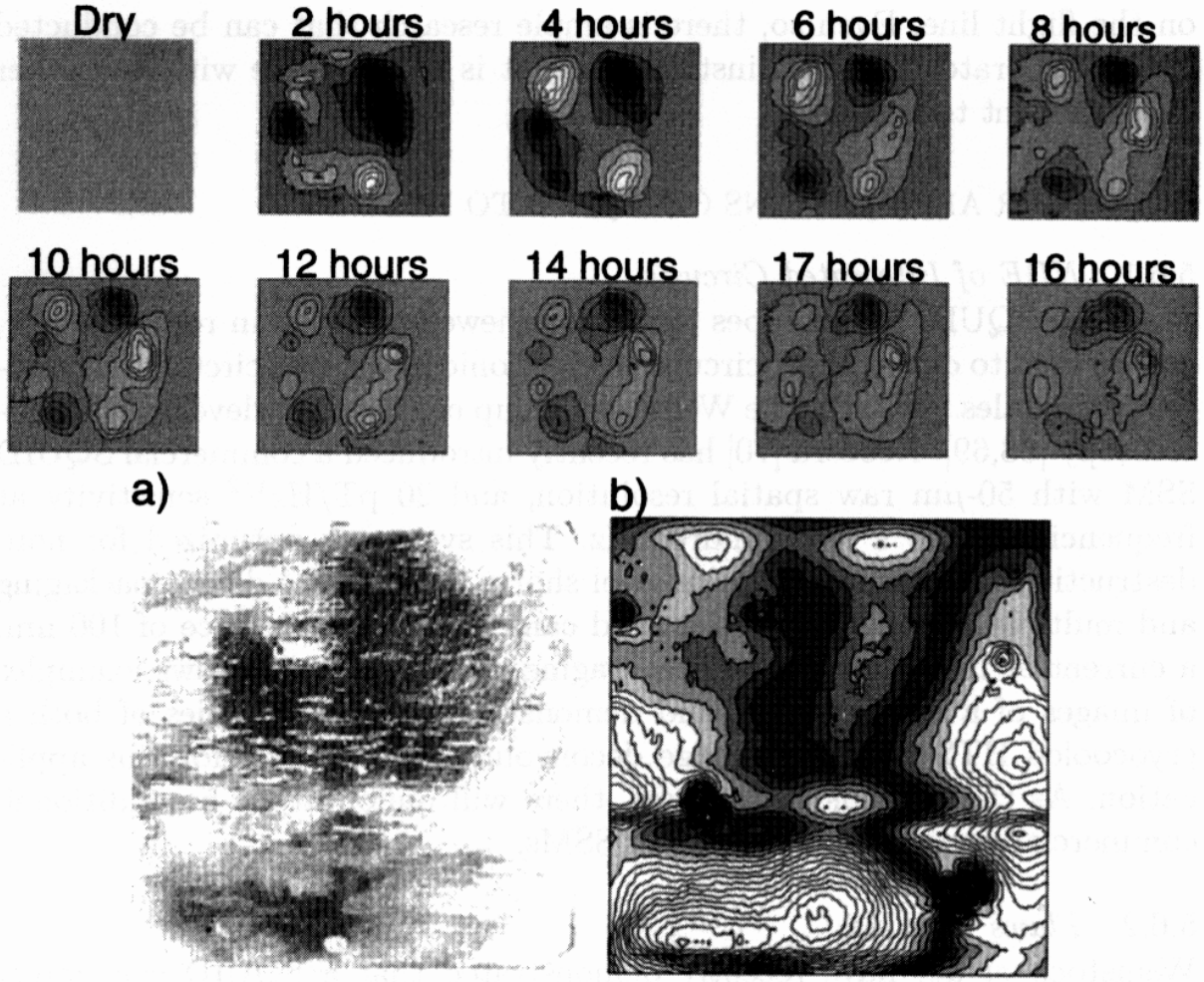

Figure 49. Examples of data obtained with the Vanderbilt corrosion SQUID system. Top: Rapid corrosion of aircraft aluminum. The lower surface of a 7-cm diameter, 1.2-mm thick, disk of 7075-T6 aluminum was exposed to a 0.5 M NaOH solution for 33 hours. The images present the change in the z-component of the magnetic field due to electrochemical corrosion for the first 18 hours of the experiment. All data were subtracted from the first (dry sample) image. The magnetic activity is localized to the area of the sample and presents a complex spatial and temporal structure. Bottom: Slow corrosion of aircraft aluminum. a) Photomicrograph of the lower (hidden) surface of a 3-inch square sample of 7075 aluminum that was exposed to a corrosive solution typical of an aircraft lap joint. The dark gray area in the upper center of the photograph corresponds to non-corroded aluminum. b) The magnetic activity of the sample after 2 hours of corrosion, showing the more active regions in white and less active regions in dark gray. (Photo by J. Dante and D. Peeler, Air Force Research Laboratory, Dayton, Ohio) (Adapted from [122])

shielding, the use of the stationary magnetometer or gradiometer, or proper sample preparation and degaussing techniques. There will be, of course, certain types of samples, such as ones with large ferromagnetic fasteners, for which it may be difficult to separate the corrosion signal from that due to other sources. However, at present it seems unlikely that this technique can be extended to measurements of corrosion signals in intact aircraft

on the flight line. Even so, there is ample research that can be conducted with a laboratory SQUID instrument that is not possible with any other measurement technique.

5.6. OTHER APPLICATIONS OF SQUIDS TO NDE

5.6.1. *NDE of Integrated Circuits*

Scanning SQUID microscopes (SSMs), reviewed in detail in reference [13], can be used to detect short circuits in electronic integrated circuits and multichip modules (MCM). The Wellstood group continues to develop HTS microscopy [68,69]. Neocera [70] has recently introduced a commercial SQUID SSM with 50-μm raw spatial resolution, and 20 pT/Hz$^{1/2}$ sensitivity at frequencies above a few hundred Hz. This system is optimized for nondestructive detection of package-level shorts through the device packaging and multiple metalization layers, and can detect, at a distance of 100 nm, a current of 10 nA with a 1-sec averaging time. Figure 50 shows examples of images of a faulty MCM, and demonstrates the capabilities of both a cryocooled HTS SSM and image deconvolution techniques for this application. As the technology matures, there will undoubtedly be additional, commercially-viable applications of SSMs.

5.6.2. *Flaws in Wires*

Weinstock *et al.*, have recently demonstrated that a SQUID can detect imperfections in wire stock prior to it being drawn into a fine wire [37]. They used a scanning SQUID to image the field perturbation associated with a 300 μm hole drilled partway into 500-μm diameter copper and aluminum wires carrying 16 mA at a kilohertz. A similar approach was used to detect, in composite superconducting wires at room temperature, the magnetic field fluctuations that are associated with conductivity anomalies that result from sausage-like discontinuities in individual strands of the conductor. The sensitivity of the technique is limited by the linearity of the wire. Fortunately, superconducting wire is sufficiently stiff that this approach can be readily applicable to quality control during manufacture or acceptance testing of composite superconducting wire, while it may be somewhat more difficult to utilize this in the soft-wire industry. There could be significant financial or practical benefits from finding flaws in wire stock before drawing it to a finer gauge or in stranded superconductor wire prior to the winding of expensive magnets.

6. Criteria for Successful Applications

SQUID magnetometers have been in use for biomagnetic measurements for thirty years, and for nondestructive testing about half that time. SQUIDs

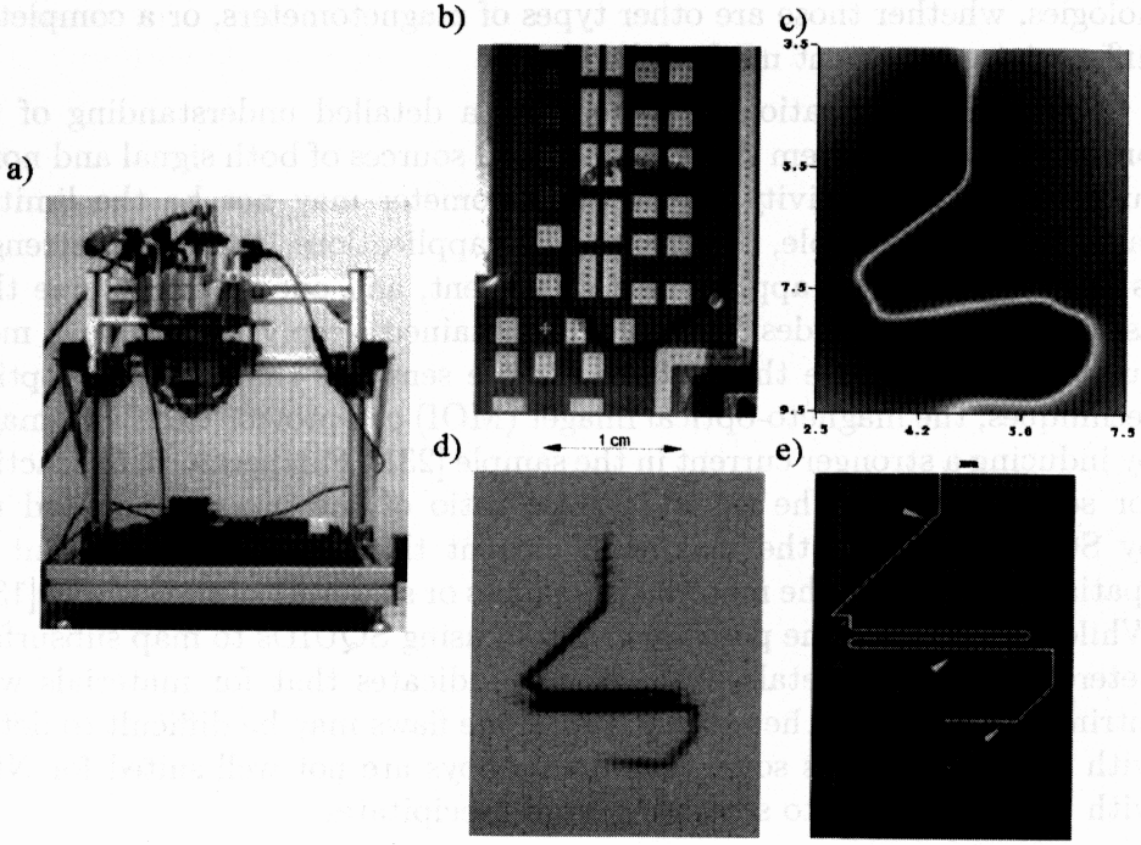

Figure 50. SQUID imaging of integrated circuits obtained by a cryocooled HTS SSM with a working distance of 340 μm between the SQUID and the multilayer circuits within the intact, room-temperature package [70]. a) A prototype of the Neocera HTS SSM developed specifically for imaging integrated circuits. b) An optical photograph of a multichip module (MCM) package. The hand-drawn circle indicates the region where a short was localized with thermography. c) The raw magnetic image obtained from a scan of the component of the magnetic field perpendicular to the area of the sample in (b). The wide white line corresponds to the region of zero field in the z direction, which to a first approximation corresponds to the path of localized current; the magnetic field is of opposite sign on either side of this line. d) The image of the current found from this field using inverse spatial filtering. The spatial resolution measured across the serpentine path of current has a full-width at half-maximum of 75 μm or ± 38 μm. e) Comparison of the data obtained from the SSM when overlaid with the circuit drawings allowed the location of the circuit fault to be located with an accuracy of better than ± 40 μm. The computed current path is shown in white on top of the background metalization. (Courtesy of Lee Knauss of Neocera, Inc.)

can provide outstanding sensitivity and spatial resolution, but at a significant fiscal and technical cost. Hence SQUID magnetometers are very good for certain types of measurements, and not terribly good for others. The primary challenge in the successful application of a SQUID to a new problem is to identify as quickly as possible whether SQUIDs would be preferred over another approach. Possibly the most important factor in making this determination is a clear understanding of both the nature and importance of the phenomena being studied and the capabilities of competing tech-

nologies, whether those are other types of magnetometers, or a completely different measurement methodology.

Successful application often requires a detailed understanding of the properties of the system being studied and sources of both signal and noise, such that the sensitivity of the magnetometer may not be the limiting factor. As an example, for many NDE applications, the signal strength is determined by an applied field or current, and one might assume that as large a signal as desired could be obtained simply by applying more current. Hence, while the SQUID is more sensitive than magneto-optical techniques, the magneto-optical imager (MOI) can provide excellent images by inducing a stronger current in the sample [231]. Furthermore, in practice, for some materials the signal-to-noise ratio of the image is limited not by SQUID noise or the maximum current that can be applied, but by spatial variations in the material properties or structure of the sample [139]. While this suggests the possible utility of using SQUIDs to map subsurface heterogeneities in metals [232], it also indicates that for materials with intrinsic conductivity heterogeneities, some flaws may be difficult to detect with SQUIDs, just as some aluminum alloys are not well-suited for NDE with ultrasound due to scattering from precipitates.

In assessing the competition, one must ask "What are the capabilities and limitations of other measurement techniques that do not require the use of superconductivity?" The very best applications of SQUIDs are those for which there is no competition. After twenty years of work, our group has identified several niche areas where SQUIDs offer capabilities that cannot be approached by other measurement techniques: other than by magnetic imaging with SQUIDs, there is no technique capable of determining the spatial distribution and temporal behavior of hidden corrosion activity within aircraft lap joints. There are no clinical techniques, other than magnetoenterography, that can noninvasively diagnose electrical, and hence ischemic, disorders of the human small intestine. SQUID microscopes may be the only technique suitable for high resolution magnetic analysis of thin geological specimens. There are, of course, other applications for which SQUIDs are uniquely suited.

Another class of SQUID applications offers only a differential benefit over other techniques. Fetal magnetocardiography has competition from ultrasound measurements and limited electrical measurements, so the benefits of fetal magnetocardiography will be determined in part by the relative cost of the technique as compared to the other diagnostic modalities, and the clinical utility of the additional information provided by the FMCG. The cost-benefit ratio is determined by engineering, and as SQUID magnetometers and cryogenic refrigerators become more sophisticated, the costs of these systems should decrease and the benefits rise. As another example,

clinically cardiology has the benefit of eighty years of diagnostic experience with the electrocardiogram, which has been used with many millions of patients worldwide. The clinical magnetocardiogram is in its infancy. The benefits of the magnetocardiogram over the electrocardiogram are at present still differential: only when there has been demonstrated a clear clinical advantage of the MCG over the ECG and there is a favorable cost-to-benefit ratio, will the technique become widely accepted.

For both the MCG and the MEG, the first two decades of research were limited to SQUID magnetometers with one or at most several recording channels. With the introduction of multi-channel SQUID arrays, such as the helmet systems for MEG, and the large-array, flat-bottomed system for the MCG, has it been possible to acquire enough high-quality data from a single subject to both learn new science and demonstrate the full capabilities of the technique. Hence one of the criteria for successful application of SQUID magnetometry is that the level of technical sophistication required must rise to the level required to compete with other modalities, some of which are both highly developed and extremely expensive.

The greatest effort in biomagnetism worldwide has been directed toward magnetoencephalography, for which there appear to be clear, albeit differential, benefits. While several dozen helmet systems have been installed worldwide, the technique is not yet universally accepted by the medical community. In part, the MEG has been an example of technology push rather than market pull. The physicists and engineers and businessmen promoting the MEG are working hard for the technique to be accepted. Were the differential benefits of the technique over other diagnostic procedures greater, or the cost-benefit analysis more favorable, the MEG would have become more widely accepted long ago. However, just because the cost-benefit analysis and the differential benefit are not as great as one might hope, there is still ample reason to pursue the development and commercialization of this technology.

In examining the competition to MEG, it is important to be aware that other techniques are developing just as SQUID magnetometry is being advanced (Obviously, the same considerations apply to other SQUID applications) [233]. In the past several years, there have been great advances in quantitative multielectrode electroencephalography [234–237], as well as in positron emission tomography (PET), magnetic resonance imaging (MRI), functional magnetic resonance imaging (fMRI), and single photon electron computed tomography (SPECT). Each of these techniques provide different diagnostic information and different spatial and temporal resolutions as shown in Fig. 51. One must remain aware of the competition, lest a competing technology advance sufficiently to render your technique obsolete!

The challenge is to identify those specific clinical measurements where

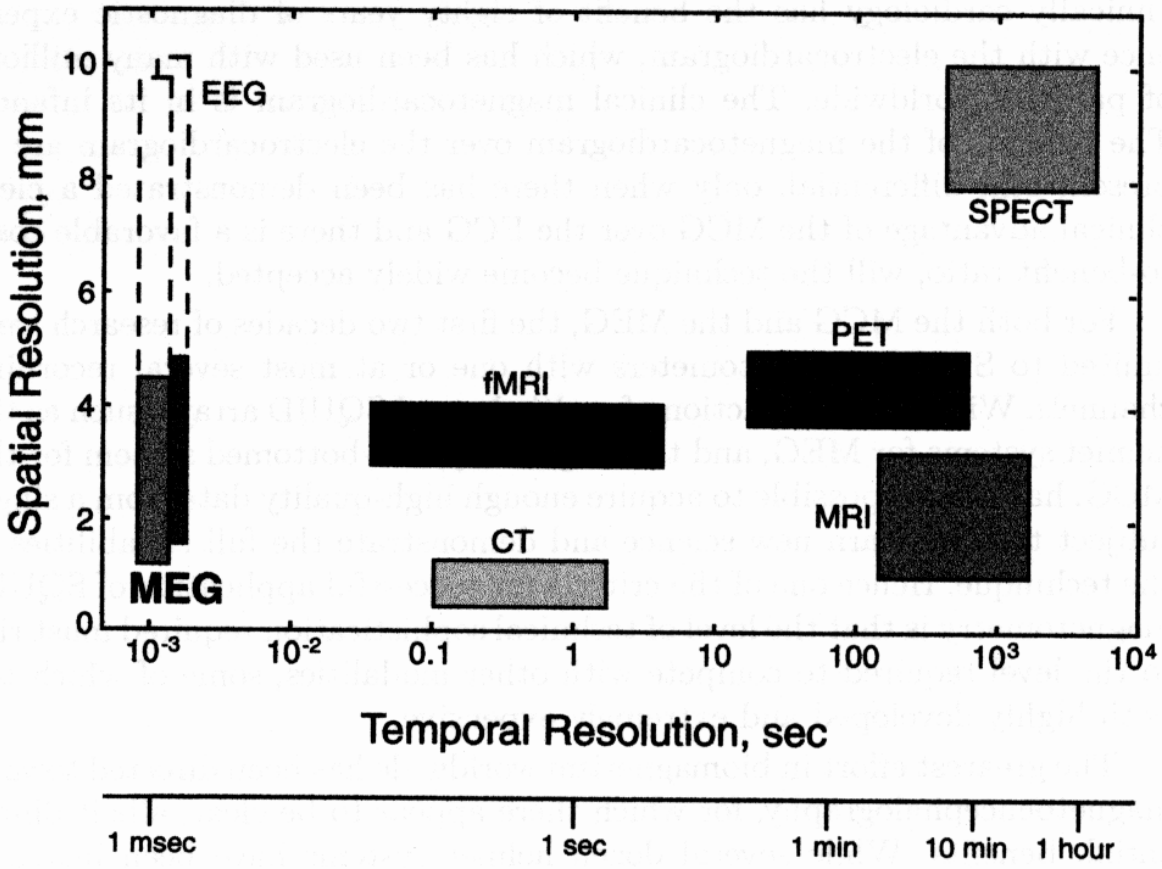

Figure 51. An approximate comparison of the spatial and temporal resolution of various brain-imaging modalities. The dotted boxes for MEG and EEG reflect the differences between localizing (solid) and imaging (dotted) resolution. (Adapted from [109])

the MEG provides information that is sufficiently important to justify the cost. One of the first examples of this limitation is the use of the MEG for a presurgical localization of critical cortical areas prior to the recession of tumors. This is now a proven technique, and is accepted for insurance reimbursement, but is not a sufficiently large clinical problem to justify massive investments in MEG facilities at more than a small number of centers.

An example with potentially favorable economics is the use of MEG to identify the focus of epileptic activity prior to surgical resection [110]. For medically-intractable epilepsy that might be treated surgically, it is important to determine whether there a single focal source, or at most several sources, that could be treated surgically [238]. At present, the surgical treatment of epilepsy is preceded by a detailed invasive study that costs between $40,000 and $50,000, in which electrodes are surgically implanted in the brain and monitored continuously for several days to determine the exact source of the epileptic seizures. Ideally, a noninvasive MEG study would be sufficiently precise so that an invasive study would not be

required. While there are only six thousand or so epilepsy surgeries performed in the US annually, the potential cost savings are significant. There are 25 to 40 epilepsy centers in the United States, most of whose patients would be potential customers for a non-invasive MEG study that might replace the more costly invasive one. However, for this to become an accepted technique, sufficient clinical data must be acquired to demonstrate the utility of the approach, and, most importantly, to obtain the required certification for reimbursement by insurance companies. In the case of the MEG, this might require a multi-center clinical study involving hundreds of epilepsy patients. Should such studies prove successful, MEG systems may be installed in the majority of the medical centers with major programs in epilepsy surgery.

The future of SQUID magnetometers is bright. The technology is continuing to develop in a manner that will improve performance and reduce both cost and technical complexity. The most obvious examples of the improving technology are the clinical systems with hundreds of channels, pulse-tube refrigerators, thin-film SQUID arrays, ultra-high-resolution scanning SQUID microscopes, and even digital SQUIDs. Applications for which SQUIDs are unique or have a clear advantage are being identified, explored, and introduced into the mainstream scientific literature. An important measure of success in the acceptance of SQUIDs as a measurement tool would be their full integration into a scientific or engineering discipline, such that the owners and users of the SQUIDs are not low temperature physicists or engineers, but geologists, biophysicists, physicians, or quality-assurance personnel. To reach that point, it is crucial that SQUID builders either work closely with such individuals, or attempt to make original contributions to those fields. It is not sufficient to build a marvelous SQUID device and expect the world to accept it! As magnetoencephalography has shown most clearly, the SQUID may be only a small part of a complete operating system: the success of the technique will be determined not in the arena defined by SQUID builders, but in the many different arenas that could benefit from a technology.

7. Acknowledgment

J. P. Wikswo, e-mail john.wikswo@vanderbilt.edu, fax 615-322-4977, phone 615-343-4124.

Preparation of this manuscript was supported in part by grants from the Air Force Office of Scientific Research and the National Institutes of Health.

Address reprint requests to John P. Wikswo, Living State Physics Group, Department of Physics and Astronomy, Vanderbilt University, Box 1807 Station B, Nashville, TN 37235, U.S.A.

I am indebted to the many people who have provided figures used in this paper: Eugene C. Hirschkoff of Biomagnetic Technologies, Inc.; Joachim Krause, Alex Braginski, and Helmut Soltner of Forschungszentrym Jülich; L. Alan Bradshaw, William B. Drake, Anthony P. Ewing, and Yu Pei Ma of Vanderbilt University; Gordon Donaldson, Sandy Cochran, Luke Morgan and Colin M. Pegrum of the University of Strathclyde; James Dante and Deborah Peeler of the Air Force Research Laboratory, Dayton, Ohio; Robert Fagaly of Tristan Technologies, Inc.; Christopher C. Gallen, formerly of Scripps Research Institute, La Jolla; John George and Christopher Wood of Los Alamos National Laboratory; Irina Gorodnitsky of the University of California, San Diego; Matti Hämäläinen and Olli V. Lounasmaa of Helsinki University of Technology; Mark B. Ketchen of the IBM Thomas J. Watson Research Center; Jeffrey D. Lewine, formerly of the University of New Mexico; Lutz Trahms of Physickalisch-Technicshe Bundesanstalt, Berlin (PTB); Steve Robinson and Jiri Vrba of CTF Systems, Inc.; Ron Wakai of the University of Wisconsin; Harold Weinstock of the Air Force Office of Scientific Research; and Samuel J. Williamson of New York University.

I appreciate comments on this manuscript by Leonora Wikswo. I especially want to thank Don Berry for his attention to detail with the illustrations and references, Jenifer Goodwin for her care in preparing the illustrations, and Cheryl Cosby for her unflagging assistance.

References

1. Cohen, D., Edelsack, E.A., and Zimmerman, J.E. (1970) Magnetocardiograms taken inside a shielded room with a superconducting point-contact magnetometer, *Appl. Phys. Lett.* **16(7)**, 278–280.
2. Weinstock, H. and Nisenoff, M. (1985) Non-destructive evaluation of metallic structures using a SQUID gradiometer, in H.D. Hahlbohm and H. Lübbig (eds.), *SQUID '85, Proc. 3rd International Conference on Superconducting Quantum Devices*, de Gruyter, Berlin, pp. 843–847.
3. Wikswo, Jr., J.P. (1983) Theoretical aspects of the ECG-MCG relationship, in S.J. Williamson, G.-L. Romani, L. Kaufman, and I. Modena (eds.), *Biomagnetism, An Interdisciplinary Approach*, Plenum Press, New York, pp. 311–326.
4. Donaldson, G.B. (1980) SQUIDs for everything else, in H. Weinstock and M. Nisenoff (eds.), *Superconducting Electronics*, Springer-Verlag, New York, pp. 175–207.
5. Wikswo, Jr., J.P. (1990) Biomagnetic sources and their models, in S.J. Williamson, M. Hoke, G. Stroink, and M. Kotani (eds.), *Advances in Biomagnetism*, Plenum Press, New York, pp. 1–18.
6. Weinstock, H. (1991) A review of SQUID magnetometry applied to nondestructive evaluation, *IEEE Trans. Mag.* **27(2)**, 3231–3236.
7. Jenks, W.G., Sadeghi, S.S.H., and Wikswo, Jr., J.P. (1997) A review of SQUID magnetometers for non-destructive testing, *J. Phys. D* **30(3)**, 293–323.
8. Clarke, J. (1980) Principles and applications of SQUIDs, *Proc. IEEE* **77**, 1208–1223.
9. Fagaly, R.L. (1990) Neuromagnetic instrumentation, in S. Sato (ed.), *Advances in Neurology*, Raven Press, New York, vol. 54, pp. 11–32.

10. Wikswo, Jr., J.P. (1996) High-resolution magnetic imaging: Cellular action currents and other applications, in H. Weinstock (ed.), *SQUID Sensors: Fundamentals, Fabrication and Applications*, Kluwer Academic Publishers, Netherlands, pp. 307–360.
11. Wikswo, Jr., J.P. (1996) The magnetic inverse problem for NDE, in H. Weinstock (ed.), *SQUID Sensors: Fundamentals, Fabrication and Applications*, Kluwer Academic Publishers, Netherlands, pp. 629–695.
12. Andrä, W. and Nowak, H. (1998) *Magnetism in Medicine: A handbook*, Wiley-VCH, New York.
13. Kirtley, J.R. and Wikswo, Jr., J.P. (1999) Scanning SQUID microscopy, *Annu. Rev. Mater. Sci.* **29**, 117-148.
14. Lounasmaa, O.V. (1996) Medical applications of SQUIDs in neuro- and cardiomagnetism, *Physica Scripta* **T66**, 70–79.
15. Gulrajani, R.M. (1998) *Bioelectricity and Biomagnetism*, John Wiley, New York.
16. Wikswo, Jr., J.P. (1995) SQUID magnetometers for biomagnetism and nondestructive testing: Important questions and initial answers, *IEEE Trans. Applied Supercond.* **5(2)**, 74–120.
17. Cohen, D. (1972) Magnetoencephalography: Detection of the brain's electrical activity with a superconducting magnetometer, *Science* **175**, 664–666.
18. Okada, Y.C. (1983) Neurogenesis of evoked magnetic fields, in S.J. Williamson, G.-L. Romani, L. Kaufman, and I. Modena (eds.), *Biomagnetism, An Interdisciplinary Approach*, Plenum Press, New York, pp. 399–408.
19. Vrba, J., Angus, V., Betts, K., Burbank, M.B., Cheung, T., Fife, A.A., Haid, G., Kubik, P.R., Lee, S., Ludwig, W., McCubbin, J., McKay, J., McKenzie, D., Robinson, S.E., Smith, M., Spear, P., Taylor, B., Tillptson, M., Cheyne, D., and Weinberg, H. (1996) 143 channel whole-cortex MEG system, *Proc. 10th Inter. Conf. on Biomagnetism*, Sante Fe, p. 346.
20. Zeng, X.H., Soltner, H., Selbig, D., Bode, M., Bick, M., Ruders, F., Schubert, J., Zander, W., Banzet, M., Zhang, Y., Bousack, H., and Braginski, A.I. (1998) A high-temperature rf SQUID system for magnetocardiography, *Measurement Science and Technology* **9**, 1600–1608.
21. Drung, D. (1995) The PTB 83-SQUID system for biomagnetic applications in a clinic, *IEEE Trans. Applied Supercond.* **5(3)**, 1051–8223.
22. Fischer, R. (1998) Liver iron susceptometry, in W. Andrä and H. Nowak (eds.), *Magnetism in Medicine: A handbook*, Wiley-VCH, New York, pp. 286–301.
23. Kalliomaki, P.-L., Korhonen, O., Vaaranen, V., Kalliomaki, K., and Koponen, M. (1978), Lung Retention and Clearance of Shipyard Arc Welders, *Internat. Arch. Occupational and Environmental Health* **42** 83–90.
24. Kötitz, R., Fannin, P.C., and Trahms, L. (1995) Time domain study of Brownian and Néel relaxation in ferrofluids, *J. Magnetism and Magnetic Materials* **149**, 42–46.
25. Kötitz, R., Weitschies, W., Trahms, L., and Semmler, W. (1999) Investigation of Brownian and Néel relaxation in magnetic fields, *J. Magnetism and Magnetic Materials* **201**, 102–104.
26. Kötitz, R., Weitschies, W., Trahms, L., Brewer, W., and Semmler, W. (1999) Determination of the binding reaction between avidin and biotin by relaxation measurements of magnetic nanoparticles, *J. Magnetism and Magnetic Materials* **194(1-3)**, 62–68.
27. Ugelstad, J., Prestvik, W.S., Stenstad, P., Kilaas, L., and Kvalheim, G. (1998) Selective cell separation with monosized magnetizable polymer beads, in W. Andrä and H. Nowak (eds.), *Magnetism in Medicine: A handbook*, Wiley-VCH, New York, pp. 471–488.
28. Wikswo, Jr., J.P., Ma, Y.P., Sepulveda, N.G., Tan, S., Thomas, I.M., and Lauder, A. (1993) Magnetic susceptibility imaging for nondestructive evaluation, *IEEE Trans. Applied Supercond.* **3(1)**, 1995–2002.
29. Roth, B.J., Sepulveda, N.G., and Wikswo, Jr., J.P. (1989) Using a magnetometer to image a two-dimensional current distribution, *J. Appl. Phys.* **65**, 361–372.

30. Fagaly, R.L. (1989) SQUID detection of electronic circuits, *IEEE Trans. Mag.* **25**, 1204–1218.
31. Zhuravlev, Y.E., Bakharev, A.A., Matlashov, A.N., Slobodchikov, V.Y., Velt, I.D., Nikulin, S.L., and Kalashnikov, R.V. (1992) Application of dc-SQUID magnetometers for nondestructive testing of multilayer electronic cards, in H. Koch and H. Lübbig (eds.), *Superconducting Devices and Their Applications*, Springer-Verlag, Berlin, vol. 64, pp. 581–583.
32. Tan, S., Ma, Y.P., Thomas, I.M., and Wikswo, Jr., J.P. (1993) High resolution SQUID imaging of current and magnetization distributions, *IEEE Trans. Applied Supercond.* **3(1)**, 1945–1948.
33. Thomas, I.M., Moyer, T.C., and Wikswo, Jr., J.P. (1992) High resolution magnetic susceptibility imaging of geological thin sections: Pilot study of a pyroclastic sample from the Bishop tuff, *Geophys. Res. Lett.* **19(21)**, 2139–2142.
34. Kirschvink, J.L. (1997) Magnetoreception: Homing in on vertebrates, *Nature* **390(6658)**, 339–340.
35. Walker, M.M., Diebel, C.E., Haugh, C.V., Pankhurst, P.M., Montgomery, J.C., and Green, C.R. (1997) Structure and function of the vertebrate magnetic sense, *Nature* **390(6658)**, 371–376.
36. Thomas, I.M., Ma, Y.P., and Wikswo, Jr., J.P. (1993) SQUID NDE: Detection of surface flaws by magnetic decoration, *IEEE Trans. Applied Supercond.* **3(1)**, 1949–1952.
37. Weinstock, H., Tralshawala, N., and Claycomb, J.R. (1999) Defect detection in wire manufacturing, in D.O. Thompson and D.E. Chimenti (eds.), *Review of Progress in QNDE*, Plenum Press, New York, vol. 18B, 2265–2277.
38. Ma, Y.P. and Wikswo, Jr., J.P. (1992) Detection of a deep flaw inside a conductor using a SQUID magnetometer, in D.O. Thompson and D.E. Chimenti (eds.), *Review of Progress in QNDE*, Plenum Press, New York, vol. 11A, pp. 1153–1159.
39. Ma, Y.P. and Wikswo, Jr., J.P. (1993) Imaging subsurface defects using SQUID magnetometers, in D.O. Thompson and D.E. Chimenti (eds.), *Review of Progress in QNDE*, Plenum Press, New York, vol. 12A, pp. 1137–1143.
40. Hurley, D.C., Ma, Y.P., Tan, S., and Wikswo, Jr., J.P. (1993) Imaging of small defects in nonmagnetic tubing using a SQUID magnetometer, *Res. Nondestr. Eval.* **5**, 1–29.
41. Wikswo, Jr., J.P., Ma, Y.P., Sepulveda, N.G., Staton, D.J., Tan, S., and Thomas, I.M. (1993) Superconducting magnetometry: A possible technique for aircraft NDE, in M.T. Valley, N.K. Grande, and A.S. Kobayashi (eds.), *Nondestructive Inspection of Aging Aircraft*, SPIE Proceedings, vol. 2001, pp. 164–190.
42. Wikswo, Jr., J.P. (1997) SQUID magnetometers for studying corrosion and corrosion protection in aircraft aluminum, *NACE International*, Paper No. 293, pp. 1–17.
43. Ma, Y.P. and Wikswo, Jr., J.P. (1993) Detection of subsurface flaws using SQUID eddy current technique, in M.T. Valley, N.K. Grande, and A.S. Kobayashi (eds.), *Nondestructive Inspection of Aging Aircraft*, SPIE Proceedings, vol. 2001, pp. 191–199.
44. Podney, W. (1994) A superconductive electromagnetic microscope for eddy current evaluation of materials, in D.O. Thompson and D.E. Chimenti (eds.), *Review of Progress in QNDE*, Plenum Press, New York, vol. 13B, pp. 1947–1954.
45. Ma, Y.P. and Wikswo, Jr., J.P. (1994) SQUID eddy current techniques for detection of second layer flaws, in D.O. Thompson and D.E. Chimenti (eds.), *Review of Progress in QNDE*, Plenum Press, New York, vol. 13A, pp. 303–309.
46. Banchet, J., Jouglar, J., Vuillermoz, P.-L., Waltz, P., and Weinstock, H. (1995) Evaluation of stress in steel via SQUID magnetometry, in D.O. Thompson and D.E. Chimenti (eds.), *Review of Progress in QNDE*, Plenum Press, New York, vol. 14B, pp. 1675–1682.
47. Thomas, I.M., Ma, Y.P., Tan, S., and Wikswo, Jr., J.P. (1993) Spatial resolution and sensitivity of magnetic susceptibility imaging, *IEEE Trans. Applied Supercond.*

3(1), 1937–1940.
48. Wikswo, Jr., J.P. and van Egeraat, J.M. (1991) Cellular magnetic fields: Fundamental and applied measurements on nerve axons, peripheral nerve bundles, and skeletal muscle, *J. Clin. Neurophysiol.* **8(2)**, 170–188.
49. Deeter, M.N., Rose, A.H., and Day, G.W. (1990) Iron-garnet magnetic field sensors with 100 $pT/Hz^{1/2}$ noise-equivalent field, *Proc. 7th Int. Conf. Optical Fiber Sensors*, Sydney.
50. Deeter, M.N., Rose, A.H., and Day, G.W. (1991) Sensitivity limits to ferromagnetic Faraday effect magnetic field sensors, *J. Appl. Phys.* **70(10)**, 6407–6409.
51. Deeter, M.N., Day, G.W., Beahn, T.J., and Manheimer, M. (1993) Magneto-optic field sensor with 1.4 $pT/Hz^{1/2}$ minimum detectable field at 1 kHz, *Electron. Lett.* **29**, 993–994.
52. Smith, N., Jeffers, F., and Freeman, J. (1991) A high-sensitivity magnetoresistive magnetometer, *J. Appl. Phys.* **69(8)**, 5082–5084.
53. Thompson, C.A., Cross, R.W., and Kos, A.B. (1994) Micromagnetic scanning microprobe system, *Rev. Sci. Instrum.* **65(2)**, 383–389.
54. Mahendiran, R. and Raychaudhuri, A.K. (1995) Low temperature linear magnetic field sensor based on magnetoresistance of the perovskite oxide La-Sr-Co-O, *Rev. Sci. Instrum.* **66**, 3071–3072.
55. Yamamoto, S. and Schultz, S. (1996) Scanning magnetoresistance microscopy, *Appl. Phys. Lett.* **69**, 3263–3265.
56. Schwarzacher, S. and Lashmore, D.S. (1996) Giant magnetoresistance in electrodeposited films, *IEEE Trans. Mag.* **32(4)**, 3133–3153.
57. Non-Volatile Electronics, Inc., Eden Prairie, MN.
58. Jenks, W.G, Thomas, I.M., and Wikswo, Jr., J.P. (1997) SQUIDs, in G.L. Trigg, E.S. Vera, and W. Greulich (eds.), *Encyclopedia of Applied Physics*, VCH Publishers, Inc., New York, vol. 19, pp. 457–468.
59. Zimmerman, J.E. and Silver, A.H. (1964) Quantum effects in type II superconductors, *Phys. Lett.* **10(1)**, 47–48.
60. Jaklevic, R.C., Lambe, J., Mercereau, J.E., and Silver, A.H. (1965) Macroscopic quantum interference in superconductors, *Physical Review* **140(5A)**, A1628–A1637.
61. See chapter by J. Clarke, this volume.
62. Zhang, Y., Krüger, U., Kutzner, R., Wördenweber, R., Schubert, J., Zander, W., Strupp, M., Sodtke, E., and Braginski, A.I. (1994) Single-layer $YBa_2Cu_3O_7$ rf SQUID magnetometers with direct-coupled pickup coils and flip-chip flux transformers, *Appl. Phys. Lett.* **65**, 3380–3382.
63. Ludwig, F., Dantsker, E., Kleiner, R., Koelle, D., Clarke, J., Knappe, S., Drung, D., Koch, H., Alford, N., and Button, T.W. (1995) Integrated high-Tc multiloop magnetometer, *Appl. Phys. Lett.* **66**, 1418–1420.
64. Burghoff, M., Trahms, L., Zhang, Y., Bousack, H., and Borgmann, J. (1996) Diagnostic application of high-temperature SQUIDS, *J. Clin. Engr.* **21(1)**, 62–66.
65. Cochran, A., Macfarlane, J.C., Morgan, L.N.C., Kuznik, J., Weston, R., Hao, L., Bowman, R.M., and Donaldson, G.B. (1994) Using a 77 K SQUID to measure magnetic fields for NDE, *IEEE Trans. Applied Supercond.* **4(3)**, 128–135.
66. Morgan, L.N.C., Carr, C., Cochran, A., McKirdy, D.McA., and Donaldson, G.B. (1995) Electromagnetic nondestructive evaluation with simple HTS SQUIDs: Measurements and modelling, *IEEE Trans. Applied Supercond.* **5(2)**, 3127–3130.
67. Grüneklee, M., Krause, H.-J., Hohmann, R., Maus, M., Lomparski, D., Banzet, M., Schubert, J., Zander, Y., Zhang, Y., Wolf, W., Bousack, H., and Braginski, A.I. (1998) HTS SQUID system for eddy current testing of airplane wheels and rivets, in D.O. Thompson and D.E. Chimenti (eds.), *Review of Progress in QNDE*, Plenum Press, New York, vol. 17A, pp. 1075–1082.
68. Chatraphorn, S., Fleet, E.F., and Wellstood, F.C. (1999) High-T_c scanning SQUID microscopy: Imaging integrated circuits beyond the standard near-field limit, *Bull.*

Am. Phys. Soc. **44(1) Part II**, 1554 (Abstract).
69. Fleet, E.F., Chatraphorn, S., and Wellstood, F.C. (1999) HTS SQUID microscopy of eddy currents, *Bull. Am. Phys. Soc.* **44(1) Part II**, 1554 (Abstract).
70. http://www.neocera.com/html-files/magma/magma.htm
71. Drung, D., Crocoll, E., Herwig, R., Neuhas, M., and Jutzi, W. (1989) Measured performance parameters of gradiometers with digital output, *IEEE Trans. Mag.* **25**, 1034–1037.
72. Vrba, J., Betts, K., Burbank, M., Cheung, T., Cheyne, D., and Fife, A.A. (1995) Whole cortex 64 channel system for shielded and unshielded environments, in L. Deecke, C. Baumgartner, G. Stroink, and S.J. Williamson (eds.), *Proc. of the 9th Inter. Conf. on Biomagnetism*, Vienna, pp. 521–525.
73. Zimmermann, E., Brandenburg, G., Clemens, U., Rongen, H., Halling, H., Krause, H.-J., Hohmann, R., Soltner, H., Lomparski, D., Grüneklee, M., Husemann, K.-D., Bousack, H., Braginski, A.I. (1997) HTS-SQUID magnetometer with digital feedback control for NDE applications, in D.O. Thompson and D.E. Chimenti (eds.), *Review of Progress in QNDE*, Plenum Press, New York, vol. 16B, pp. 2129–2135.
74. Fujimaki, N., Tamura, H., Suzuki, H., Imamura, T., Hasuo, S., and Shibatomi, A. (1988) A single-chip SQUID magnetometer, *IEEE Trans. Elect. Dev.* **35**, 2412–2417.
75. Radparvar, M. (1994) A wide dynamic range single-chip SQUID magnetometer, *IEEE Trans. Applied Supercond.* **4**, 87–91.
76. Radparvar, M. and Rylov, S. (1995) A single-chip SQUID magnetometer with high sensitivity input, *IEEE Trans. Applied Supercond.* **5**, 2142–2145.
77. Radparvar, M. and Rylov, S. (1997) High sensitivity digital SQUID magnetometers, *IEEE Trans. Applied Supercond.* **7**, 3682–3685.
78. See chapter by K.K. Likharev, this volume.
79. Wikswo, Jr., J.P. (1995) Closing Comments: Recent developments in 5 K cryocoolers - An outsider's view, *5 K Cryocooler Workshop: Present Status, Future Prospects and Market Potential for 4-5 K Cryocoolers Proceedings*, Hypres, Inc., Elmsford, NY, pp. 58–66.
80. Klemic, G.A., Buchanan, D.S., Cycoqicz, Y.M., and Williamson, S.J. (1990) Sequential spatially distributed activity of the human brain detected magnetically by CryoSQUIDs, in S.J. Williamson, M. Hoke, G. Stroink, and M. Kotani (eds.), *Advances in Biomagnetism*, Plenum Press, New York, pp. 685–688.
81. Buchanan, D.S., Paulson, D., and Williamson, S.J.(1988) Instrumentation for clinical applications of neuromagnetism, in R.W. Fast (ed.), *Advances in Cryogenic Engineering*, Plenum Press, New York, vol. 33, pp. 97–106.
82. Podney, W.N. (1993) Performance measurements of a superconductive microprobe for eddy current evaluation of subsurface flaws, *IEEE Trans. Applied Supercond.* **3(1)**, 1914–1917.
83. Hohmann, R., Lienerth, C., Zhang, Y., Bousack, H., Thummes, G., and Heiden, C. (in press, 1999) Comparison of low noise cooling performance of a Joule-Thompson cooler and a pulse-tube cooler using a HT SQUID, *IEEE Trans. Applied Supercond.*
84. Little, W.A. (1984) Microminiature refrigeration, *Rev. Sci. Instrum.* **55**, 661–680.
85. Little, W.A. (1990) Advances in Joule-Thomson cooling, *Adv. Cryogenic Engr.* **35**, 1305–1314.
86. Kajiwara, G., Harakawa, K., and Ogata, H. (1996) High-performance magnetically shielded room, *IEEE Trans. Mag.* **32**, 2582–2585.
87. Drung, D. (1992) Investigation of a double-loop dc-SQUID magnetometer with additional positive feedback (for biomagnetic applications), in H. Koch and H. Lübbig (eds.), *Superconducting Devices and Their Applications*, Springer-Verlag, Berlin, vol. 64, pp. 351–356.
88. Trahms, Lutż, PTB, personal communication.
89. Romani, G.L., Williamson, S.J., and Kaufman, L. (1982) Biomagnetic instrumentation, *Rev. Sci. Instrum.* **53**, 1815–1845.
90. Wikswo, Jr., J.P. (1978) Optimization of SQUID differential magnetometers, *AIP*

Conf. Proc. **44**, 145–149.
91. Cochran, A., Donaldson, G.B., Evanson, S., and Bain, R.J.P. (1993) First-generation SQUID-based nondestructive testing system, *IEE Proceedings-A* **140(2)**, 113–120.
92. Zimmerman, J.E. (1977) SQUID instruments and shielding for low-level magnetic measurements, *J. Appl. Phys.* **48(2)**, 702–710.
93. Tsukada, K. and Haruta, Y. (1995) Multichannel SQUID system detecting tangential components of the cardiac magnetic field, *Rev. Sci. Instrum.* **66(10)**, 5085–5091.
94. Sepulveda, N.G. and Wikswo, Jr., J.P. Differential operators and their applications to magnetic measurements using SQUID magnetometers, unpublished.
95. http://www.neuromag.com
96. Vrba, J., Taylor, B., Cheung, T., Fife, A.A., Haid, G., Kubik, P.R., Lee, S., McCubbin, J., and Burbank, M.B. (1995) Noise cancellation by a whole-cortex SQUID MEG system, *IEEE Trans. Applied Supercond.* **5(2)**, 2118–2123.
97. Robinson, Steve, personal communication.
98. Drung, D. (1992) Performance of an electronic gradiometer, in H. Koch and H. Lübbig (eds.), *Superconducting Devices and their Applications*, Springer-Verlag, New York, vol. 64, pp. 542–546.
99. Tavrin, Y., Zhang, Y., Mück, M., Braginski, A.I., and Heiden, C. (1993) $YBa_2Cu_3O_7$ thin film SQUID gradiometer for biomagnetic measurements, *Appl. Phys. Lett.* **62(15)**, 1824–1826.
100. Tavrin, Y., Zhang, Y., Wolf, W., and Braginski, A.I. (1994) A second-order SQUID gradiometer operating at 77 K, *Supercond. Sci. Technol.* **7**, 265–268.
101. Koch, R.H. (1992) Gradiometer having a magnetometer which cancels background magnetic field from other magnetometers, *U.S. Patent 5,122,744.*
102. Koch, R.H., Rozen, J.R., Sun, J.Z., and Gallagher, W.J. (1993) Three SQUID gradiometer, *Appl. Phys. Lett.* **63(3)**, 403–405.
103. Ter Brake, H.J.M., Flokstra, J., Jaszczuk, W., Stammis, R., van Ancum, G.K., Martinez, A., and Rogalla, H. (1991) 19 UT 19-channel dc SQUID based neuromagnetometer, *Clin. Phys. and Physiol. Meas.* **12(Suppl. B)**, 45–50.
104. Matlashov, A.N., Slobodchikov, V.Y., Bakharev, A.A., Zhuravlev, Y.E., and Bondarenko, N. (1995) Biomagnetic multichannel system built with 19 cryogenic probes, in L. Deecke, C. Baumgartner, G. Stroink, and S.J. Williamson (eds.), *Proc. 9th Inter. Conf. on Biomagnetism*, Vienna, pp. 493–496.
105. Matlashov, A., Zhuravlev, Y., Slobodchikov, V., Bondarenko, N., Bakharev, A., and Rassi, D. (1995) Miniature dc SQUID magnetometers for clinical use, in L. Deecke, C. Baumgartner, G. Stroink, and S.J. Williamson (eds.), *Proc. 9th Inter. Conf. on Biomagnetism*, Vienna, pp. 526–529.
106. Dössel, O., David, B., Fuchs, M., Krüger, J., Lüdeke, K.-M., and Wischmann, H.-A. (1993) A 31-channel SQUID system for biomagnetic imaging, *Applied Supercond.* **1(10-12)**, 1813–1825.
107. Yamasaki, S., Morooka, T., Matsuda, N., Kawai, J., Mizutani, N., Tsukada, K., Uehara, G., and Kado, H. (1993) Design and fabrication of multichannel dc SQUIDs for biomagnetic applications, *IEEE Trans. Applied Supercond.* **3**, 1887–1889.
108. Romani, Gian Luca, personal communication.
109. http://www.ctf.com
110. Hirschkoff, Gene, Biomagnetic technologies, Inc., personal communication.
111. Ueda, M., Kandori, A., Ogata, H., Takada, Y., Komuro, T., Kazami, K., and Ito, T. (1995) Development of a biomagnetic measurement system for brain research, *IEEE Trans. Applied Supercond.* **5(2)**, 2465–2469.
112. Kado, H., Higuchi, M., Shimogawara, Y., Haruta, Y., Adachi, J., Kawai, H., and Uehara, G. (in press) Magnetoencephalogram systems developed at KIT, *IEEE Trans. Applied Supercond.*
113. Tan, S., Roth, B.J., and Wikswo, Jr., J.P. (1990) The magnetic field of cortical current sources: The application of a spatial filtering model to the forward and inverse problems, *Electroenceph. clin. Neurophysiol.* **76**, 73–85.

114. Matlashov, A., Bakharev, A., Zhuravlev, Y., and Slobdobchikov, V. (1992) Biomagnetic multi-channel system consisting of several self-contained autonomous small-size units, in H. Koch and H. Lübbig (eds.), *Superconducting Devices and Their Applications*, Springer-Verlag, Berlin, vol. 6, pp. 511–516.
115. Matlashov, A.N. (1993) New approaches to biomagnetic measurements and signal processing, *International Journal of Applied Electromagnetics in Materials*, Elsevier, Amsterdam, vol. 4, pp. 185–188.
116. Wikswo, Jr., J.P. (1988) High-resolution measurements of biomagnetic fields, in R.W. Fast (ed.), *Advances in Cryogenic Engineering*, vol. 33, pp. 107–116.
117. Cochran, A. and Donaldson, G.B. (1992) Improved techniques for structural NDT using SQUIDs, in H. Koch and Lübbig (eds.), *Superconducting Devices and Their Applications*, Springer-Verlag, Berlin, vol. 64, pp. 576–581.
118. Hibbs, A.D., Sager, R.E., Cox, D.W., Aukerman, T.H., Sage, T.A., and Landis, R.S. (1992) A high-resolution magnetic imaging system based on a SQUID magnetometer, *Rev. Sci. Instrum.* **63(7)**, 3652–3658.
119. Hibbs, A., Chung, R., and Pence, J.S. (1994) Corrosion measurements with a high resolution scanning magnetometer, in D.O. Thompson and D.E. Chimenti (eds.), *Review of Progress in QNDE*, Plenum Press, New York, vol. 13B, pp. 1955–1962.
120. Wikswo, Jr., J.P., van Egeraat, J.M., Ma, Y.P., Sepulveda, N.G., Staton, D.J., Tan, S., and Wijesinghe, R.S. (1990) Instrumentation and techniques for high-resolution magnetic imaging, in A.F. Gmitro, P.S. Idell, and I.J. LaHaie (eds.), *Digital Image Synthesis and Inverse Optics*, SPIE Proceedings, vol. 1351, pp. 438–470.
121. Ma, Y.P. and Wikswo, Jr., J.P. (1991) Magnetic shield for wide-bandwidth magnetic measurements for nondestructive testing and biomagnetism, *Rev. Sci. Instrum.* **62(11)**, 2654–2661.
122. Abedi, A., Fellenstein, J.J., Lucas, A.J., and Wikswo, Jr., J.P. (in press) A SQUID magnetometer system for quantitative analysis and imaging of hidden corrosion activity in aircraft aluminum structures, *Rev. Sci. Instrum.*
123. Brenner, D., Williamson, S.J., and Kaufman, L. (1975) Visually evoked magnetic fields of the human brain, *Science* **190**, 480–482.
124. Brenner, D., Lipton, J., Kaufman, L., and Williamson, S.J. (1978) Somatically evoked magnetic fields of the human brain, *Science* **199**, 81–83.
125. Romani, G.L., Williamson, S.J., and Kaufman, L. (1982) Tonotopic organization of the human auditory cortex, *Science* **216**, 1339–1340.
126. Maclin, E., Okada, Y.C., Kaufman, L., and Williamson, S.J. (1983) Retinotopic map on visual cortex for eccentrically placed patterns: First noninvasive measurement, *Il Nuovo Cimento* **2D**, 410–419.
127. Schlitt, H.A., Heller, L., Aaron, R., Best, E., and Ranken, D.M. (1995) Evaluation of boundary element methods for the EEG forward problem: Effect of linear interpolation, *IEEE Trans. Biomed. Eng.* **42(1)**, 52–58.
128. Schlitt, H.A., Heller, L., Best, E., Ranken, D.M., and Aaron, R. (1994) Effect of conductor geometry on source localization: Implications for epilepsy studies, in N. Tepley (ed.), *NABMAG2 - Proceedings of the Second North American Biomagnetism Action Group Meeting*, Henry Ford Hospital, Detroit, Michigan.
129. Maurer, Jr., C.R., Aboutanos, G.B., Dawant, B.M., Gadamsetty, S., Margolin, R.A., Maciunas, R.J., and Fitzpatrick, J.M. (1994) Effect of geometrical distortion correction in MR on image registration accuracy, in *Medical Imaging VIII: Image Processing*, SPIE Proceedings, vol. 2167, pp. 200–213.
130. Ebersole, J.S. (1991) EEG dipole modeling in complex partial epilepsy, *Brain Topog.* **4(2)**, 113–123.
131. Cooper, R., Winter, A.L., Crow, H.J., and Walter, W.G. (1969) Comparison of subcortical, cortical, and scalp activity using chronically indwelling electrodes in man, *Electroenceph. clin. Neurophysiol.* **18**, 217–228.
132. Mosher, J.C., Lewis, P.S., and Leahy, R.M. (1992) Multiple dipole modeling and localization from spatio-temporal MEG data, *IEEE Trans. Biomed. Eng.* **39(6)**,

541–557.
133. Gorodnitsky, I.F., George, J.S., and Rao, B.D. (1995) Neuromagnetic source imaging with FOCUSS: A recursive weighted minimum norm algorithm, *Electroencephal. clin. Neurophysiol.* **95(4)**, 231–251.
134. Gorodnitsky, I.F. and Rao, B.D. (1997) Sparse signal reconstruction from limited data using FOCUSS: A recursive weighted minimum norm algorithm, *IEEE Trans. on Sig. Processing* **45(3)**, 600–616.
135. Robinson, S.E. and Vrba, J. (1999) Functional neuroimaging by synthetic aperture magnetometry (SAM), *Proc. 11th Inter. Conf. on Biomagnetism*, Sendai, Japan, pp. 302–305.
136. Ishii, R., Shinosaki, K., Ukai, S., Inouye, T., Ishihara, T., Yoshimine, T., Hirabuki, N., Asada, H., Kihara, T., Robinson, S.E., and Takeda, M. (1999) Medial prefrontal cortex generates frontal midline theta rhythm, *NeuroReport* **10(4)**, 675–679.
137. Wang, J.-Z., Williamson, S.J., and Kaufman, L. (1995) Kinetic images of neuronal activity of the human brain based on the spatio-temporal MNLS inverse: A theoretical study, *Brain Topog.* **7(3)**, 193–200.
138. Gençer, N.G. and Williamson, S.J. (1997) Magnetic source images of human brain functions, *Behavior Res. Meth. Instrum. and Comp.* **29(1)**, 78–83.
139. Wikswo, Jr., J.P., Crum, D.B., Henry, W.P., Ma, Y.P., Sepulveda, N.G., and Staton, D.J. (1993) An improved method for magnetic identification and localization of cracks in conductors, *J. Nondestr. Eval.* **12(2)**, 109–119.
140. Ma, Y.P. and Wikswo, Jr., J.P. The magnetic field produced by an elliptical flaw in a current carrying plate, in preparation.
141. Ma, Y.P. and Wikswo, Jr., J.P. Magnetic field of a subsurface spherical flaw inside a current-carrying conductor, in preparation.
142. Ewing, A.P., Hall Barbosa, C., Cruse, T.A., Bruno, A.C., and Wikswo, Jr., J.P. (1998) Boundary integral equations for modeling arbitrary flaw geometries in electric current injection NDE, in D.O. Thompson and D.E. Chimenti (eds.), *Review of Progress in QNDE*, Plenum Press, New York, vol. 17A, pp. 1011–1015.
143. Hurley, D.C., Ma, Y.P., Tan, S., and Wikswo, Jr., J.P. (1993) A comparison of SQUID imaging techniques for small defects in nonmagnetic tubes, in D.O. Thompson and D.E. Chimenti (eds.), *Review of Progress in QNDE*, Plenum Press, New York, vol. 12A, pp. 633–640.
144. Cruse, T.A., Ewing, A.P., and Wikswo, Jr., J.P. (1999) Green's function formulation of Laplace's equation for electromagnetic crack detection, *Computational Mechanics* **23(5/6)**, 420–429.
145. Ewing, A.P., Cruse, T.A., and Wikswo, Jr., J.P. (1998) A SQUID NDE measurement model using BEM, in D.O. Thompson and D.E. Chimenti (eds.), *Review of Progress in QNDE*, Plenum Press, New York, vol. 17A, pp. 1083–1090.
146. Ewing, A.P., Cruse, T.A., and Wikswo, Jr., J.P. A boundary element measurement model for SQUID nondestructive evaluation: An experimental comparison, unpublished.
147. Ewing, A.P., Cruse, T.A., and Wikswo, Jr., J.P. Using a SQUID measurement model for sensitivity analysis to determine probability of detection, unpublished.
148. Lü, Z.-L., Williamson, S.J., and Kaufman, L. (1992) Human auditory primary and association cortex having differing lifetimes for activation traces, *Brain Res.* **527**, 236–241.
149. Kaufman, L., Curtis, S., Wang, J.-Z., and Williamson, S.J. (1992) Changes in cortical activity when subjects scan memory for tones, *Electroenceph. clin. Neurophysiol.* **82**, 266–284.
150. Hari, R., Salmelin, R., Tissari, S.O., Kajola, M., and Virsu, V. (1994) Visual stability during picture naming, *Nature* **367**, 121–122.
151. Salmelin, R., Hari, R., Lounasmaa, O.V., and Sams, M. (1994) Dynamics of brain activation during picture naming, *Nature* **368**, 463–465.
152. Yang, T.T., Gallen, C.C., Schwartz, B.J., and Bloom, F.E. (1993) Noninvasive

somatosensory homunculus mapping in humans by using a large-array biomagnetometer, *Proc. Natl. Acad. Sci. USA* **90**, 3098–3102.
153. Yang, T.T., Gallen, C., Schwartz, B., Bloom, F.E., Ramachandran, V.S., and Cobb, S. (1994) Sensory maps in the human brain, *Nature* **368**, 592–593.
154. Romani, G.L., Del Gratta, C., Pizzella, V. (1996) Neuromagnetism and its clinical applications, in H. Weinstock (ed.), *SQUID Sensors: Fundamentals, Fabrication and Applications*, Kluwer Academic Publishers, Netherlands, pp. 445–490.
155. Wakai, R.T., Wang, M., and Martin, C.B. (1994) Spatiotemporal properties of the fetal magnetocardiogram, *Am. J. Obstet. Gynecol.* **170(3)**, 770–776.
156. Zhuravlev, Y.E., Rassi, D., and Emery, S.J. (in press, 1999) Clinical assessment of fetal magnetocardiography, *IEEE Trans. Applied Supercond.*
157. Lowery, C., Robinson, S., Eswaran, H., Vrba, J., Haid, V., and Cheung, T. (1999) Detection of the transient and steady-state auditory evoked responses in the human fetus, *Proc. 11th Inter. Conf. on Biomagnetism*, Sendai, Japan, pp. 963–966.
158. Burghoff, M., Curio, G., Haberkorn, W., Mackert, B.-M., and Trahms, L. (1994) *Quellenbildgebung aus biomagnetischen Feldern peripherer Nerven. Proceedings of the Congress, Biomedizinische Technik.*
159. Mackert, B.-M., Curio, G., Burghoff, M., and Marx, P. (1997) Mapping of tibial nerve evoked magnetic fields over the lower spine, *Electroenceph. clin. Neurophysiol.* **104(4)**, 322–327.
160. Mackert, B.-M., Curio, G., Burghoff, M., Trahms, L., and Marx, P. (1998) Magnetoneurographic 3D-localization of conduction blocks in patients with unilateral S1 root compression, *Electroenceph. clin. Neurophysiol.* **109**, 315–320.
161. Golzarian, J., Staton, D.J., Wikswo, Jr., J.P., Friedman, R.N., and Richards, W.O. (1994) Diagnosing intestinal ischemia using a noncontact superconducting quantum interference device, *Am. J. Surgery* **167**, 586–592.
162. Modena, I., Ricci, G.B., Barbanera, S., Leoni, R., Romani, G.L., and Carelli, P. (1982) Biomagnetic measurements of spontaneous brain activity in the brain following repetitive sensory stimulation, *Electroenceph. clin. Neurophysiol.* **54**, 622–628.
163. Barth, D.S., Sutherling, W., Engel, Jr., J., and Beatty, J. (1982) Neuromagnetic localization of epileptiform spike activity in the human brain, *Science* **218**, 891–894.
164. Hari, R., Ahonen, A., Forss, N., Granström, M.-L., Hämäläinen, M., Kajola, M., Knuutila, J., Lounasmaa, O.V., Makela, J.P., and Paetau, R., Salmelin, R., and Simola, J. (1993) Parietal epileptic mirror focus detected with a whole-head neuromagnetometer, *NeuroReport* **5(1)**, 45–48.
165. Orrison, W.W. and Lewine, J.D. (1993) Magnetic source imaging in neurosurgical practice, *Prospectives in Neurosurgical Surgery* **4(2)**, 141–147.
166. Benzel, E.C., Lewine, J.D., Bucholz, R.D., and Orrison, W.W. (1993) Magnetic source imaging: A review of the *Magnes* system of Biomagnetics Technology Incorporated, *Neurosurg.* **33**, 252–259.
167. Lewine, J.D. and Orrison, W.W. (1995) Magnetoencephalography amd Magnetic Source Imaging, in W.W. Orrison, J.D. Lewine, J.A. Sanders, and M. Hartshorne (eds.), *Functional Brain Imaging*, Mosby Yearbooks, St. Louis, pp. 369–416.
168. Barkley, G.L., Tepley, N., Nagel-Leiby, S., Moran, J.E., Simkins, R.T., and Welch, K.M.A. (1990) Magnetoencephalographic studies of migraine, *Headache J.* **30(7)**, 428–434.
169. Barry, W.H., Harrison, D.C., Fairbank, W.M., Lehrman, K., Malmivuo, J.A.V., and Wikswo, Jr., J.P. (1977) Measurement of the human magnetic heart vector, *Science* **198**, 1159–1162.
170. Wikswo, Jr., J.P. and Barach, J.P. (1982) Possible sources of new information in the magnetocardiogram, *J. Theoretical Biol.* **95**, 721–729.
171. Roth, B.J. and Wikswo, Jr., J.P. (1986) Electrically-silent magnetic fields, *Biophys. J.* **50**, 739–745.
172. Lant, J., Stroink, G., Ten Voorde, B., Horachek, M., and Montague, T.J. (1990) Complementary nature of electrocardiographic and magnetocardiographic data in

patients with ischemic heart disease, *J. Electrocardiology* **23**, 315–322.
173. Stroink, G., Lant, J., Elliot, P., and Gardner, M. (1992) Magnetic field and body surface potential mapping of patients with ventricular tachycardia, in M. Hoke, S.N. Erne, Y.C. Okada, and G.-L. Romani (eds.), *Biomagnetism: Clinical Aspects*, Elsevier, Amsterdam, pp. 471–475.
174. Malmivuo, J. and Plonsey, R. (1994) *Bioelectromagnetism - Principles and Applications of Bioelectric and Biomagnetic Fields*, Oxford University Press, New York.
175. Stroink, G., Moshage, W., and Achenbach, S. (1998) Cardiomagnetism, in W. Andrä and H. Nowak (eds.), *Magnetism in Medicine: A handbook*, Wiley-VCH, New York, pp. 163–189.
176. Stroink, G. (1999) New developments in magnetocardiology, *Proc. 11th Inter. Conf. on Biomagnetism*, Sendai, Japan, pp. 982–985.
177. Gornick, C.C., Adler, S.W., Pederson, B., Hauck, J., Budd, J., and Schweitzer, J. (1999) Validation of a new noncontact catheter system for electroanatomic mapping of left ventricular endocardium, *Circulation* **99(6)**, 829–835.
178. Schilling, R.J., Peters, N.S., and Wyn Davies, D. (1998) Simultaneous endocardial mapping in the human left ventricle using a noncontact catheter, *Circulation* **98(9)**, 887–898.
179. Van Leeuwen, P., Hailer, B., and Wehr, M. (1996) Spatial distribution of QT intervals: An alternative approach to QT dispersion, *Pace* **19(1) Part II**, 1894–1899.
180. Brockmeier, K., Schmitz, L., Chavez, J.J.B., Burghoff, M., Koch, H., Zimmerman, R., and Trahms, L. (1997) Magnetocardiography and 32-lead potential mapping: Repolarization in normal subjects during pharmacologically induced stress, *J. Cardiovasc. Electrophysiol.* **8**, 615–626.
181. Moshage, W. and Achenbach, S. (1997) Clinically significant differences between ECG and MCG, *Biomedizinische Technik* **42(1)**, 25–28.
182. Hailer, B., Van Leeuwen, Lange, S., and Wehr, M. (1997) Magnetocardiography in risk stratification after myocardial infarction using spatial dispersion of the QT interval, *Biomedizinische Technik* **42(1)**, 136–139.
183. Van Leeuwen, P., Hailer, B., and Wehr, M. (1997) Changes in current dipole parameters in patients with coronary artery disease with and without myocardial infarction, *Biomedizinische Technik* **42(1)**, 132–135.
184. Van Leeuwen, Hailer, B., Donker, D., Lange, S., and Wehr, M. (1998) Noninvasive diagnosis of coronary artery disease at rest on the basis of multichannel magnetocardiography, *Pace* **21 Part II**, 908 (Abstract).
185. Hailer, B., Van Leeuwen, P., Pilath, M., Lange, S., Grönemeyer, Wehr, M., and Anstalt, A.K. (1998) Changes in the spatial dispersion of QT interval in patients with coronary artery disease, *Pace* **21 Part II**, 908 (Abstract).
186. Gessner, Ch., Endt, P., Burghoff, M., and Trahms, L. (1998) Vortex currents detected by stress MCG and fragmentation of ECG/MCG in VT patients, *Proc. 43rd Seminar on High-Resolution Electrocardiography and Magnetocardiography*, Warsaw, Poland.
187. Hailer, B., Van Leeuwen, P., Lange, S., Grönemeyer, and Wehr, M. (1998) Spatial dispersion of the magnetocardiographically determined QT interval and its components in the identification of patients at risk for arrhythmia after myocardial infarction, *Annals Noninvas. Electrocardiol.* **3(4)**, 311–318.
188. Endt, P., Hahlbohm, H.-D., Kreiseler, D., Oeff, M., Steinhoff, U., and Trahms, L. (1998) Fragmentation of the bandpass filtered QRS-complex of patients prone to malignant arrhythmia, *Med. Biol. Eng. Comput.* **36**, 723–728.
189. Drake, W.B., Bradshaw, L.A., Fish, F.A., Mellen, B.G., and Wikswo, Jr., J.P. (1998) Magnetocardiographic assessment of developmental changes in fetal cardiac intervals, *Circulation* **98(17)**, I–835 (Abstract).
190. Drake, W.B., Bradshaw, L.A., Mellen, B.G., Fish, F.A., and Wikswo, Jr., J.P. Evaluation of fetal intracardiac intervals using vector magnetocardiography, in prepara-

tion.

191. Lowery, C., Robinson, S., Eswaran, H., Vrba, J., Haid, V., and Cheung, T. (1999) Detection of the transient and steady-state auditory evoked responses in the human fetus, *Proc. 11th Inter. Conf. on Biomagnetism*, Sendai, Japan, pp. 963–966.
192. Staton, D.J., Friedman, R.N., and Wikswo, Jr., J.P. (1993) High resolution SQUID imaging of octupolar currents in anisotropic cardiac tissue, *IEEE Trans. Applied Supercond.* **3(1)**, 1934–1936.
193. Bradshaw, L.A., Ladipo, J.K., Haupt, C.D., Seidel, S.A., van Leeuwen, P., Wikswo, Jr., J.P., and Richards, W.O. (1998) Noninvasive measurement of gastric propagation using a multichannel SQUID magnetometer, *Gastroenterology* **114(4 Part 2)**, G3003 (Abstract).
194. Richards, W.O., Bradshaw, L.A., Staton, D.J., Garrard, C.L., Liu, F., Buchanan, S., and Wikswo, Jr., J.P. (1996) Magnetoenterography (MENG): Noninvasive measurement of bioelectric activity in human small intestine, *Digestive Diseases and Sciences* **41(12)**, 2293–2301.
195. Richards, W.O., Staton, D.J., Golzarian, J., Friedman, R.N., and Wikswo, Jr., J.P. (1995) Non-invasive SQUID magnetometer measurement of human gastric and small bowel electrical activity, in L. Deecke, C. Baumgartner, G. Stroink, and S.J. Williamson (eds.), *Proc. 9th Inter. Conf. on Biomagnetism*, Vienna, pp. 743–747.
196. Richards, W.O., Garrard, C.L., Allos, S.H., Bradshaw, L.A., Staton, D.J., and Wikswo, Jr., J.P. (1995) Noninvasive diagnosis of mesenteric ischemia using a SQUID magnetometer, *Annals of Surgery* **221(6)**, 696–705.
197. Allos, S.H., Staton, D.J., Bradshaw, L.A., Halter, S., Wikswo, Jr., J.P., and Richards, W.O. (1997) Superconducting quantum interference device magnetometer for diagnosis of ischemia caused by mesenteric venous thrombosis, *World J. Surg.* **21**, 173–178.
198. Bradshaw, L.A., Allos, S.H., Wikswo, Jr., J.P., and Richards, W.O. (1997) Correlation and comparison of magnetic and electric detection of small intestinal electrical activity, *Am. J. Physiol.* **272**, G1159–G1167.
199. Bradshaw, L.A., Ladipo, J.K., Staton, D.J., Wikswo, Jr., J.P., and Richards, W.O. (1999) The human vector magnetogastrogram and magnetoenterogram, *IEEE Trans. Biomed. Eng.* **46(8)**, 959–970.
200. Weitschies, W., Kötitz, R., Cordini, D., and Trahms, L. (1997) High-resolution monitoring of the gastrointestinal transit of a magnetically marked capsule, *J. Pharmaceutical Sci.* **86(11)**, 1218–1222.
201. Farrell, D.E., Allen, C.J., Arendt, P.N., Foltyn, S.R., Paulson, D.N., Fagaly, R.L., Brittenham, G.M. (1999) High-T_c SQUID susceptometry, *Bull. Am. Phys. Soc.* **444(1/II)**, 1553.
202. Barth, D.S., Sutherling, W., and Beatty, J. (1984) Fast and slow magnetic phenomena in focal epileptic seizures, *Science* **226**, 855–857.
203. Okada, Y.C., Wu, J., and Kyuhou, S.-I. (1997) Genesis of MEG signals in a mammalian CNS structure, *Electroenceph. clin. Neurophysiol.* **103**, 474–485.
204. Wikswo, Jr., J.P., Friedman, R.N., Kilroy, A.W., van Egeraat, J.M., and Buchanan, D.S. (1990) Preliminary measurements with MicroSQUID, in S.J. Williamson, M. Hoke, G. Stroink, and M. Kotani (eds.), *Advances in Biomagnetism*, Plenum Press, New York, pp. 681–684.
205. Thomas, I.M., Freake, S.M., Swithenby, S.J., and Wikswo, Jr., J.P. (1993) A distributed quasi-static ionic current source in the 3-4 day old chicken embryo, *Phys. Med. Biol.* **38**, 1311–1328.
206. Thomas, I.M. and Friedman, R.N. (1995) Study of macrophage activity in rat liver using intravenous superparamagnetic tracers, in L. Deecke, C. Baumgartner, G. Stroink, and S.J. Williamson (eds.), *Proc. 9th Inter. Conf. on Biomagnetism*, Vienna, pp. 809–813.
207. Goranson, U.G. and Miller, M. (1991) Aging jet transport structural evaluation programs, in S.N. Atluri, S.G. Sampath, and P. Tong (eds.), *Structural Integrity of*

Aging Airplanes, Springer-Verlag, Berlin, pp. 131–140.
208. Bobo, S.N. (1990) The aging aircraft fleet: A challenge for nondestructive inspection, in D.O. Thompson and D.E. Chimenti (eds.), *Review of Progress in QNDE*, Plenum Press, New York, **vol. 9B**, pp. 2097–2109.
209. Ma, Y.P. and Wikswo, Jr., J.P. (1998) SQUID magnetometers for depth-selective, oriented eddy current imaging, in D.O. Thompson and D.E. Chimenti (eds.), *Review of Progress in QNDE*, Plenum Press, vol. 17A, pp. 1067–1074.
210. Ma, Y.P., Ewing, A.P., and Wikswo, Jr., J.P. SQUID eddy current measurements using a sheet inducer, in preparation.
211. Ma, Y.P. and Wikswo, Jr., J.P. (1995) Techniques for depth-selective, low-frequency eddy current analysis for SQUID-based non-destructive testing, *J. Nondestr. Eval.* **14(3)**, 149–167.
212. Ma, Y.P. and Wikswo, Jr., J.P. (1996) Depth-selective SQUID eddy current techniques for second layer flaw detection, in D.O. Thompson and D.E. Chimenti (eds.), *Review of Progress in QNDE*, Plenum Press, New York, vol. 15A, pp. 401–408.
213. Hall Barbosa, C., Bruno, A.C., Vellasco, M., Pacheco, M., Wikswo, Jr., J.P., Ewing, A.P., and Camerini, C.S. (in press) Automation of SQUID nondestructive evaluation of steel plates by neural networks, *IEEE Trans. Applied Supercond.*
214. Cochran, Sandy, University of Strathclyde, Glasgow, Scotland, personal communication.
215. Cochran, A., Donaldson, G.B., Morgan, L.N.C., Bowman, R.M., and Kirk, K.J. (1993) SQUIDs for NDT: The technology and its capabilities, *British J. NDT* **35**, 173–182.
216. Otaka, M., Enomoto, K., Hayashi, M., Sakata, S., and Shimizu, S. (1994) Detection of fatigue damage in stainless steel using a SQUID sensor, in J.C. Spanner, Jr. (ed.), *The American Society Mechanical Engineers*, PVP-vol. 276, book no. G00844: Determining Material Characterization, pp. 113–117.
217. Sawade, G., Krause, H.-J., Gampe, U. (1997) Non destructive examination of prestressed tendons by the magnetic stray field method, in M.T. Forde (ed.), *Proceedings of the 7th International Conference on Structural Faults and Repair - 97*, Engineering Technic Press, Edinburgh, vol. I, pp. 401–406.
218. Bellingham, J.G., MacVicar, M.L.A., Nisenoff, M., and Searson, P.C. (1986) Detection of magnetic fields generated by electrochemical corrosion, *J. Electrochem. Soc.* **133**, 1753–1754.
219. Bellingham, J.G., MacVicar, M.L.A., and Nisenoff, M. (1987) SQUID technology applied to the study of electrochemical corrosion, *IEEE Trans. Mag.* **23(2)**, 477–479.
220. Jette, B.D. and MacVicar, M.L.A. (1991) SQUID magnetometry applied as a non-invasive electroanalytic chemical technique, *IEEE Trans. Mag.* **27**, 3025–3028.
221. Misra, M., Lordi, S., and MacVicar, M.L.A. (1991) Applications of SQUID magnetometry to electrochemical systems, *IEEE Trans. Mag.* **27**, 3245–3248.
222. Hibbs, A.D., Sager, R.E., Cox, D.W., Aukerman, T.H., Sage, T.A., and Landis, R.S. (1992) A high-resolution magnetic imaging system based on a SQUID magnetometer, *Rev. Sci. Instrum.* **63(7)**, 3652–3658.
223. Hibbs, A.D. (1992) Measurement of electrochemical corrosion currents using a multichannel superconducting quantum interference device magnetometer, *J. Electrochem. Soc.* **139(9)**, 2447–2457.
224. Richter, H. and Knecht, A. (1997) HTS SQUID magnetometer - feasibility study on non-destructive detection of corrosion currents in aluminum aircraft parts, *Materialpruefung* **39**, 390–396.
225. Li, D., Ma, Y.P., Flanagan, W.F., Lichter, B.D., and Wikswo, Jr., J.P. (1994) The use of superconducting magnetometry to detect corrosion in aircraft alloys, *Proceedings of the Tri-Service Conference on Corrosion*, Orlando, FL, pp. 335–346.
226. Li, D., Ma, Y.P., Flanagan, W.F., Lichter, B.D., and Wikswo, Jr., J.P. (1995) Detecting in-situ active corrosion by a SQUID magnetometer, *J. Minerals, Metals*

and Materials **47**, 36–39.

227. Li, D., Ma, Y.P., Flanagan, W.F., Lichter, B.D., and Wikswo, Jr., J.P. (1996) Application of superconducting magnetometry in the study of aircraft aluminum alloy corrosion, *Corrosion* **52**, 219–231.
228. Li, D., Ma, Y.P., Flanagan, W.F., Lichter, B.D., and Wikswo, Jr., J.P. (1997) Detection of hidden corrosion of aircraft aluminum alloys by magnetometry using a superconducting quantum interference device, *Corrosion* **53**, 93–98.
229. Abedi, A. and Wikswo, Jr., J.P. Investigating and modeling of the sources of magnetic field associated with uniform corrosion of 7075-T6 aircraft aluminum alloy, in preparation.
230. Skennerton, G., Abedi, A., and Wikswo, Jr., J.P. Magnetic measurements of the response of corrosion activity within aircraft lap joints to accelerated corrosion testing, in preparation.
231. Fitzpatrick, G.L., Thome, D.K., Skaugset, R.L., and Shih, E.Y.C. (1993) The present status of magneto-optic eddy current imaging technology, in D.O. Thompson and D.E. Chimenti (eds.), *Review of Progress in QNDE*, Plenum Press, New York, vol. 12A, pp. 617–624.
232. Staton, D.J., Rousakov, S.V., and Wikswo, Jr., J.P. (1996) Conductivity imaging in plates using current injection tomography, in D.O. Thompson and D.E.Chimenti (eds.), *Review of Progress in QNDE*, Plenum Press, New York, vol. 15A, pp. 845–851.
233. Wikswo, Jr., J.P., Gevins, A., and Williamson, S.J. (1993) The future of the EEG and MEG, *Electroenceph. clin. Neurophysiol.* **87**, 1–9.
234. Tucker, D.M. (1993) Spatial sampling of head electrical fields: The geodesic sensor net, *Electroenceph. clin. Neurophysiol.* **87**, 154–163.
235. Gevins, A.S., DuRosseau, D., and Libove, J. (1991) Electrode system for brain wave detection, *U.S. Patent 5,038,782.*
236. Gevins, A.S., Le, J., Brickett, P., Reutter, B., and Desmond, J. (1991) Seeing through the skull: Advanced EEGs use MRIs to accurately measure cortical activity from the scalp, *Brain Topog.* **4(2)**, 125–131.
237. Gevins, A., Smith, M.E., Le, J., Leong, H., Bennett, J., Martin, N., McEvoy, L., Du, R., Whitfield, S. (1996) High resolution evoked potential imaging of the cortical dynamics of human working memory, *Electroenceph. clin. Neurophysiol.* **98**, 327–348.
238. (1993) *Surgical Treatment of the Epilepsies*, J. Engel, Jr. (ed.), Raven Press, New York, p. 26.